The Pennsylvania State University

The Graduate School

Department of Materials Science and Engineering

STRUCTURE - PROPERTY - COMPOSITIONAL RELATIONSHIPS IN THE

BaTiO$_3$ – BiScO$_3$ CERAMIC SYSTEM

A Thesis in

Materials Science and Engineering

by

Hideki Ogihara

Submitted in Partial Fulfillment

of the Requirements

for the Degree of

Master of Science

August 2008

The thesis of Hideki Ogihara was reviewed and approved * by the following:

Clive A. Randall
Professor of Materials Science and Engineering
Thesis Co-Advisor

Susan Trolier-McKinstry
Professor of Ceramic Science and Engineering
Thesis Co-Advisor

L. Eric Cross
Evan Pugh Professor Emeritus of Electrical Engineering

Elizabeth C. Dickey
Professor of Materials Science and Engineering

Shujun Zhang
Assistant Professor of Materials Science and Engineering

Joan M. Redwing
Professor of Materials Science and Engineering
Associate Head for Graduate Studies

* Signatures are on file in the Graduate School

ABSTRACT

The structural and dielectric properties of bulk (1-x) BaTiO$_3$ - x BiScO$_3$ (x = 0 to 0.5) ceramics were investigated to acquire a better understanding of the binary system, including determination of the phase diagram, displacive phase transitions, the associated dielectric properties, and the differences in the roles of Bi$_2$O$_3$ and BiScO$_3$ doping in BaTiO$_3$.

The solubility limit for BiScO$_3$ into the BaTiO$_3$ perovskite structure was determined to be about x = 0.4, which is much higher than the solubility of Bi alone. A structural change from tetragonal to pseudocubic was observed at about x = 0.05 - 0.075 at room temperature. The solubility was investigated through the systematic trends in the dielectric data, lattice parameter, and microstructure.

Dielectric measurements revealed a gradual change from normal ferroelectric behavior in pure BaTiO$_3$ to a highly diffusive and dispersive relaxor behavior from 10 to 40 mol% BiScO$_3$. Several of the compositions showed high permittivities (approximately 1000) with low temperature coefficients of capacitance over a wide range of temperature. This result confirmed the result from the earlier work in thin films that the broad, frequency-dependent-permittivity maximum is an intrinsic material property, neither a consequence of defects or stresses associated with the thin film preparation, nor a space charge contribution. It was found that the temperature for the maximum dielectric constant, T$_{max}$, increases with increasing BiScO$_3$ concentration. The Vogel-Fulcher model gave an activation energy of 0.2-0.3 eV for the relaxor behavior range, which was high compared with other relaxors. The attempt frequency was on the order of 10^{13} Hz

and the freezing temperature, T_f, ranged from -177 to -93 ^{o}C (96 to 160 K) as a function of composition.

The dielectric constant is high and stable from 0 – 300 ^{o}C for the 0.7 BaTiO$_3$ - 0.3 BiScO$_3$ ceramics, making this composition attractive for high energy density capacitor applications. A single dielectric layer capacitor was prepared to confirm the feasibility of BaTiO$_3$ - BiScO$_3$ as a capacitor material. The 0.7 BaTiO$_3$ - 0.3 BiScO$_3$ capacitors exhibited an energy density of about 6.1 J/cm^3 at a field of 73 kV/mm at room temperature, which is superior to some commercial X7R capacitors. Moreover, this system may be very useful at high temperatures, as the permittivity of commercial BaTiO$_3$ – based capacitors drops rapidly above the transition temperature (around 130 ^{o}C). In this study, relatively high, temperature-stable energy density values were confirmed from room temperature to 300 ^{o}C.

Another application possibility is as a base composition for lead-free piezoelectrics. Undoped BaTiO$_3$ - BiScO$_3$ ceramics are electrostrictors at room temperature over a wide composition range, but the highly polarizable material may be useful as a piezoelectric matrix if a normal ferroelectric phase could be developed. Possible off-center ions, Li and Na were doped into the system in an attempt to stabilize a normal ferroelectric phase. LiNbO$_3$ could not achieve a solid solution. For the case of Na, solid solution was confirmed up to 15 mol% NaNbO$_3$, but there was no indication of the stabilization of a normal ferroelectric. Instead, it was found that T_{max} and T_f decrease with increasing NaNbO$_3$ concentration. This result suggests that NaNbO$_3$ doping breaks up the polar ordering developed in the BaTiO$_3$ - BiScO$_3$ system.

TABLE OF CONTENTS

LIST OF FIGURES

LIST OF TABLES

ACKNOWLEDGEMENTS

I would like to thank my advisors, Dr. Clive A. Randall and Dr. Susan Trolier-McKinstry, for their kind and continuous support towards the degree. Over the last two years of graduate work and my undergraduate study in 2001 - 2003, they taught me not only about the subject of electroceramics, but also many fundamental things which are essential as a scientist. The things I learned from them will be valuable for the rest of my life. I would also like to acknowledge the rest of my committee members, namely, Dr. Leslie Eric Cross, Dr. Elizabeth C. Dickey, and Dr. Shujun Zhang for their helpful suggestions and discussions.

I also want to acknowledge the community of the Center for Dielectric Studies (CDS) at Penn State for funding this project and for opportunities to present the work to center members.

Many thanks go to all the people in MRI for their support. Especially, my study would never be completed without the following: Beth and Amanda for sample preparation, Jeff for dielectric measurements, Nicole for x-ray diffraction, Maria for scanning electron microscopy, Maria for polishing/sputtering samples, Trevor for transmission electron microscopy, and Joanne and Susie for decoding my advisors' hand-writing.

I would like to thank the friends that made my life in State College exciting. Special thanks should go to my soccer and golf friends, who I spent most of my free time with. Last but not least, I really appreciate the continuous support and encouragement from my parents in Japan.

Chapter 1: Introduction

1.1 Motivation

1.1.1 BaTiO$_3$ - BiScO$_3$ System

BaTiO$_3$ – based solid solutions have been extensively studied as means of tailoring the ferroelectric transition temperatures, (i.e. manipulating the transitions by compositional routes to engineer the temperature dependence of the dielectric constant), and controlling the defect chemistry or defect mobilities as a function of applied dc fields (Jaffe et al., 1971; Hennings et al.; 1982; Randall et al., 1993; Kishi et al., 1999, 2003; Lee et al., 2007). The resulting materials have been widely employed in capacitors, thermistors, dielectric bolometers, pyroelectrics, and piezoelectrics (Lines and Glass, 2007; Moulson and Herbert, 2003). As new perovskite end-member materials are developed, it is thus interesting to study how the structure and functional properties of BaTiO$_3$ - based ceramics are modified, both from the standpoint of developing new materials, and in developing a fundamental understanding of ferroelectrics.

Bi doped BaTiO$_3$ has been studied by several authors (Skanavi et al., 1958; Bogdanov et al., 1965; Zhou et al., 1999; Bahri et al., 2001). The motivation for Bi-doping BaTiO$_3$ includes the use of Bi as a sintering aid (Burn, 1982) or employing Bi as a donor dopant on the Ba site (Saburi, 1959). The solubility limit of Bi in BaTiO$_3$ has been reported to be 5 to 10 mole % on the A site of the perovskite lattice (Zhou et al., 1999; Bahri et al., 2001). The dielectric behavior is characterized by a transition from a normal ferroelectric to a relaxor as the Bi concentration increases.

Recently, Tinberg and Trolier-McKinstry reported on (1-x) BaTiO$_3$ - x BiScO$_3$ thin films (Tinberg and Trolier-McKinstry, 2007), following the work of Eitel et al. on

BiScO₃ – PbTiO₃ piezoelectrics (Eitel et al., 2001). A pure perovskite phase was achieved in the films with x = 0.2-0.45, even without epitaxy, which suggests that a stable perovskite phase could be prepared in bulk material as well. The resulting films showed highly dispersive dielectric peaks with modest remanent polarization values at room temperature, as shown in Figure 1.1.

It is interesting to confirm whether the dispersion is a consequence of defects or stresses associated with the thin film preparation or an intrinsic material property.

(a)   (b)
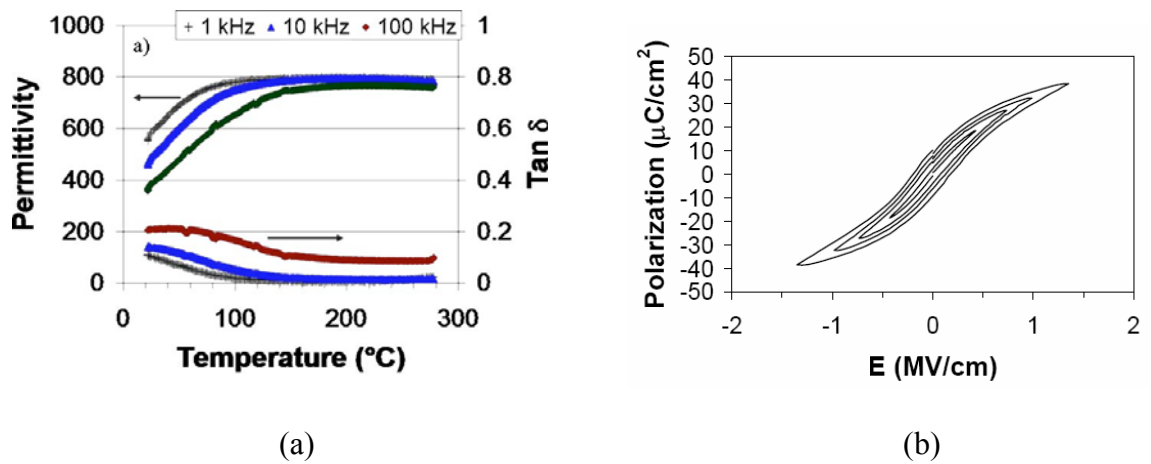
Figure 1.1.   Dielectric characteristics of 0.6 BaTiO₃ - 0.4 BiScO₃ thin film sample, (a) dielectric constant and loss vs. temperature and (b) polarization vs. electric field data (From Tinberg and Trolier-McKinstry, 2007)

1.1.2 High Energy Density Capacitor Application

A high energy density, on the order of 13 J/cm^3 for a bias field of about 1300 kV/cm at room temperature, was obtained from the hysteresis loop in Figure 1.1 (See section 3.3 for the calculation). This high value is partly due to the high breakdown strength of the film, but suggests that bulk ceramics might also have high energy densities over a wide range of temperature.

1.1.3 Non-lead Piezoelectrics

PbTiO$_3$ – PbZrO$_3$ (PZT) based materials have been employed in many piezoelectric applications such as sensors and actuators due to their high piezoelectric performance. However, use of lead carries with it some environmental concerns, and there is currently a strong push (especially in Europe and Asia) to develop alternate lead-free piezoelectric systems (Takenaka and Nagata, 2005).

The high dielectric constant and the stable perovskite phase observed in the BaTiO$_3$ - BiScO$_3$ thin film are attractive in the search for non-lead piezoelectric materials. At room temperature thin films are not expected to possess good piezoelectric properties because of the slim hysteresis loop with a modest remanent polarization. Consequently, it is interesting to consider whether or not it is possible to stabilize a long-range polarization in such a system, to make it more suitable for applications in poled ferroelectric states such as for piezoelectric and pyroelctric applications.

1.2 Objectives

The objectives of this study on the $BaTiO_3$ - $BiScO_3$ system are as follows:

- To determine whether the dispersion observed in thin films is an intrinsic material property or a consequence of defects or stresses associated with the thin film preparation.

- To acquire a better understanding of this system, including determination of the phase diagram, the low and high field dielectric properties, and the differences in the roles of Bi_2O_3 and $BiScO_3$ doping on $BaTiO_3$.

- To determine the energy densities that can be obtained under high electric fields.

- To investigate whether it is possible to stabilize a ferroelectric phase in $BiScO_3$-$BaTiO_3$ with high piezoelectric performance (i.e. high remanent polarization, high d_{33} value), by means of doping with off-center ions, such as Li, to create local dipoles.

Chapter 2: Background

2.1 Dielectric Materials

Electroceramic materials can be divided into 3 broad categories with respect to their electrical conduction behavior; namely, metals, semiconductors, and dielectrics (insulators) (Moulson and Herbert, 2003). Figure 2.1 shows the difference for the conduction mechanisms with a simple electron band model.
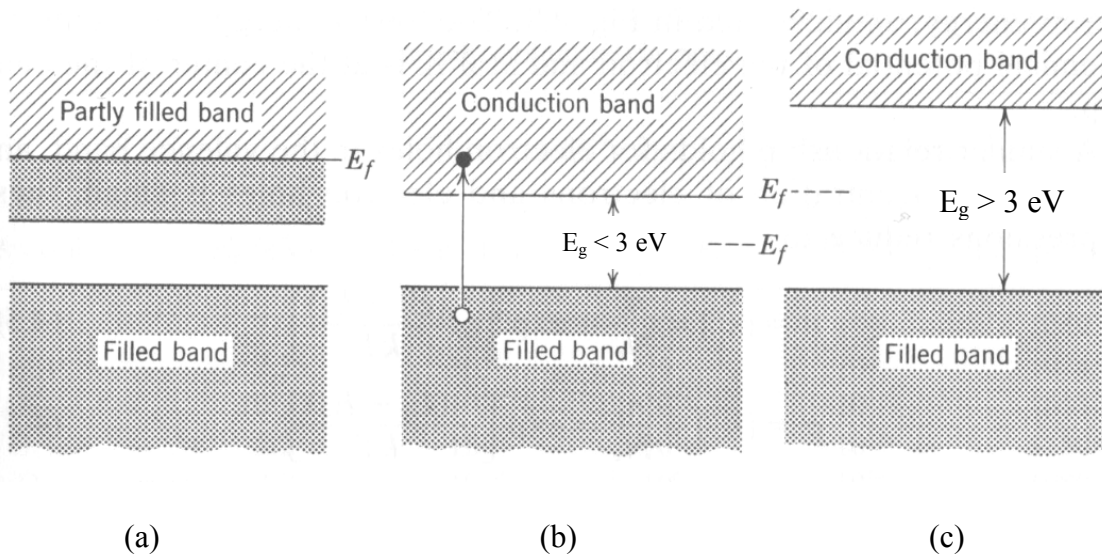
Figure 2.1.   Schematic electron band structures for (a) metals, (b) semiconductors, and

(c) dielectrics (after Kingery et al., 1976)

In metals, an electron with the highest energy lies in a partially filled band and excited states are continuously available. The energy of the highest filled level in the ground state at 0 K is defined as the Fermi energy, E_f (Kittel, 2005). On the other hand, semiconductors and insulators have a gap between the electron with the highest energy and the next available state. At 0 K, the valence band is completely filled, and the

conduction band is empty. In this case, E_f lies between the bands and it is at $E_g/2$ for intrinsic semiconductors and off-set by doping to give either n or p-type carriers. The energy difference between the valence and conduction bands is called the band gap. Dielectrics and semiconductors are distinguished by the magnitude of the band gap, E_g. If E_g is relatively small, materials are classified as semiconductors since thermal energy tends to be large enough to excite a population of electrons from the valence band to the conduction band, as shown in Figure 2.1 (b). If E_g is relatively large, materials are called dielectrics since thermal energy is insufficient to promote many electrons to the conduction band (Kingery et al., 1976). 2 - 3eV is often used as the boundary between semiconductors and insulators, but no strict definition has been made.

When an electric field is applied to a dielectric, it does not conduct current significantly unless a sufficiently strong field is applied to lead to dielectric breakdown. Rather, dielectric materials are polarized when an electric field is applied (Moulson and Herbert, 2003) as shown in Equation 2.1.

$$D = \varepsilon_0\, E + P = \varepsilon_0\, \varepsilon_r\, E \qquad\qquad (2.1)$$

where D is dielectric displacement, E is applied electric field, P is polarization induced in the material, ε_0 is the permittivity of free space, and ε_r is the relative permittivity of the material (or dielectric constant), respectively. The polarization can be expressed by:

$$P = \varepsilon_0\, (\varepsilon_r - 1)\, E = \chi\, \varepsilon_0\, E \qquad\qquad (2.2)$$

This defines the dielectric susceptibility $\chi = (\varepsilon_r - 1)$. For the materials described in this thesis, it is appropriate to use the approximation $P \sim \varepsilon_0\, \varepsilon_r\, E$ since $\varepsilon_r \gg 1$ for these materials. Note that the permittivity and dielectric susceptibility are 2nd rank tensors, $\varepsilon_{r\,ij}$ and χ_{ij}, respectively.

There are four primary mechanisms contributing to the polarization, namely, electronic, ionic, dipolar, and space charge polarizability (Moulson and Herbert, 2003). Figures 2.2 and 2.3 illustrate each mechanism and the frequency range over which it contributes to the observed response.
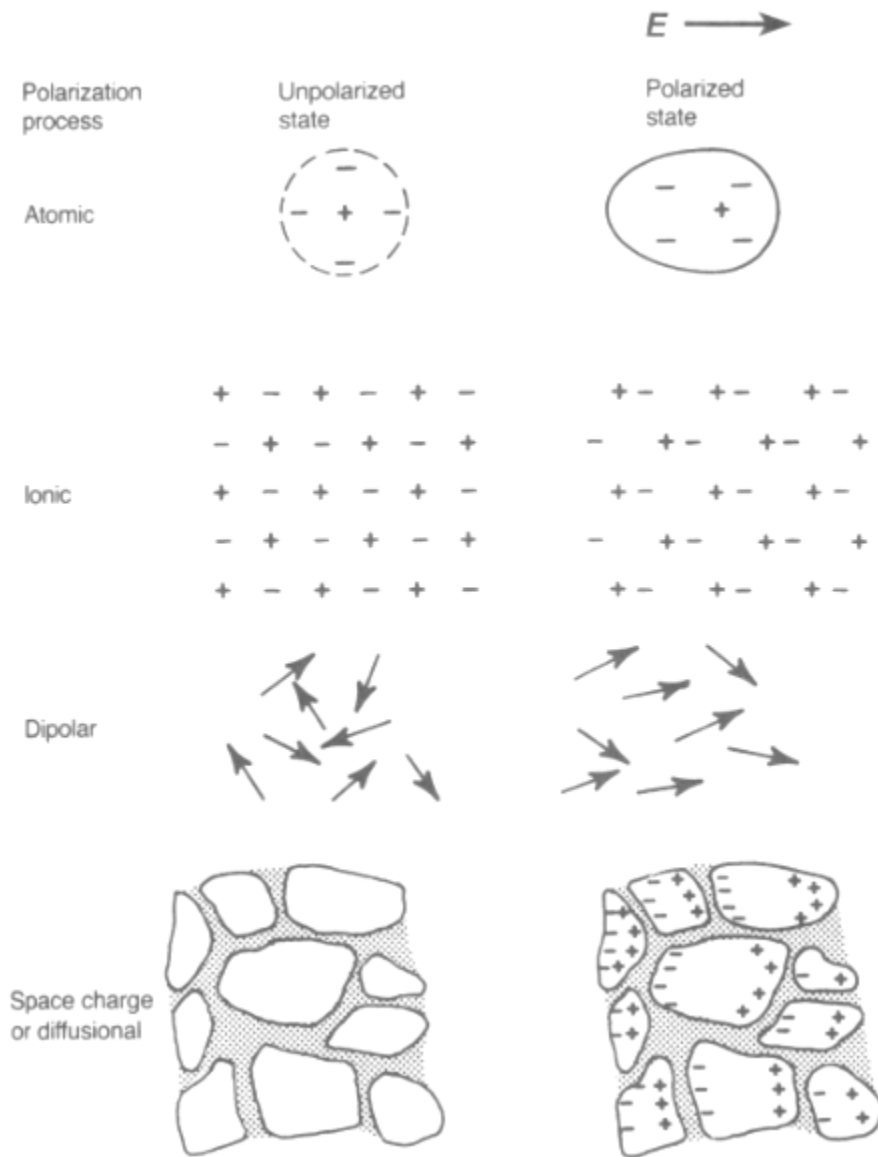
Figure 2.2.   Schematic illustrations for the four polarization mechanisms (from Moulson and Herbert, 2003)
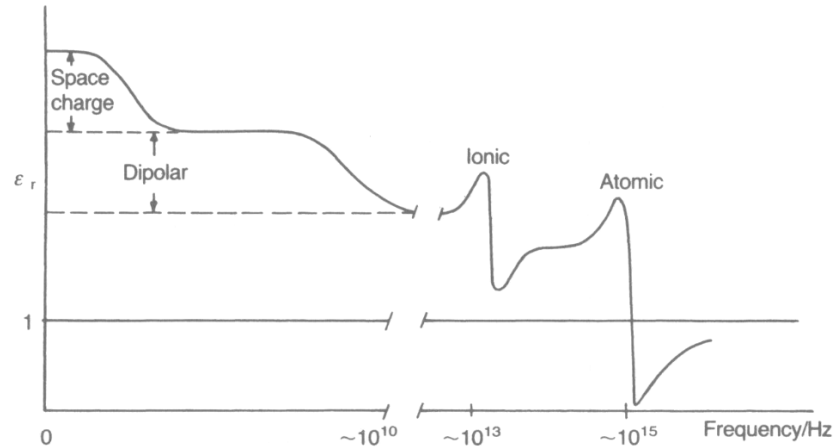
Figure 2.3.   A schematic showing the frequency dependence of the relative permittivity

(from Moulson and Herbert, 2003)

Electronic (atomic) polarization arises from a small displacement of the electron clouds with respect to the nucleus.   Electronic polarization is observed in all materials and can follow an oscillating electric field up to frequencies on the order of 10^{15} Hz. Ionic polarization is characterized by the relative displacement of cations and anions. Materials have to be ionic to posses this polarization mechanism.   Ionic polarization contributes to the measured permittivity up to frequencies of $\sim 10^{13}$ Hz.   Dipolar polarization occurs in materials possessing permanent dipoles.   When an electric field is applied to such a material, the permanent dipoles tend to align along the electric field direction, resulting in a finite net polarization.   Dipolar polarization typically contributes to the permittivity for frequencies up to $\sim 10^{8-9}$ Hz.   Space charge polarization is caused by movement of mobile charges until they are stopped by an insulating interface. Because the transport distances can be comparatively long in this case, space charge polarization is relatively slow, and typically responds only to frequencies of 10^2 - 10^6 Hz. It is worthwhile noting that the magnitude of dipolar polarization ($\varepsilon_r \sim 50$ - 10^5) is usually

much larger than the contribution from ionic and electronic polarization ($\varepsilon_r \sim 5$ - 100) (Moulson and Herbert, 2003). This aspect is important when materials with large dielectric constants are required.

Even without an applied electric field, some materials may possess polarization. In piezoelectric materials, a stress can induce a change in the polarization (Jaffe et al. 1973). Some piezoelectric materials have a *spontaneous polarization*, which is a built-in polarization which exists without an applied electric field or stress. These materials are called pyroelectric, meaning that the spontaneous polarization changes as a function of temperature (Jaffe et al. 1973). The following section explains in more detail these classes of materials from the standpoint of symmetry.

2.2 Dielectric Properties and Point Group Symmetry

From the view of symmetry with respect to a point, crystals can be divided into 32 point groups (Newnham, 2005; Nye, 1985). Point symmetry operations include the rotation, identity, mirror, and inversion. Rotation involves a rotation operation about a given axis. If the rotation is n - fold (n = 1, 2, 3, 4, or 6 for crystals), equivalent positions exist at each $(360/n)^o$ rotation. The identity is the case when n = 1, and all crystals include this operation. If the only element of symmetry is the identity operation, the point has no symmetry related points. The mirror plane makes a point symmetry-equivalent with another point an equal and opposite distance from the mirror; for example, for a mirror plane parallel to the z axis, a point (x, y, z) is related to (x, y, -z)

through the mirror plane.   Inversion through the origin relates the point (x, y, z) to (-x, -y, -z).

Neumann's law states that the geometric representation of any physical property must contain the point (or Curie) group symmetry (Newnham, 2005).   As shown in Figure 2.4, 21 out of the 32 point groups are non-centrosymmetric.   Since piezoelectricity is a third rank tensor property, it is not shown in centrosymmetric materials.   In addition, the combined symmetry elements in point group 432 do not allow the piezoelectric effect.   Thus, there are 20 as piezoelectric point groups (Jaffe et al., 1973).   Within the 20 piezoelectric groups, 10 point groups allow a spontaneous polarization.   These 10 groups are the polar groups, and materials with these point group symmetries can be pyroelectric (Jaffe, 1973).   Materials contained within the pyroelectric groups are ferroelectric if the spontaneous polarization can be reoriented between crystallographically equivalent states by the application of a realizable electric field (Lines and Glass, 1977; IEEE, 2003).   It should be obvious that all ferroelectric materials are also pyroelectric, and therefore piezoelectric as well.

All non-magnetic crystals belong to one of the 32 point groups described above. However, amorphous or polycrystalline materials are often employed in practical applications.   Their macroscopic symmetries are categorized into the so called Curie groups (Newnham, 2005).   Figure 2.5 shows the seven Curie group symmetries.   The same arguments as in the 32 point groups can be applied to determine if materials possess pyroelectric and/or piezoelectric properties.   For example, the material with Curie group ∞m should exhibit piezoelectricity as well as pyroelectricity, since the symmetry is non-centrosymmetric and also allows a spontaneous polarization.
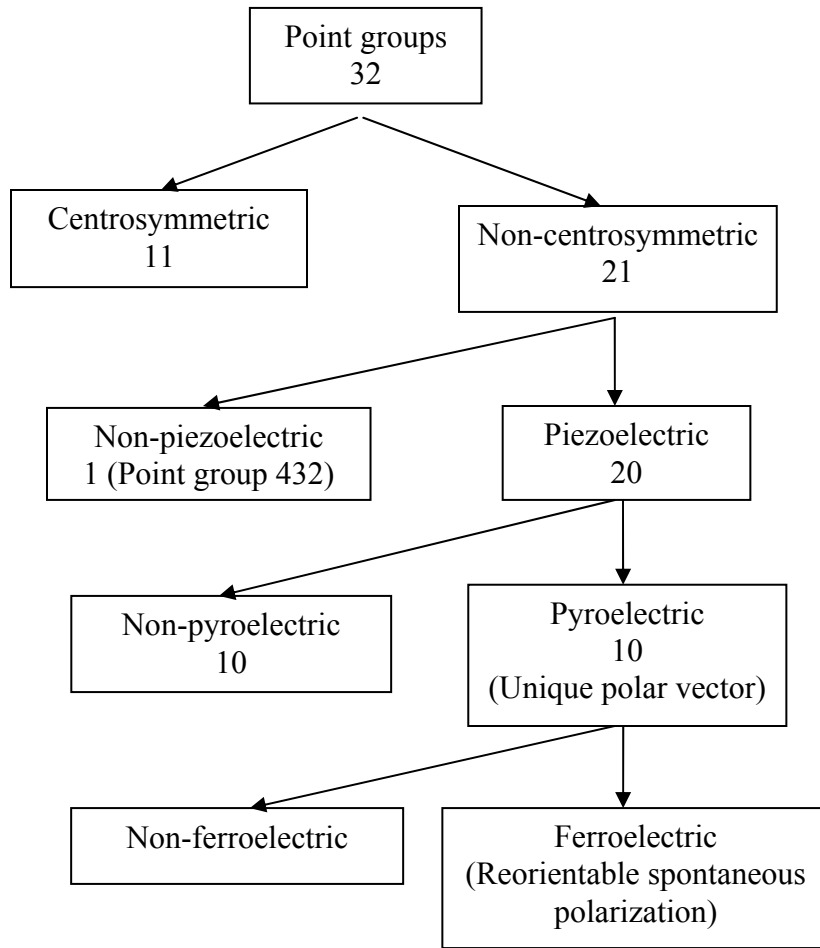
Figure 2.4.   Illustration of the relationship between the properties piezoelectricity, pyroelectricity, and ferroelectricity, for the 32 point groups
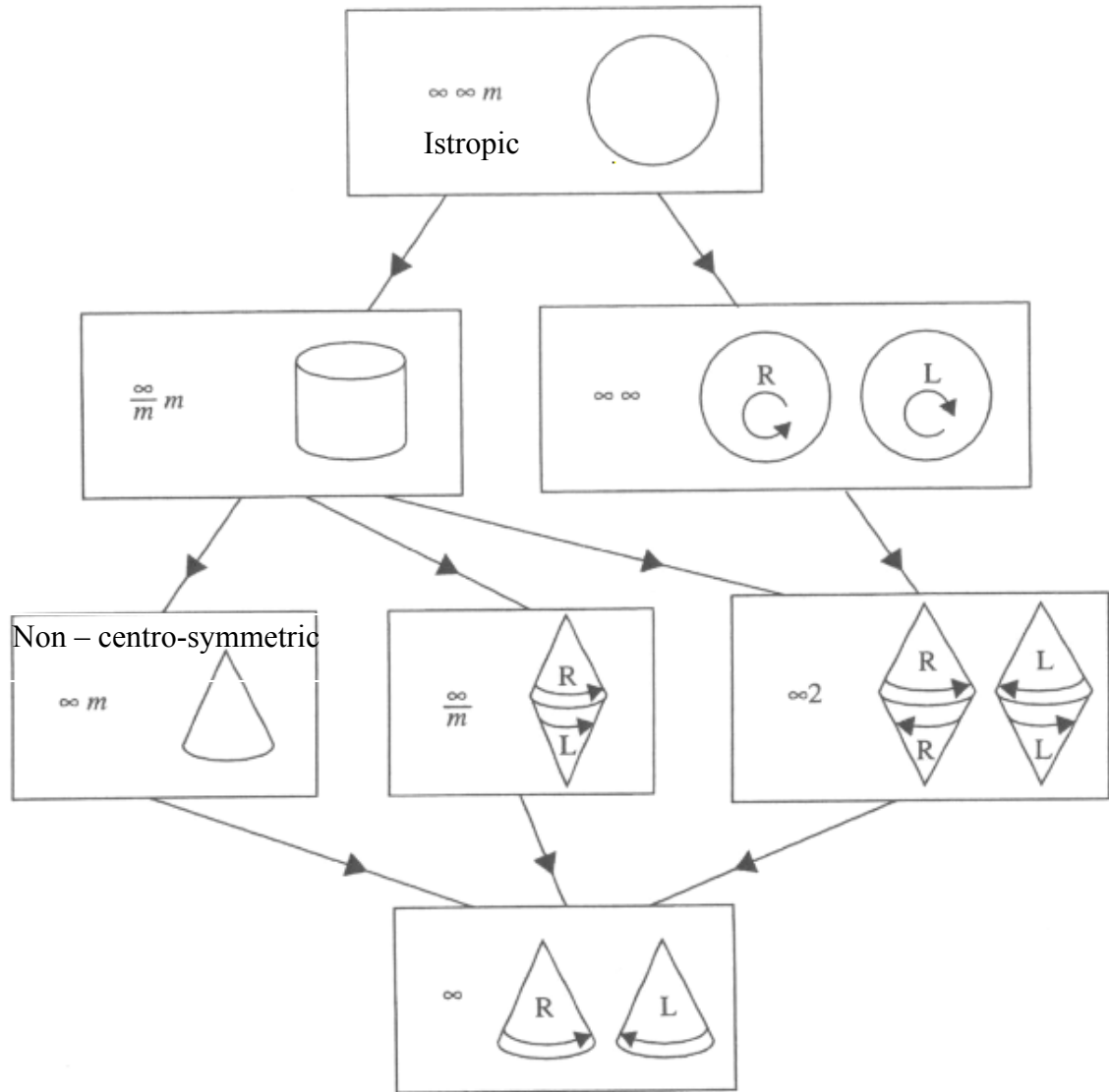
Figure 2.5.   Illustration of the seven Curie groups.   They are represented geometrically
as spheres, cylinders, and cones, with or without handedness (after Newnham, 2005).

2.3 Ferroelectrics

As described in the previous section, ferroelectric materials are a subset of pyroelectric materials.   The ability to reorient the spontaneous polarization between crystallographically defined, energetically equivalent orientations distinguishes ferroelectrics both from other pyroelectric materials and electrets (Lines and Glass, 1977). Electric fields (and sometimes stresses) can re-orient the spontaneous polarization and lead to hysteresis switching.   The Sawyer-Tower circuit (Sawyer and Tower, 1930), shown in Figure 2.6, is an experimental method to observe the polarization switching with an external electric field.   In the circuit, the linear capacitor, C, stores the charge developed in the ferroelectric sample, C_x.   The potential difference on C is applied to an oscilloscope to determine the electrical polarization of C_x as a function of the applied field.   Assuming that the electrical conduction is negligible, the ferroelectric produces a polarization - electric field hysteresis loop (Sinha, 1965).
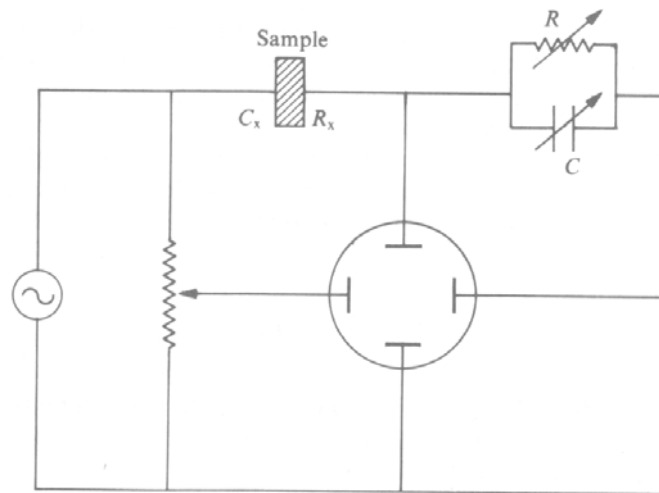
Figure 2.6.   The modified Sawyer-Tower circuit diagram for the ferroelectric

hysteresis observation (after Sinha, 1965; Lines and Glass, 1977)

Figure 2.7 shows a typical hysteresis loop for a ferroelectric and the corresponding domain structures for several points on the loop (IEEE, 2003). Domains are defined as volumes within a crystal with a (nearly) uniform spontaneous polarization. Before application of an electric field (Point A in Figure 2.7), the total polarization in the material is zero. There are three different polarization processes from Point A to Point B in Figure 2.7; at a low applied field, the polarization increases nearly linearly with the applied field. The polarization increases more rapidly at higher applied fields due to the switching of ferroelectric domains. With further increments in the applied field, the polarization increases nearly linearly again as a result of the saturation in polarization, meaning that most of the domains have aligned as well as possible with the direction of the applied field (Point B in Figure 2.7). The remanent polarization, P_r, is the polarization that is retained when the applied field is released to zero (Point C in Figure 2.7). A finite value of polarization remains when there is not a strong driving force to return the domains to their original configuration. The field at which the polarization becomes zero is defined as the coercive field, E_c (Point D in Figure 2.7).
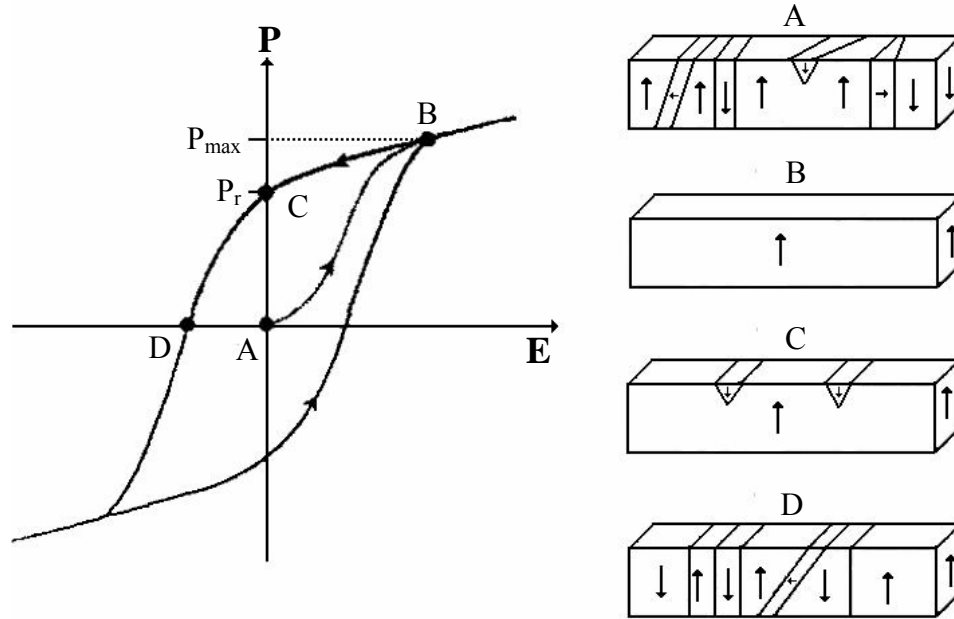
Figure 2.7.   (a) A hysteresis loop of ferroelectric materials representing the remanent

polarization, P_r, and (b) schematics of the corresponding domain structures

(after IEEE, 2003)

Most ferroelectric materials undergo a transition to a high temperature paraelectric phase, where no spontaneous polarization exists (Shuvalov, 1970).   The high temperature phase, often referred to as the prototype phase, has a higher symmetry than the ferroelectric phase.   There are several transition mechanisms, but many industrially important ferroelectric materials undergo a displacive transition.   In many displacive ferroelectric transitions, the relative displacements of anions and cations are driven by a soft lattice mode (Kittel, 2005).

The critical temperature where the ferroelectric- paraelectric transition occurs is called the Curie temperature (Lines and Glass, 1977).   Above T_c, the relative permittivity of proper ferroelectrics follows Curie-Weiss behavior,

$$\varepsilon_r = C / T - \theta \qquad\qquad (2.3)$$

where C is the Curie constant, T is temperature, and θ is the Curie-Weiss temperature. Typically, C is on the order of 10^5 $^{\circ}$C for displacive transitions (Lines and Glass, 1977). The reorientable component of the spontaneous polarization of ferroelectric materials falls to zero at the Curie temperature. Figure 2.8 (a) shows two ways in which the spontaneous polarization falls at the Curie temperature. One is the 1st order transition, in which the spontaneous polarization drops off to zero suddenly at the Curie point, and the other is the 2nd order transition, in which the spontaneous polarization falls continuously to zero at the Curie temperature. As Figure 2.8 (b) illustrates, a discontinuity in entropy at the Curie temperature is characteristic of a 1st order transition. This can be observed as a latent heat in differential scanning calorimetry (DSC). Figure 2.8 (c) shows theoretical dielectric behavior derived from phenomenology. For the 1st order transition, $\theta < T_c$ is expected, whereas $\theta = T_c$ for ferroelectrics undergoing a 2nd order phase transition. Another distinction is that the slope of inverse permittivity below T_c is -8 C for the 1st order and -2 C for the 2nd order transition, which can be derived through phenomelogical theories (Mitsui et al., 1976).
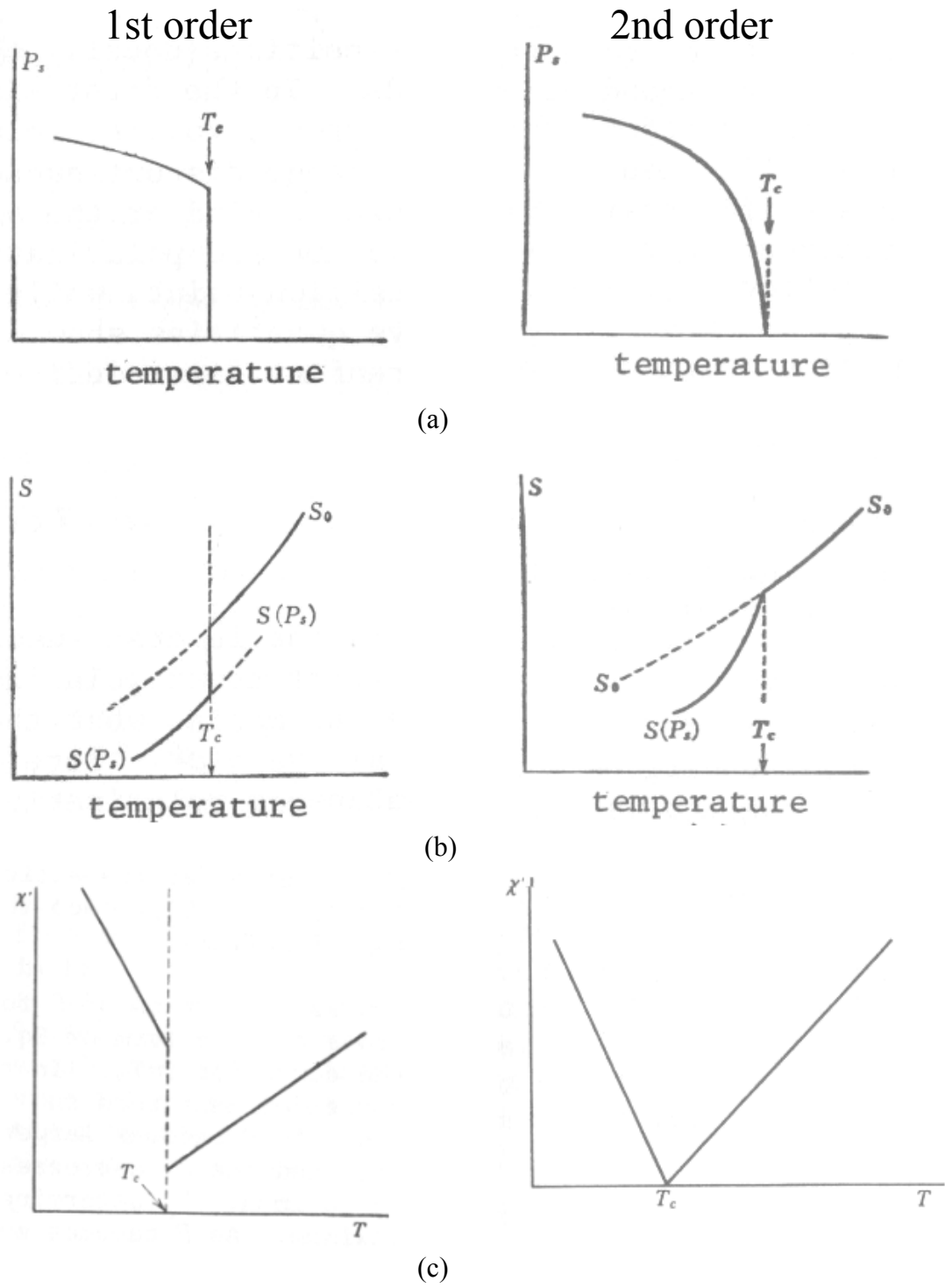
Figure 2.8.   Differences between 1st (on left) and 2nd (on right) order transitions in

(a) spontaneous polarization (b) entropy (c) inverse susceptibility (after Mitsui et al.,

1976)

2.4 Piezoelectrics

In piezoelectric materials, an electrical polarization is proportionally induced by an applied mechanical stress.   The direct piezoelectric effect is represented by:

$$P_i = d_{ijk}\, \sigma_{jk} \qquad\qquad (2.4)$$

where P is the vector quantity polarization, d_{ijk} is the piezoelectric charge coefficient and a 3rd rank tensor, σ is an applied stress and a 2nd tensor, and the subscripts, i, j, k run from 1 to 3 using the Einstein convention.   Piezoelectric materials also exhibit the converse piezoelectric effect.   In this phenomenon, a strain is induced in the material by an applied electric field.   The converse piezoelectric effect is described by:

$$x_{ij} = d_{ijk}\, E_k \qquad\qquad (2.5)$$

where x is the strain developed, and E is an applied electric field.   The piezoelectric coefficient, d, is numerically identical for both direct and converse piezoelectric effects for free boundary conditions (Jaffe et al., 1973).   It should be noted that the notation for the 3rd rank tensor d_{ijk} is often shortened to $d_{ij'}$, where j' = 1, 2, 3, 4, 5, 6 corresponds to jk = 11, 22, 33, 23 or 32, 13 or 31, 12 or 21, respectively (Newnham, 2005; Nye, 1985). For example, d_{33} and d_{31} denote d_{333} and d_{311}, respectively.

Before expressing the intrinsic contributions to the piezoelectric coefficient, we need to consider a more general case of a strain being induced in a dielectric material. This phenomenon is called electrostriction (Jaffe, 1973).   In electrostriction, the induced strain is proportional to the square of the electric field.   In contrast, the strain is linearly proportional to the field for the converse piezoelectric effect (Jaffe, 1973).   Another distinction is that electrostriction is observed in all dielectric materials, whereas

piezoelectricity is allowed only in non-centrosymmetric materials (Jaffe, 1973). Electrostriction can be expressed by:

$$x_{ij} = M_{ijkl} \, E_k \, E_l \qquad (2.6)$$

where the 4th rank tensor M_{ijkl} gives the electrostrictive coefficients in terms of electric field. As explained above, strain is proportional to E^2. Electrostriction can also be described in terms of polarization as:

$$x_{ij} = Q_{ijkl} \, P_k \, P_l \qquad (2.7)$$

where Q_{ijkl} are the electrostrictive coefficients in terms of polarization (also a 4th rank tensor). Here, it should be obvious for linear dielectric that,

$$M_{ijkl} = Q_{ijkl} \, \varepsilon_0^2 \, \varepsilon_r^2 \qquad (2.8)$$

though the relation $P_{induced} \sim \varepsilon_0 \, \varepsilon_r \, E$ for $\varepsilon_r \gg 1$. The total polarization in a ferroelectric is the sum of spontaneous polarization, P_S, and the induced polarization. Considering a simple uniaxial system:

$$P_{total} = P_{induced} + P_S \qquad (2.9)$$

where $P_{induced} \sim \varepsilon_0 \, \varepsilon_r \, E$ when the permittivity is large. P_S is replaced by P_r to account for ceramics and multidomain crystals. Substituting P_{total} into equation (2.7),

$$x = Q \, P_r^2 + 2 \, Q \, P_r \, \varepsilon_0 \, \varepsilon_r \, E + Q \, \varepsilon_0^2 \, \varepsilon_r^2 \, E^2 \qquad (2.10)$$

is obtained. Since the piezoelectric effect is linearly proportional to the applied electric field, equation (2.10) suggests that,

$$d = 2 \, Q \, P_r \, \varepsilon_0 \, \varepsilon_r \qquad (2.11)$$

This implies that materials with high P_r and ε_r should have high piezoelectric coefficients. Although the expression for d obtained from phenomenology provides a good estimate, it should be noted that this expression may underestimate the value of d for ceramics at

some temperatures as it only accounts only for the intrinsic piezoelectric effect. This pure intrinsic case is appropriate for a single domain material. The boundaries between domains, called domain walls, move in response to applied electric fields or stresses, and domain wall movement contributes to the extrinsic piezoelectric (Zhang et al., 1983; Arlt, 1990; Haun, 1988). Thus, the piezoelectric coefficient is given by:

$$d_{total} = d_{intrinsic} + d_{extrinsic} \qquad (2.12)$$

For example, Haun (1988) demonstrated that, in lead zirconate titanate, about half of the room temperature piezoelectric response is extrinsic by separating out the intrinsic contributions from experimental data with the use of phenomenology.

2.5   Perovskite Structure (Tolerance Factor)

The perovskite structure is adopted by many commercially important ferroelectric materials, including barium titanate ($BaTiO_3$) (Megaw, 1973). The ideal perovskite structure has cubic symmetry with ABX_3 stoichiometry, where A is a large cation with a 12-fold coordination to X, B is a smaller cation with a 6-fold coordination to X, and X is an anion with 4 coordination to A and 2 coordination to B, as shown in Figure 2.9 (a) (Megaw, 1957). The structure can be considered as a regular arrangement of corner-connected B octahedra with the A cation occupying the interstice between octahedra (see Figure 2.9 (b)).
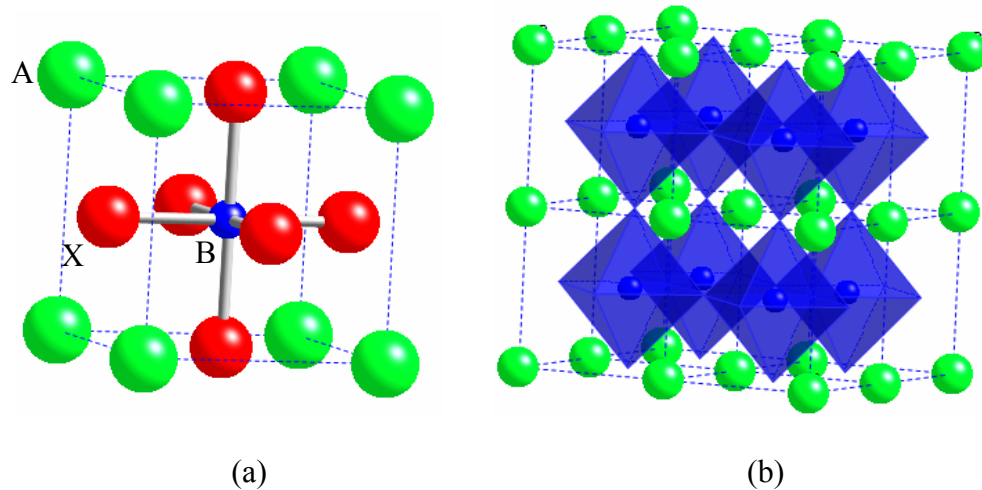
Figure 2.9. The unit cell of the ideal perovskite structure, ABX_3 (a) all atoms are shown, and (b) BX_6 octahedra are emphasized.

At room temperature, many perovskite materials are not in this ideal cubic form but rather are distorted; the cubic symmetry usually can be achieved at high temperatures in the prototype phase (Megaw, 1973). On cooling, transitions from cubic symmetry are observed in many perovskite materials. The phase transitions are often associated with one or more of the following three mechanisms: distortion of the octahedra, tilting of the octahedra, and displacement of ions in the octahedra (Woodward, 1997). Although the focus of this work tends to be on the displacement of ions, as the displacement contributes significantly to the ferroelectric properties, brief descriptions of the other two mechanisms are also provided in the following.

Distortion of the octahedron itself can be caused, for example, by the Jahn-Teller effect in transition metal cations such as high-spin Cu^{2+} or Mn^{3+} (Goodenough, 1998). The Jahn-Teller effect implies, from the point of crystal field theory, that a change from symmetrical to asymmetrical cation-oxygen bondings can lower the free energy of the

material by decreasing the overlap between electrons in the d orbital and the adjacent ligands.

Tilting of octahedra is often observed when the A site ions are relatively small so that they do not adequately fill the interstices between the octahedra. Although the shape and corner connectivity of octahedra are maintained, octahedra tilting (i.e. octahedra can rotate along the a, b, and/or c axes) changes the $B - O - B$ angles from 180°, reducing the interstice volume. Tilting is the most common of these three distortion mechanisms (Glazer, 1972 and 1975; Woodward, 1997).

Displacement of the B site cations in the octahedra can also develop. Some B site cations are too small to sit in the center of their coordination octahedra, and displacement to an off-center position tends to occur. A good example is the displacements of the Ti^{4+} ion in $BaTiO_3$. At room temperature, the Ti^{4+} ion displaces to an off-center position towards one of the six neighboring oxygen ions, which induces a spontaneous polarization and makes the material useful as a ferroelectric material (Moulson and Herbert, 2003).

A convenient method to assess the distortions in a non-ideal perovskite material is through the "tolerance factor". The tolerance factor, t, was first proposed by Goldschmidt (1926) as a measure of the stability of the perovskite phase. It is given by:

$$t = (r_A + r_X) / \sqrt{2} (r_B + r_X) \tag{2.13}$$

where r_A, r_B, and r_X are the ionic radii for A, B and X, respectively (Megaw, 1957). For the case of a solid solution, the ionic radii for each site are simply averaged. From a simple geometrical argument as shown in Figure 2.10, it is clear that an ideal cubic perovskite structure is achieved when $t = 1$.
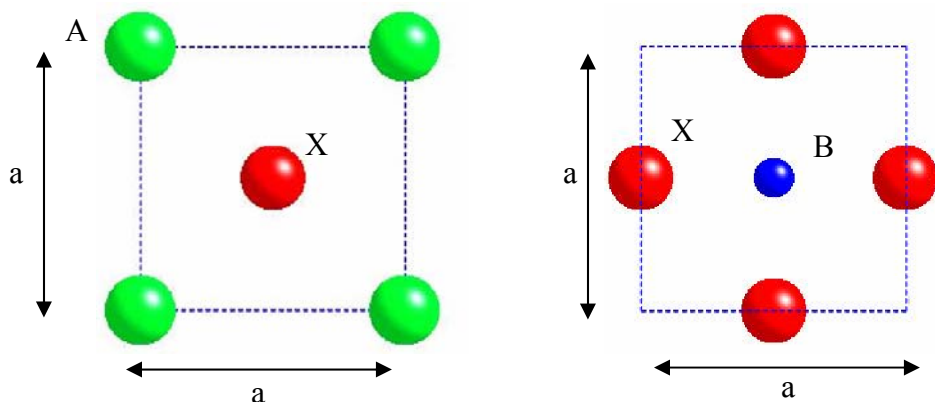
View from (100) plane   View from (200) plane

$$a^2 + a^2 = (2 r_A + 2 r_X)^2 \qquad\qquad a = 2 r_B + 2 r_X$$

$$a = (2 r_A + 2 r_X) / \sqrt{2}$$

Combining the two "a" obtained above,

$$t = (r_A + r_X) / \sqrt{2} (r_B + r_X) = a/a = 1.$$

Figure 2.10.   A schematic showing that the ideal cubic perovskite possesses $t = 1$.

The tolerance factors of the oxides possessing the perovskite structure fall into the range, $0.88 < t < 1.09$ with ambient processing conditions, using Shannon ionic radii corrected for cation coordination numbers (Eitel et al., 2001; Shannon, 1976).   Pressure and epitaxial methods can allow perovskites to be fabricated beyond this range.   The tolerance factor has been widely employed to predict the stability of perovskite solid solutions.   It is also known that ferroelectric perovskites with $t > 1$ tend to be tetragonally distorted, whereas those with $t < 1$ often prefer rhombohedral or monoclinic phases (Isupov, 1983).   It is worth noting that although the tolerance factor provides a good estimation of the stability of the perovskite structure and the type of distortions

23

shown, it is not a perfect predictor for the two following reasons; first, t varies depending on which set of ionic radii is used for the calculation.   Second, t is designed for purely ionic materials, but this is unrealistic since there is a finite amount of covalency in any crystal (Megaw, 1973).   Nonetheless, there are many examples in the literature that successfully explain trends in the physical properties of perovskite material with the tolerance factor.   These include the temperature coefficient of capacitance (Reaney et al, 1994), the transition temperature of Morphotropic Phase Boundaries (MPBs) (Eitel et al., 2001), the phase transition temperature in perovskite materials with colossal magneto-resistance (Goodenough, 1999), the heat of formation (Navrotsky, 1981), and the optical band gap (Lee et al., 2008).

2.6   Relaxor Ferroelectrics

Relaxor ferroelectrics are distinguished from normal ferroelectrics in terms of their phase transition, polarization, and dielectric behavior (Cross, 1987).   Figure 2.11 illustrates the distinct features of relaxor ferroelectrics with a normal ferroelectric for comparison.

Normal Ferroelectric		Relaxors
(a)		
• Macro-size FE domains		• Nano-size polar domains
(b)		
• No polar domains above T_c		• Nano-size polar domains persist well above T_m
(c)		
•sharp narrow transitions		• very broad $\varepsilon'(T)$ peaks
•$\varepsilon'(T)$ follows Curie-Weiss law		• strong deviation from Curie-Weiss law
•No frequency dispersion		• strong frequency dispersion
• 1st - or 2nd - order phase transition with macroscopic symmetry change at T_c		• No structural phase transition across T_m
• Strong optical anisotropy across T_c		• Critical slowing down of dipolar motion below T_m
		• No optical anistropy across T_m

Figure 2.11.   Differences in dielectric characteristics between normal and relaxor

ferroelectrics (a) hysteresis loop, (b) spontaneous polarization, and (c) dielectric constant

(from Samara, 2003).

25

The dielectric maximum in relaxor ferroelectrics is frequently broad, shown in Figure 2.11 (c), whereas homogeneous normal ferroelectrics have a sharp phase transition. A local polarization exists above the temperature for the maximum permittivity, T_{max} (see Figure 2.11 (b)).   The frequency dependence of the dielectric constant below T_{max} (with convergence above T_{max}) distinguishes a relaxor ferroelectric both from a normal ferroelectric, and from dielectrics with strong space charge contributions (which are dispersive both above and below T_{max}).   In relaxors, T_{max} decreases as the measurement frequency decreases (Smolensky, 1970).

It is believed that intermediate range (~ 100Å) cation ordering on one site in the structure is essential for the formation of relaxors (Randall and Bhalla, 1990).   Below T_{max} the polarization also develops only over a small characteristic length scale, yielding micropolar regions.   In contrast, normal ferroelectrics show long range order in the polarization (Cross, 1987).

Relaxor behavior is often observed in complex perovskite compounds.   Two typical ways are known to achieve relaxor behavior in ferroelectric perovskites.   One way is to introduce short - intermediate range order in the B site cations, with a general chemical formula $A(B'B'')O_3$ (Randall and Bhalla, 1990).   Examples of the B-site complex perovskites include $Pb(Mg_{1/3}Nb_{2/3})O_3$ and $Pb(Sc_{1/2}Ta_{1/2})O_3$.   The complexity on the B-site yields short range order of dipoles, resulting in the relaxor behavior.   A site relaxors such as lanthanum doped PZT ($Pb_{1-3x/2}La_x(Zr_{1-y}Ti_y)O_3$) (Viehland et al., 1992) also exist.   Here the La^{+3} ion and A-site vacancies contribute to breaking the translational order and limiting long range dipolar ordering.

2.7 Morphotropic Phase Boundary (MPB)

A Morphotropic Phase Boundary (MPB) has been defined as a temperature independent boundary between two different phases (Jaffe et al., 1955).   Pb(Zr,Ti)O$_3$ (PZT), developed in the 1950's, is one of the most widely studied and used piezoelectric materials.   In PZT, the MPB between tetragonal and rhombohedral phases occurs when the molar ratio PbZrO$_3$:PbTiO$_3$ is close to 1:1 (see Figure 2.12).   At the MPB composition, a peak in the polarizability results in maxima in the relative permittivity, the piezoelectric constants, and the electromechanical coupling coefficient, k, (measure of how much mechanical energy can be converted to electrical energy or vice versa), as shown in Figure 2.13 (Haun et al., 1989).
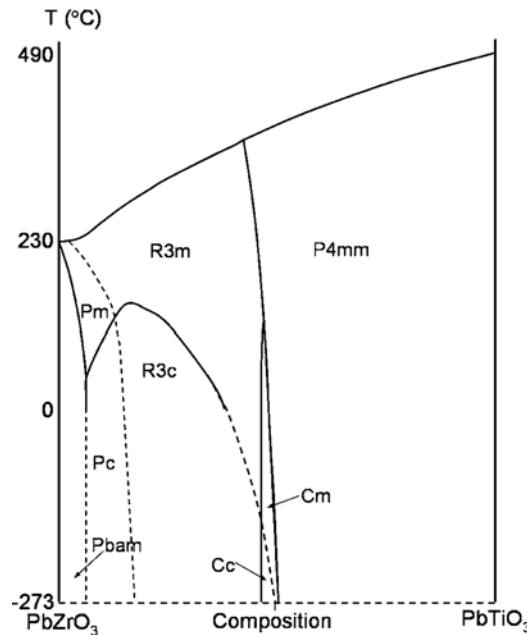
Figure 2.12.   Phase diagram of PbZr$_x$Ti$_{1-x}$O$_3$ solid solution (from Woodward et al., 2005).
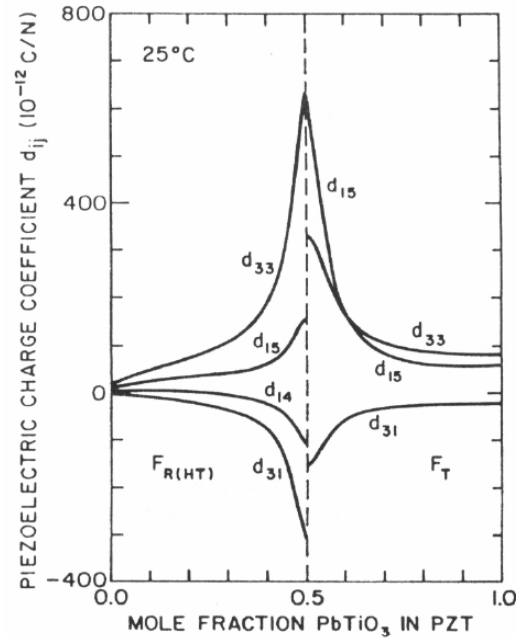
Figure 2.13.   Calculated piezoelectric coefficient for various compositions in

$PbZr_xTi_{1-x}O_3$ solid solution (from Haun et al., 1989)

2.8   Non Lead Piezoelectrics

In the previous section, the useful piezoelectric properties in PZT around its MPB were mentioned.   However, there is a considerable body of existing literature on lead-free piezoelectric alternatives to PZT due to environmental concerns about lead oxide based materials (Takenaka and Nagata, 2005).   Good examples of non lead ferroelectric piezoelectrics include $(Bi_{1/2}Na_{1/2})TiO_3$ (BNT) - based materials (Takenaka et al., 1999) and $(K_{1/2}Na_{1/2})NbO_3$ (KNN) - based materials (Matsubara et al. 2005).   Table 2.1 compares the performance of existing lead-free piezoelectric materials (Shrout and Zhang, 2007).   These materials may be acceptable for some piezoelectric applications (as in resonators), but their piezoelectric performance is still inferior to that of PZT for

actuator applications, which typically required d_{33} values > 300 pC/N (with the exception that KNN-LF4 shows a d_{33} value of 410 pC/N).

Table 2.1.   Dielectric and piezoelectric properties on existing lead-free perovskite materials (from Shrout and Zhang, 2007). k_p denotes the planar coupling coefficient.

Material	$\varepsilon_r/\varepsilon_0$	Loss	d_{33} (pC/N)	k_p	k_{33}	T_c (°C)	T_{O-T}/T_d (°C)
BaTiO$_3$	1,700	0.01	190	0.36	0.5	115	0
BaTiO$_3$-CaTiO$_3$-Co	1,420	0.005	150	0.31	0.46	105	−45
(K$_{0.5}$Na$_{0.5}$)NbO$_3$ (HP)	500	0.02	127	0.46	0.6	420	
(K$_{0.5}$Na$_{0.5}$)NbO$_3$	290	0.04	80	0.35	0.51	420	195
KNN-Li (7%)	950	0.084	240	0.45	0.64	460	~20
KNN-Li3%; Ta20% (LF3)	920–1,256	0.024–0.02	190–230	0.46–0.505	0.62	310–323	50–70
KNN-LF4[a]	1,570	/	410	0.61	/	253	25
KNN-SrTiO$_3$ (5%)	950	/	200	0.37	/	277	27
KNN-LiTaO$_3$ (5%)	570	0.04	200	0.36	/	430	55
KNN-LiNbO$_3$ (6%)	500	0.04	235	0.42	0.61	460	70
KNN-LiSbO$_3$ (5%)	1,288	0.019	283	0.50	/	392	45
NBT-KBT-LBT	1,550	0.034	216	0.401	/	350	160
NBT-KBT-BT	820	0.03	145	0.162	0.519	302	224
NBT-KBT-BT (MPB)	730	0.02	173	0.33	0.59	290	162
NBT-KBT-BT	770	0.034	183	0.367	0.619	290	100
NBT-BT	665	0.028	64 (d_{31})	0.28(k_{31})	/	/	/
NN-BT10%	1,000	0.015	147	/	/	235	/
NBT-KBT50%	825	0.03	150	0.22	/	320	210
SBT-KBT90	870	0.04	110	0.15	0.507	296	/
SBT-KBT85	1,000	0.05	120	0.16	0.491	250	/
BBT-KBT90	837	0.05	140	0.23	0.538	297	144
BBT-KBT80	630	0.04	95	0.15	0.361	290	238
Sr$_2$NaNb$_5$O$_{15}$[a]	1,100	/	120	/	/	280	/

[a] Textured ceramics; T_{O-T}: Orthorhombic to tetragonal phase transition; HP: Hot Pressed; NN: NaNbO$_3$; NBT: (Na$_{0.5}$ Bi$_{0.5}$)TiO$_3$; KBT: (K$_{0.5}$ Bi$_{0.5}$)TiO$_3$; LBT: (Li$_{0.5}$Bi$_{0.5}$)TiO$_3$; BT: BaTiO$_3$; SBT: (Sr$_{0.7}$Bi$_{0.2}$)TiO$_3$; BBT: (Ba$_{0.7}$Bi$_{0.2}$)TiO$_3$; KNN: (K$_{0.5}$Na$_{0.5}$)NbO$_3$; T_d: depolarization temperature.

The outstanding material, KNN-LF4 in Table 2.1, was reported by Saito et al., based on (K$_{1/2}$Na$_{1/2}$)NbO$_3$ modified with LiTaO$_3$ and LiSbO$_3$.   The material shows a significant improvement in piezoelectric performance relative to other lead-free compositions, and is competitive with PZT ceramics at room temperature (Saito et al., 2004).   Figure 2.14 and Table 2.2 show the dielectric behavior and typical piezoelectric coefficients, respectively.   In order to achieve d_{33} values > 300 pC/N, however, the

polycrystals must be <001> textured. At present, it is not clear if the templated grain growth process used to produce the texture is suitable for low cost mass production. In addition, the properties are enhanced only near the polymorphic transition and there is not a proper MPB, so temperature stability and depoling will be problematic. There may be some applications with limited temperature ranges to which these non-lead materials can contribute, however, it is doubtful that these materials could replace PZT for a multilayer actuator application that requires high temperature and large strain requirements.

(a)   (b)
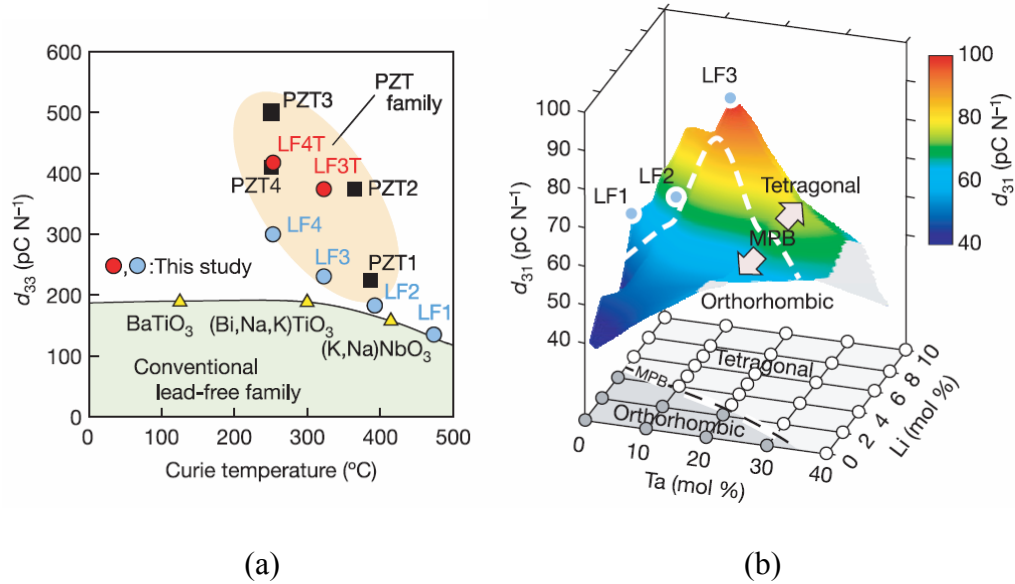
Figure 2.14.   Piezoelectric performance of $\{(K_{0.5}Na_{0.5})_{1-x}Li_x\}(Nb_{1-y}Ta_y)O_3$ ceramics, (a) comparison of d_{33} value and Curie temperature with other non-lead materials and PZT, (b) d_{31} value at room temperature as a function of Ta and Li concentration (from Saito et al., 2004).   Note that what is marked as a MPB is, in fact, a polymorphic phase transition.

Table 2.2.   Room temperature piezoelectric coefficients for

$(K_{0.44}Na_{0.52}Li_{0.04})(Nb_{0.86}Ta_{0.10}Sb_{0.04})O_3$ <001> textured ceramics and a commercial

PZT(from Saito et al., 2004)

Piezoelectric property		LF4T	PZT4
Curie temperature	T_C (°C)	253	250
Piezoelectric coupling constant	K_p	0.61	0.60
Piezoelectric charge sensor constant	d_{31} (pC N^{-1})	152	170
	d_{33} (pC N^{-1})	416	410
Piezoelectric voltage constant	g_{31} (10^{-3} V m N^{-1})	11.0	8.3
	g_{33} (10^{-3} V m N^{-1})	29.9	20.2
Dielectric constant	$\varepsilon_{33}^T / \varepsilon_0$	1,570	2,300
Normalized strain	S_{max} / E_{max} (pm V^{-1})	750	700

One of the major misleading aspects in Table 2.2 is that the T_c is not always the relevant transition. T_{O-T} (orthorhombic – tetragonal transition), the transition temperature for the polymorphic phase transition that enhances the properties, is much lower.

2.9   BiScO$_3$ – PbTiO$_3$ Ceramics and BaTiO$_3$ - BiScO$_3$ Thin Films

Bi based piezoelectrics may be interesting as an alternative to PZT, as Bi^{3+} has a lone electron pair and so promotes both ferroelectricity and a high polarizability.

High piezoelectric performance in BiScO$_3$ – PbTiO$_3$ coupled with a high Curie temperature was discovered by Eitel et al. (2001).   BiScO$_3$ – PbTiO$_3$, like PZT, utilizes compositions near a MPB between rhombohedral and tetragonal phases to enhance the properties.   Simple crystal chemistry arguments with the tolerance factor were used to target potential MPB systems; MPBs often develop at compositions near t = 1, since

materials with t > 1 and t < 1 prefer tetragonal and lower symmetry distortions (often rhombohedral or monoclinic), respectively (Eitel et al., 2001). This system is attractive due to its high piezoelectric performance with reduced amount of lead use, but it not lead-free.

A comparable methodology was applied to selection of compositions in the (1-x) $BaTiO_3$ - x $BiScO_3$ system to explore non-lead dielectric thin films (Tinberg and Trolier-McKinstry, 2007). A relative permittivity up to 800 was observed for the films, depending on composition. Figure 2.15 shows the dielectric constant and loss tangent vs. temperature plot for a 0.6 $BaTiO_3$ – 0.4 $BiScO_3$ film, showing a highly diffusive and dispersive dielectric behavior. A pure perovskite phase was achieved in the films with x = 0.2-0.45, even without epitaxy, which suggests that a stable perovskite phase could be prepared in bulk ceramics as well.
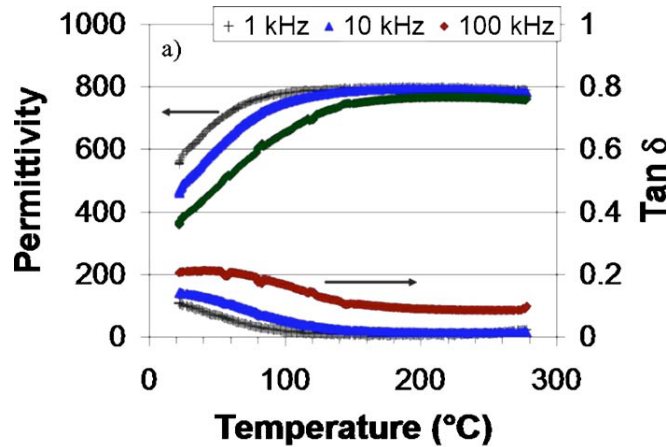
Figure 2.15. Dielectric constant and loss tangent vs. temperature for 0.6 $BaTiO_3$ – 0.4 $BiScO_3$ film (after Tinberg and Trolier-McKinstry, 2007).

2.10 Off-center Ion Doping

If a normal ferroelectric can be developed in the highly polarizable $BaTiO_3$ - $BiScO_3$ system as explained in the last section, the material may become more suitable for piezoelectric applications. Previous research suggests that in some highly polarizable dielectrics, doping with ions that tend to off-center, such as Li, can stabilize a long-range polarization (Vugmeister and Glinchuk, 1990). For example, pure $KTaO_3$ is an incipient ferroelectric that remains in a paraelectric state down to 0 K. However, when $KTaO_3$ is doped with Li or Na, it exhibits a ferroelectric transition (see Figure 2.16) (Davis, 1972; DiAntonio et al., 1993). Li in $KTaO_3$ tends to adopt an off-center position in the lattice due to its small ion size, as shown in Figure 2.17. Once the Li ion displaces from the high symmetry positions, it produces an electric dipole moment. If the Li ion concentration is small, the dipolar correlation length, r_c, is much shorter than the distance between the dipoles created by the Li doping. In this case, the dipoles do not interact with each other and no net polarization is induced. However, when the Li ion concentration is large enough so that r_c becomes comparable to the separation distance between dipoles, the dipoles start interacting each other, forming dipolar domains and inducing polarization (Vugmeister and Glinchuk, 1990).
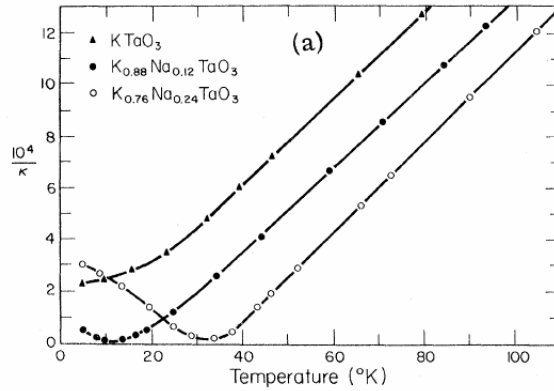
Figure 2.16.   Inverse dielectric constant vs. temperature for Na-doped $KTaO_3$ showing

Curie – Weiss behavior (from Davis, 1972).
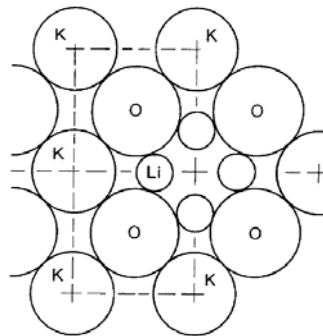
Figure 2.17.   [001] plane view of $KTaO_3$ showing the off-center position of Li ion (from

Hochli et al., 1990)

Another example of a high temperature ferroelectric transition obtained with Li

doping is the work on $Ag(Nb_{1/2}Ta_{1/2})O_3$ and $AgNbO_3$ by Sakabe et al. (2001).   Pure

$Ag(Nb_{1/2}Ta_{1/2})O_3$ and $AgNbO_3$ undergoes a series of ferroelastic transitions over a wide

range of temperature, becoming ferroelectric only at about -125 and 60 ^{o}C, respectively.

34

Li doping stabilizes a normal ferroelectric at room temperature with a square hysteresis loop, as shown in Figure 2.18.

(a)   (b)
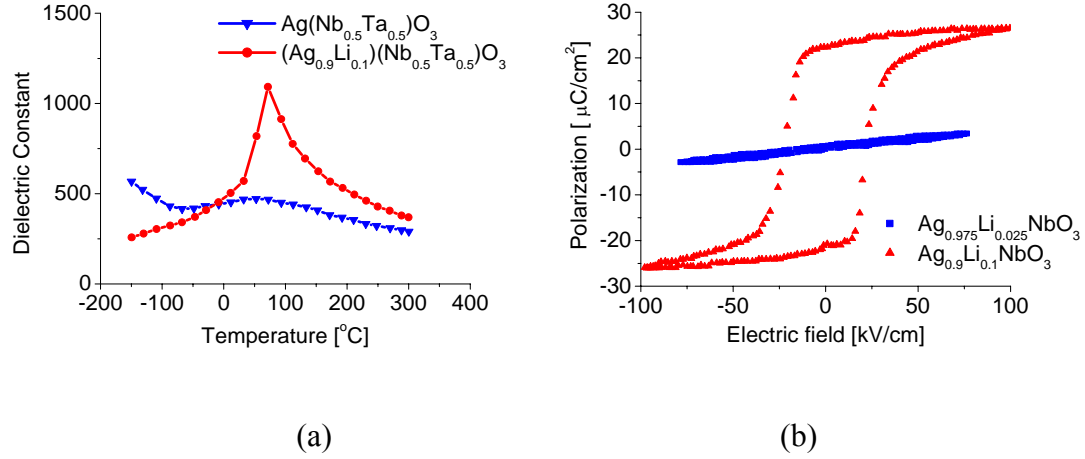
Figure 2.18. Dielectric behavior for Li-doped $Ag(Nb_{1-x}Ta_x)O_3$ ceramics, (a) dielectric constant vs. temperature and (b) polarization vs. electric field (after Sakabe et al., 2001)

2.11 High Energy Density Capacitor Application

The highly diffusive and dispersive dielectric behavior observed in $BaTiO_3$ - $BiScO_3$ thin films (described in section 2.9) may be useful in capacitor applications. Dielectric capacitive materials are used for charge storage and supply and modifying impedance.   In high field applications, the non-linear behavior of the dielectric materials often limits the energy storage capabilities.   A useful figure of merit is the total energy storage capability at high field (Burn and Smyth, 1972).   The stored electrical energy is expressed as,

$$J = \int_0^{D_{max}} E \, dD \qquad (2.14)$$

35

where J is the energy density, E is the electric field, D is the electric displacement, and D_{max} denotes the displacement at the highest applied field, E_{max}. For an ideal lossless linear dielectric material, the energy density is given by the shaded area in Figure 2.19 (a):

$$J = 1/2 \ D_{max} \ E_{max} \ \text{(for linear dielectrics)} \qquad\qquad (2.15)$$

However, Figure 2.19 (b) and (c) indicate that for ferroelectric and antiferroelectric materials, there are dielectric losses, hysteresis, and non-linearities, so the calculation is more complex (Jaffe, 1961). As described in section 2.1, for the materials employed in this thesis, $D \sim P$, since $\varepsilon_r \gg 1$.
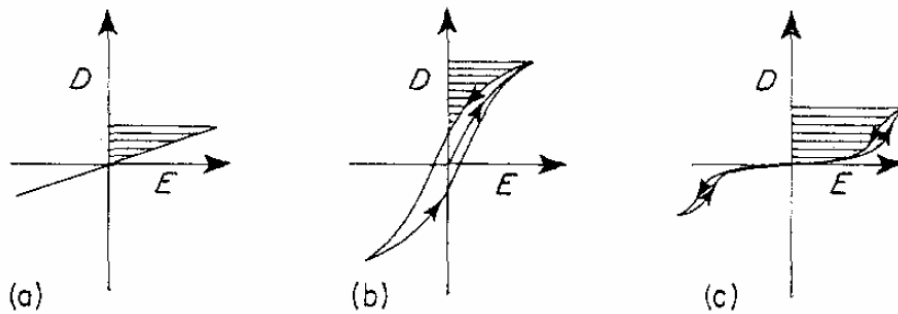
Figure 2.19. Displacement vs. electric field for (a) linear dielectrics, (b) ferroelectrics, and (c) antiferroelectrics. The shaded area is the recoverable energy density (after Burn and Smyth, 1972).

Various kinds of dielectric materials have been investigated for high energy density applications. Figure 2.20 compares the energy storage capability for various types of materials. Most of the data shown are for linear dielectrics, including those used in electrolytic capacitors, mica, and most of the polymers (wa Gachigi, 1997).

Although these materials possess relatively low dielectric constants ($\varepsilon_r \ll 100$), high energy density ($J > 10$ J/cm^3) can be achieved due to their high dielectric breakdown strength. On the other hand, ferroelectric ceramics exhibits high dielectric constant, but the energy density values are lower due to the low dielectric breakdown strength in ceramics and the energy loss from the hysteresis behavior (wa Gachigi, 1997).
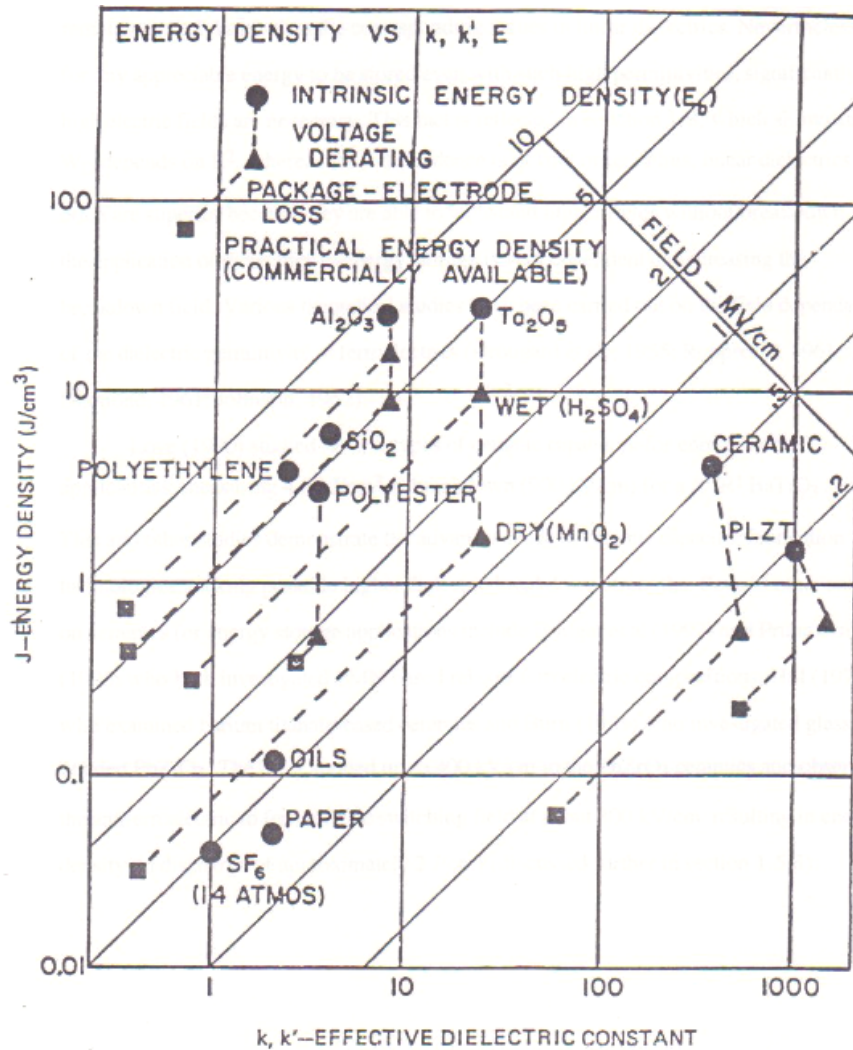
Figure 2.20. Energy density capability for various types of materials as a function of dielectric constant and applied electric field (from wa Gachigi, 1997; Shirn and Burn, 1972)

37

Over the last several decades, capacitors based on high permittivity ceramics have been shown to possess energy density values close to linear dielectric capacitors (Love, 1990). The advances developed as a result of improved processing, resulted in higher dielectric breakdown strength, pushing up the achievable energy values. For example, one type of $BaTiO_3$ based X7R capacitor showed $\sim$ 5 J/cm^3 at 80 kV/mm, which is close to the breakdown strength of 90 kV/mm for the material (Love, 1990).

The dielectric breakdown strength in ferroelectric ceramics is often dominated not by intrinsic material property but extrinsic effects such as sample geometry, electrode shape, and the homogeneity of the sample. Although there are several major mechanisms for breakdown in ceramics, thermal breakdown often dominates (Moulson and Herbert, 2003). In this mechanism, Joule heating results from the finite current flow in a dielectric. If the rate of heat generation is faster that the rate of heat dissipation, the material becomes less resistive, increasing the current flow. Eventually, the cycle leads to breakdown of the material. This thermal breakdown mechanism is known to be sample thickness dependent (i.e. dielectric breakdown strength $\propto d^{-1/2}$, where d is the sample thickness).

The temperature dependence of the dielectric properties also needs to be considered when capacitors are employed in industrial devices. A stable capacitance over the working temperature range is essential. TCC ($^oC^{-1}$), temperature coefficient of capacitance, is often employed as a figure of merit for capacitor design. TCC can be described by,

$$TCC = (1/c)\,(dc/dT) \qquad\qquad (2.16)$$

where c is capacitance and T is temperature. Most linear dielectric materials possess low TCC over a wide range of temperature (with the limitation that polymer based materials do not tolerate high temperatures). However, for ferroelectric capacitors, the temperature stability is often limited due to the phase transitions, such as ferroelectric-paraelectric and ferroelastic transitions. Therefore, it is essential to carefully design the material so that the capacitance becomes stable over a desired temperature range.

2.12   Outline of the thesis

Here, the organization of the following chapter is briefly explained.

Chapter 3 reviews the details of the material processing. The experimental technique and approaches used to characterize the solid solution phases, microstructure, and electrical properties are also described.

Chapter 4 presents the experimental results and discussion. The first part emphasizes the structural and dielectric properties of base $BaTiO_3 - BiScO_3$ ceramics. Secondly, the results on single dielectric layer $0.7\ BaTiO_3 - 0.3\ BiScO_3$ capacitors are presented, and the feasibility for the high energy density capacitor application based on this system is discussed. Lastly, attempts to stabilize a normal ferroelectric with off-center ion doping are described.

Chapter 5 summarizes the important findings of scientific and technological perspectives. The final point of the chapter outlines possible directions of future work.

Chapter 3: Experimental Procedure

3.1   General Sample Preparation

Ceramic samples were prepared by conventional solid state ceramic processing. Powders were made at different points across the solid solution batched to the required stoichiometries and were then milled and heat treated to form the perovskite phase.   The powders were formed into solid, dense, polycrystalline materials; pellet pressing and tape casting were employed to prepare green ceramic bodies, followed by sintering.

3.1.1   Powder Preparation

(1-x) $BaTiO_3$ - x $BiScO_3$ powder was prepared from reagent grade powders of barium carbonate ($BaCO_3$, 99.0%, Alfa Aesar), titanium oxide (TiO_2, 99.97%, 0.25μm, Ishihara), bismuth oxide (Bi_2O_3, 99.9%, MCP), and scandium oxide (Sc_2O_3, 99.0%, The Low Hanging Fruit Company).   For compositions with possible off-center ions, Li, K, and Na, lithium carbonate (Li_2CO_3, 99%, Alfa Aesar), sodium carbonate (Na_2CO_3, 99.95%, Alfa Aesar), potassium carbonate (K_2CO_3, 99.0%, Alfa Aesar), and niobium pentoxide (Nb_2O_5, 99.8%, Reference Metals) were employed.

Figure 3.1 is the flow chart for the powder preparation.   Raw materials were batched for the desired composition stoichiometrically, and mixed in an aqueous solution with 0.2 vol% ammonium hydroxide (J. T. Baker) and 0.5 vol% dispersant (Darvan 821A) to reduce the flocculation of the powders.   The solution was then ball milled with stabilized zirconia media (cylindrical with ~ 9mm height and 9 mm diameter, TOSOH Ceramics) for 24 hours.   After drying the suspension at 130 ^{o}C, the powder mixture was

calcined in air for 4 hours at 700°C to 1000°C as shown in Table 3.1. For better homogeneity, the powder was mixed in the same aqueous solution mentioned above with the media, vibratory milled for 18 hours, and dried at 130 ^{o}C before a second calcination in air for 4 hours.   Vibratory milling was employed for the second milling to crush agglomerates into finer powders.   After checking for the formation of the perovskite phase by using X-ray diffraction (XRD), the calcined powder was again vibratory milled with the media and dried as described before preparing ceramic compacts.

Figure 3.2 shows X-ray patterns for x = 0.1 after the 1st and 2nd calcinations steps and for x = 0.3 after the 2nd calcination.   After the 1st calcination, all compositions showed residual $BaCO_3$ (ICDD PDF #00-005-0378) as shown in Figure 3.2 (a).   The 2nd calcination step yielded almost phase-pure perovskite for the compositions x = 0 - 0.3 (see Figure 3.2 (b)).   However, the 2nd compositions with x = 0.4 or more were not phase pure.   As seen in Figure 3.2 (c), samples with x = 0.4 showed peaks from a $Bi_{12}TiO_{20}$ (ICDD PDF #00-034-0097) second phase.   The undesired peaks were reduced during the sintering process, but some of them could not be removed from the system (See section 4.1.2 for details).

Batch raw materials stoichiometrically:
Raw materials: $BaCO_3$, TiO_2, Bi_2O_3, Sc_2O_3
(For off-center doping, Li_2CO_3, Na_2CO_3, K_2CO_3, Nb_2O_5)
Compositions: $(1-x)\ BaTiO_3 - x\ BiScO_3$ with $x = 0$ to 0.5

1 vol% of dispersant
30 vol% of 1.4% NH_4OH
200 vol% of distilled water

Ball mill for 24 hr

Dry at 130 ^{o}C

Grind the powders

Calcine

700 ~ 1000 ^{o}C for 4 hours

Calcination profile

Repeat until desired phase achieved

X-ray diffraction for phase determination

1 vol% of dispersant
30 vol% of 1.4% NH_4OH
200 vol% of distilled water

Ball mill for 18 hr and dry at 130 ^{o}C

Grind and screen through 80 mesh

Figure 3.1.   Flow chart for the powder preparation with the profile for calcination

Table 3.1.   Calcination and sintering temperatures for each composition.   Note that 2
temperatures in one calcination step mean 2 hours at each temperature (total 4 hours).

sample	Composition		Temperature (^{o}C)		
	1-x (BaTiO$_3$)	x BiScO$_3$	1st calcination	2nd calcination	Sintering
1	1	0	800	1000	1320
2	0.999	0.001	700, 850	750, 900	1300
3	0.998	0.002	700, 850	750, 900	1300
4	0.997	0.003	700, 850	750, 900	1300
5	0.996	0.004	700, 850	750, 900	1300
6	0.995	0.005	700, 850	750, 900	1300
7	0.99	0.01	700, 850	750, 900	1300
8	0.98	0.02	700, 850	750, 900	1300
9	0.97	0.03	700, 850	750, 900	1300
10	0.96	0.04	700, 850	750, 900	1300
11	0.95	0.05	800	700, 850	1300
12	0.925	0.075	800	700, 850	1300
13	0.9	0.1	800	700, 850	1300
14	0.85	0.15	800	700, 850	1300
15	0.8	0.2	800	700, 850	1300
16	0.7	0.3	800	700, 850	1250
17	0.6	0.4	800	700, 850	1150
18	0.5	0.5	800	700, 850	1050
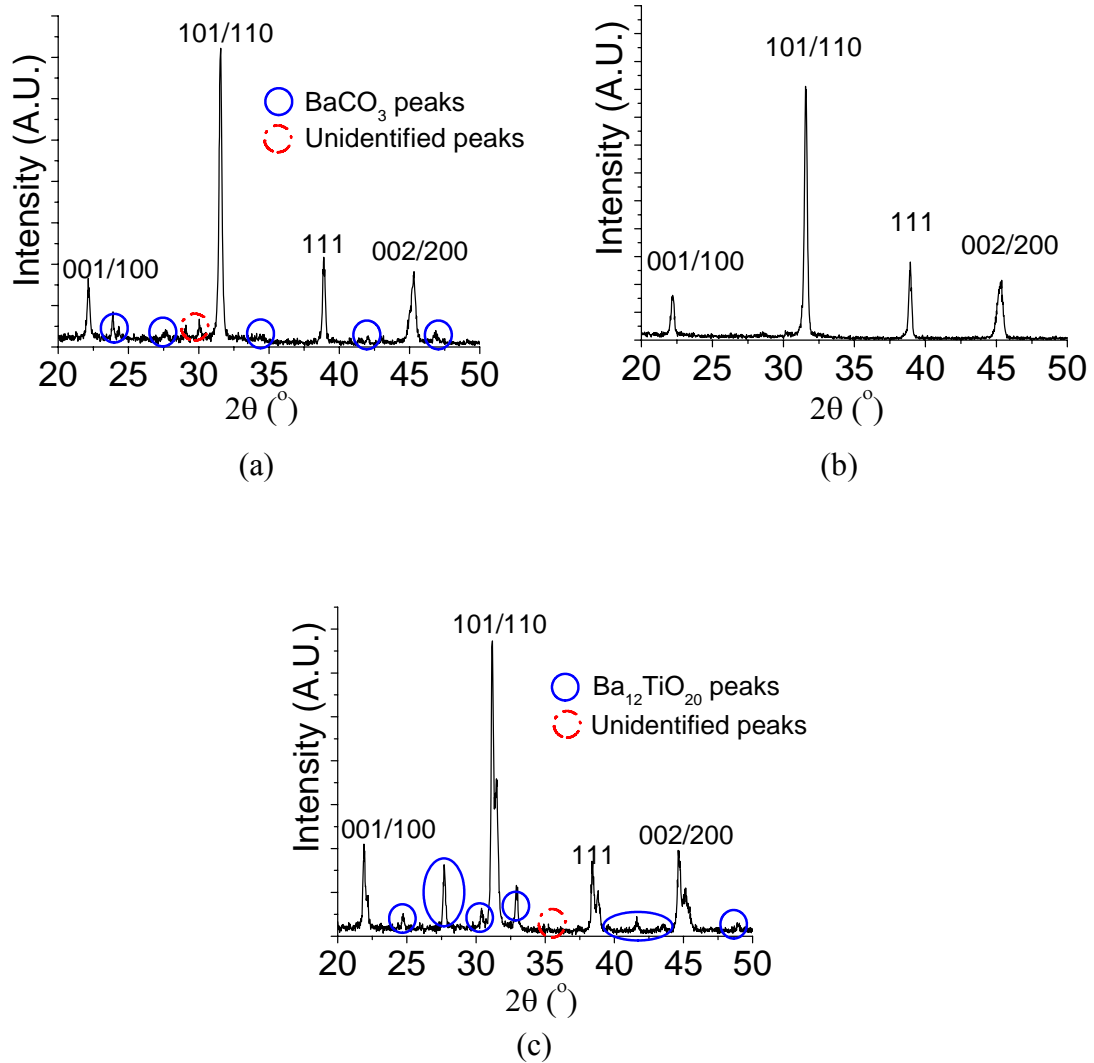
Figure 3.2.   X-ray diffraction patterns for calcined $(1-x)$ BaTiO$_3$ - x BiScO$_3$ powder, (a)

$x = 0.1$ after 1st calcination, (b) $x = 0.1$ after 2nd calcination, and (c) $x = 0.3$ after 2nd

calcination.   The peak indexing is based on either tetragonal or pseudocubic perovskite

unit cells.

3.1.2 Pellet Preparation

Figure 3.3 is the flow chart for pellet preparation.   The calcined powder was mixed with 3-4 wt% acrylic binder (Acrylic Resin, Rohm and Hass) to increase the green strength of the compacts, pulverized, and sieved through a mesh screen with 180 μm openings.   The powder was uniaxially pressed at 70 MPa to form disks 13 mm in diameter and about 1mm in thickness.   The binder was burned out at 325 ^{o}C for 90 min and at 550 ^{o}C for 60 min.   Samples were then cold isostatic pressed at 200 MPa to increase the green density.   The pellets were subsequently sintered at 1050 - 1320 ^{o}C, as shown in Table 1, for 1 – 20 hours in a closed crucible with a source powder of the same composition to minimize bismuth loss due to its volatility.   The exception was the samples with x = 0 which were sintered in a clean furnace with an O_2 rich but open environment.   The weight loss during sintering was confirmed to be less than 1% for all samples.

In order to achieve densities higher than 95% theoretical density for the electrical measurements, an additional 3 mol % Bi_2O_3 was added as a sintering aid at the same time as the binder for samples with x = 0.001 to 0.15. Bi_2O_3 has a melting temperature of about 825 ^{o}C (Weast, 1976), which is lower than the sintering temperatures employed in this study, so the excess Bi_2O_3 was believed to improve the density through liquid phase sintering.   Weight loss measurement suggested that more than two third of the excess Bi_2O_3 added evaporated during sintering.

4 wt% of acryloid binder
10 wt% of acetone

For compositions x = 0.001 – 0.15, 3 mol % excess Bi_2O_3 added as sintering aid to achieve higher density for pellets for electrical measurement

Mix until dried

Grind and screen through 80 mesh

Dry press at 70 MPa

Binder burnout

325 °C for 90 min and 550 °C for 60 min

Binder burnout profile

Cold isostatic press at 200 MPa

Sinter

1100 ~ 1300 °C for 1 - 20 hours

Polish pellets

Sintering profile

Crush into powder and anneal for XRD measurement

Electrode with gold for electrical measurement

SEM/TEM microstructural analysis

Figure 3.3.   Flow chart for pellet preparation with the profiles for binder burnout and

sintering

46

3.1.3 Single Dielectric Layer Capacitor Preparation

Figure 3.4 is the flow chart for the tape casting process and the preparation of single dielectric layer capacitors for electrical testing. First, the calcined powder was mixed in a solution with 32 wt% methylethylketone (MEK, Alfa Aesar), 32 wt% ethyl alcohol (Pharmco - AAPER), and 1 wt% fish oil (Z-3 Blown Menhaden, Tape Casting Warehouse) as a dispersant. The solution was then ball milled with stabilized zirconia media (~ 9mm height and 9 mm diameter, TOSOH Ceramics) for 12 hours. The organics, including 10 wt% PVB binder (BMS FB – C96, Sekisui) and 4 wt% plasticizer (Butyl Benzyl Phthalate S-160, Tape Casting Warehouse) were added to the solution, and the slurry was ball milled for an additional 12 hours. Before tape casting, the slurry was slowly rotated for 6 hours to remove air.

Tape casting was performed on a sheet of Mylar using a commercial casting machine (A. J. Carstern Co., Inc.), with a casting speed of about 8 cm/s. The thickness of the tape was controlled by changing the space between the doctor blade and the casting stage. The resulting tape thickness ranged from about 25 μm to 50 μm. The tape was dried at least 1 hour after casting before the printing and stacking stages.

Platinum thick film ink (6482, Degussa) was screen printed on the tape in 5 mm x 5 mm squares to serve as inner electrodes. The tapes with the electrodes were stacked with a 1 mm off-set from each other so that the effective electrode area was 4 mm x 5 mm. More dielectric layers (~ 250 μm thick total) were laminated on the top and bottom of the active layer to form cover layers and to support the structure. The capacitor structure was then laminated in a uniaxial press for 10 minutes at 65 °C with

30MPa pressure for pre-lamination treatment, and the structure was finally laminated at 65 ^{o}C for 10 minutes with 200MPa pressure.

Binder burnout was performed with the profile shown in the flow chart (including 30 minutes holds at 200 ^{o}C, 300 ^{o}C, 400 ^{o}C, and 500 ^{o}C as well as a hold at 550 ^{o}C for 60 minutes, and with the heating rate of 0.5 ^{o}C/min between each setting temperature). Since the tape contained more binder than the pellets, this slower binder burnout was essential to remove the organic from the green ceramics before sintering.

Sintering was performed using the same conditions as was used for pellets, e.g. 1250 ^{o}C for 60 minutes for 0.7 $BaTiO_3$ − 0.3 $BiScO_3$ ceramics, with a source powder of the same composition.

The sintered sample was then polished so that the inner electrode could be exposed and terminated. Silver post-fire ink (Dupont 6160) was painted on both sides of the samples as termination electrodes, and the samples were fired at 850 ^{o}C for 12 minutes.
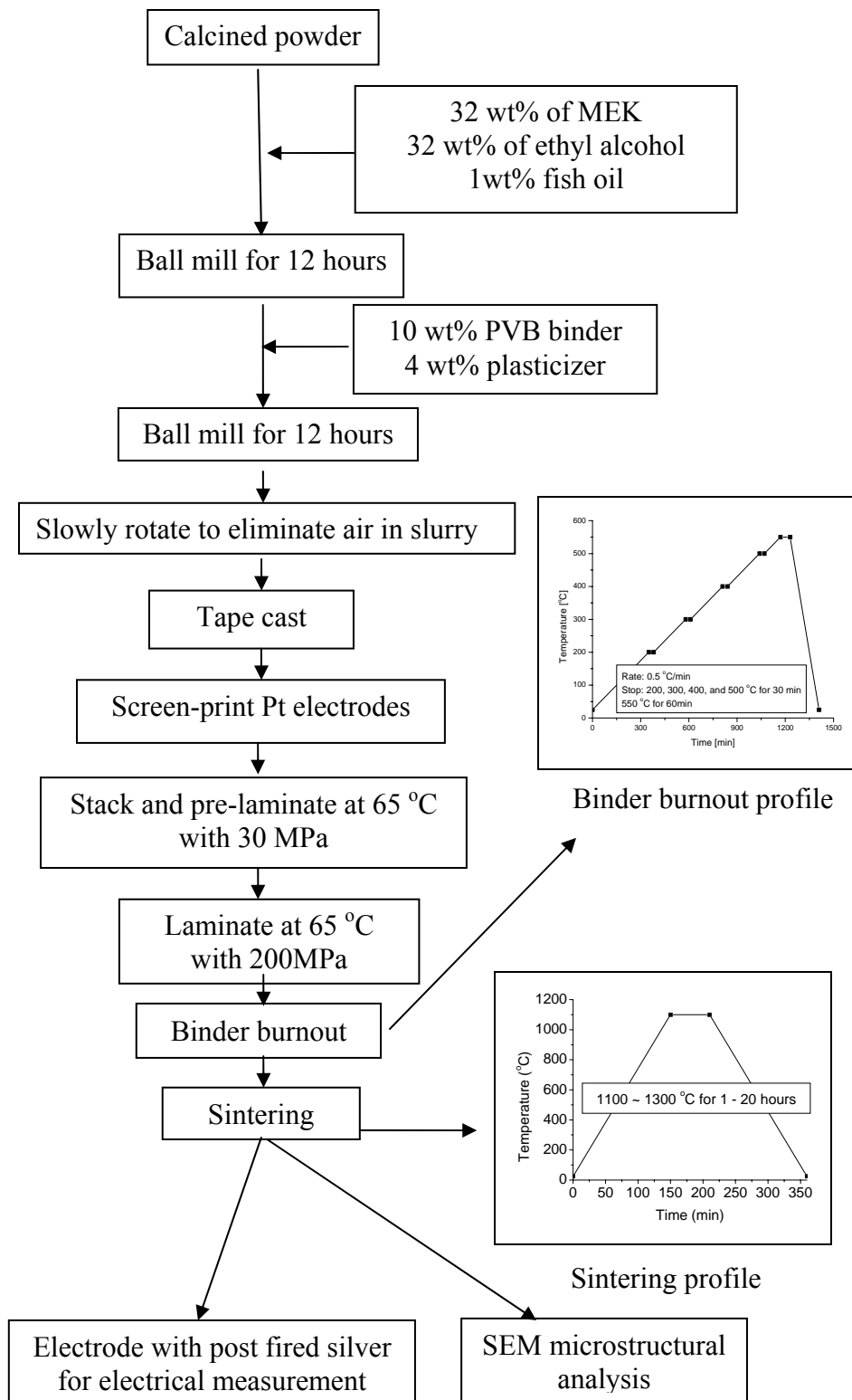
Figure 3.4. Flow chart for thin dielectric layer capacitor preparation with the profiles

for binder burnout and sintering

3.2 Structural Characterization

X-ray diffraction (XRD) was performed at room temperature for structural analysis and lattice parameter determination using a Scintag PADV diffractometer with Cu Kα radiation (35 kV, 30 mA, 0.02 $^{\circ}$/step, 3 sec/step conditions were used for lattice parameter calculation and 0.6 sec/step for the phase determination). Sintered pellets were crushed and ground into powder, followed by annealing at 300 $^{\circ}$C to reduce the stress from the grinding. A silicon internal standard with a certified lattice constant of 5.4301 +/- 0.0001 Å (Gem Dugout) was employed for precise lattice parameter determinations. XRD patterns were calibrated with the internal standard, and peaks were obtained using Jade software (Materials Data Inc.). Lattice parameters were calculated from the peaks using a least squares minimization of errors.

Microstructural analysis was performed on some of the sintered samples with a scanning electron microscope (SEM, Hitachi S-3000, secondary electron imaging at an operating voltage of 20kV) and a transmission electron microscope (TEM, Philips 420, bright field imaging at an operating voltage of 120kV). Samples for SEM were either fractured or polished with progressively finer media down to 3 μm Al_2O_3 powder and then thermally etched for 12 min at 100 $^{\circ}$C lower than the sintering temperature for the polished samples. Samples for TEM were mechanically polished down to about 30 μm, and then ion milled (Fischione Instruments model 1010 or Gatan model 691) to make the samples electron transparent. A Philips 420 TEM with an energy dispersive spectrometer (EDS, e2v scientific instruments) was employed to assess the grain size and to analyze the compositional gradient within samples.

3.3 Electrical characterization

For electrical measurements on pellet samples, the sintered pellets were polished to achieve parallel, smooth faces, and gold electrodes were sputtered on both faces of the pellets. Dielectric measurements were performed from -120 to 400 $^{\circ}$C in custom-designed furnaces with a LF impedance analyzer (HP4192A) with computerized control and data collection systems using a heating or cooling rate of 0.5 to 2 $^{\circ}$C/min. The frequencies employed for the measurement were from 100 Hz to 1MHz, with an oscillating voltage of 1.0 V. To minimize the effect of moisture on capacitance measurements, data obtained from a cooling cycle was used for measurements $< \sim 100$ $^{\circ}$C.

A modified Sawyer-Tower circuit was employed for ferroelectric switching measurements in custom-designed furnaces covering the temperature range from – 180 to 400 $^{\circ}$C. The stored electrical energy density of the samples was calculated using the decreasing field part of the hysteresis loop, as shown in Figure 3.5.
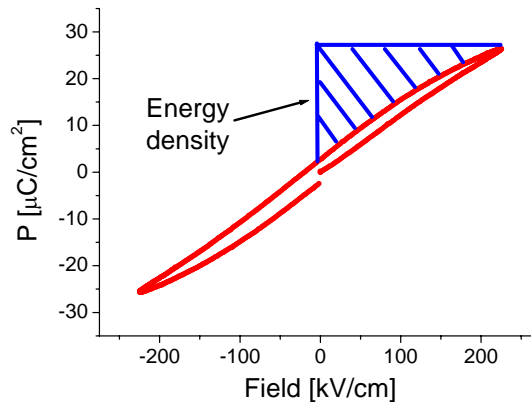
Figure 3.5. Example polarization vs. electric field data, showing the calculated energy density (shaded area)

To determine the dielectric breakdown strength, a D.C. field load was applied to the samples at a rate of 500 V/sec using a high voltage power source (Model 30/20, TRek). The point where a spike in current was observed was used as the dielectric breakdown strength.

Chapter 4:   Result and Discussion

4.1   BaTiO$_3$ - BiScO$_3$ Ceramics

4.1.1   Compositions

For the base (1-x) BaTiO$_3$ - x BiScO$_3$ system, compositions with x = 0 to 0.5 were prepared.   This composition range was chosen based on the fact that in thin films, phase-pure perovskite samples could be achieved up to x = 0.45 even without epitaxy. Optimized dielectric properties were found at about x = 0.4 (Tinberg and Trolier-McKinstry, 2007).

4.1.2   Structural Characterization

Figure 4.1 shows the XRD data for samples with x = 0 – 0.5 after sintering.   It can be seen that all of the compositions with x = 0 – 0.3 could be prepared in the desired pure perovskite phase.   Small second phase peaks were observed for the x = 0.4 sample; the intensity of the second phase peaks increased for x = 0.5.   The second phases matched the powder diffraction peaks for Bi$_{20}$TiO$_{32}$ and Bi$_2$O$_3$ (ICDD PDF #00-042-0202 and #00-027-0050, respectively).   The solubility limit for BiScO$_3$ in BaTiO$_3$ is much larger than Bi doped BaTiO$_3$, where the limit has variously been reported to range from x = 0.05 to 0.10 for Ba$_{1-3/2x}$Bi$_x$TiO$_3$ (Zhou et al., 1999; Bahri et al., 2001).   This can be explained by the fact that the simultaneous addition of Sc with Bi should maintain charge balance; in the BaTiO$_3$ - BiScO$_3$ system, the following substitution is expected,

$$BiScO_3 \xrightarrow{\text{In BaTiO}_3 \text{ matrix}} Bi_{Ba}^{\bullet} \;+\; 3\,O_O^{X} \;+\; Sc_{Ti}^{'} \qquad (4.1)$$
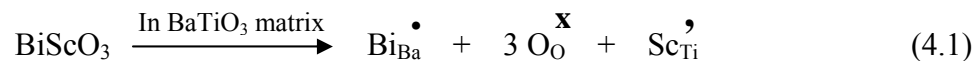
On the other hand, in Bi doped BaTiO$_3$, the anticipated but unproven solution with ionic compensated defects could be,

$$Bi_2O_3 \xrightarrow{\text{In BaTiO}_3 \text{ matrix}} 2\ Bi_{Ba}^{\bullet} + 3\ O_O^{x} + 2\ V_{Ti}^{''''} + 3\ V_O^{\bullet\bullet} \quad (4.2)$$
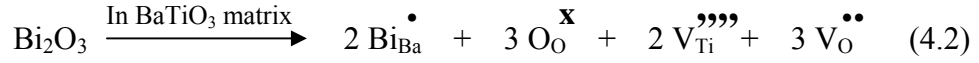
It is likely that the high vacancy concentration in Bi doped BaTiO$_3$ decreases the structural stability for high doping levels.
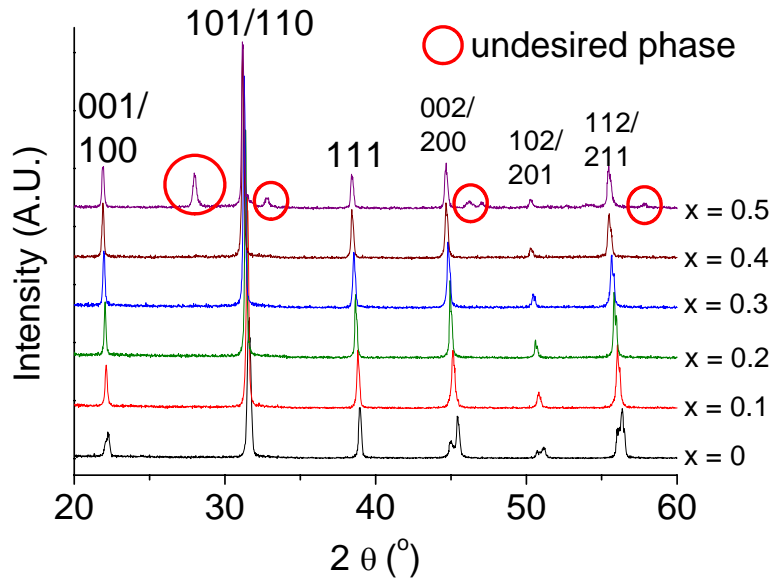
Figure 4.1.   X-ray diffraction pattern on (1-x) BaTiO$_3$ - x BiScO$_3$ ceramics.   The indexing is based on either tetragonal or pseudocubic perovskite unit cells.

Figure 4.2 shows the 220 and 202 peaks for samples with x = 0, 0.02 0.05, 0.075, and 0.10.   It appears that the perovskite structure is tetragonally distorted up to x = 0.05 and switches to a pseudocubic phase with x = 0.075 – 0.1.   Clear splitting of the {hhh} family of peaks, which is characteristic of rhombohedral structures, was not observed for any of the samples.
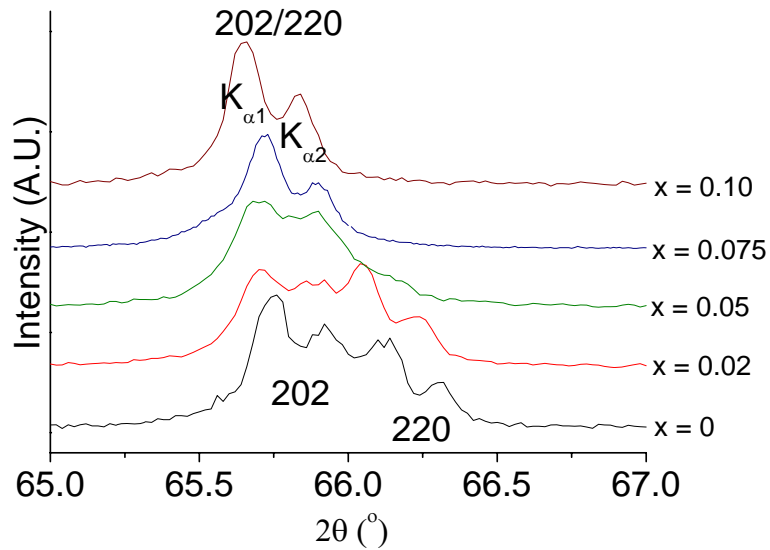
Figure 4.2.   X-ray diffraction pattern for (1-x) BaTiO$_3$ - x BiScO$_3$ after sintering, showing the transition from a tetragonal to a pseudocubic perovskite unit cell

The lattice parameters calculated from the XRD data assuming a tetragonal phase (x = 0 – 0.05) or a pseudocubic phase (x = 0.075 – 0.40) are plotted in Figure 4.3. The lattice parameters were determined using a least squares fit to at least six and four indexed diffraction peaks for tetragonal and cubic cells, respectively.   The linear increase in the lattice parameter with BiScO$_3$ concentration in the pseudocubic phase up to x = 0.4 is consistent with Vegard's law (Vegard, 1921), confirming solid solution. The result indicates that the solubility limit of BiScO$_3$ into BaTiO$_3$ is about x = 0.43, based on the deviation from Vegrad's law for the sample with x = 0.5.   This limit agrees well with the data on thin films, which reported that a pure perovskite phase was achieved with x = 0.2-0.45 without epitaxy (Tinberg and Trolier-McKinstry, 2007).   The observed decrease in tetragonality with BiScO$_3$ concentration is consistent with the

decreasing tolerance factor, t (t = 1.062 and 0.907 for pure $BaTiO_3$ and $BiScO_3$, respectively). A relation between tolerance factor and crystal structure has been well established in perovskites, and a lower tolerance factor generally favors rhombohedral, orthorhombic, or monoclinic phases (Eitel et al., 2001; Sasaki et al., 1983). However, the composition for the transition disagrees with the data on films, which showed clear tetragonality even with x = 0.20 and 0.30 (Tinberg and Trolier-McKinstry, 2007). It should be noted that the film data shows the symmetry change near a tolerance factor of 1, while the ceramics investigated here become pseudocubic at a tolerance factor of about 1.05, an unusually high value. The origin of this discrepancy is not known, but may be a function of strains associated with the film deposition, or may reflect differences between powders and continuous samples (Woodward et al., 2003).
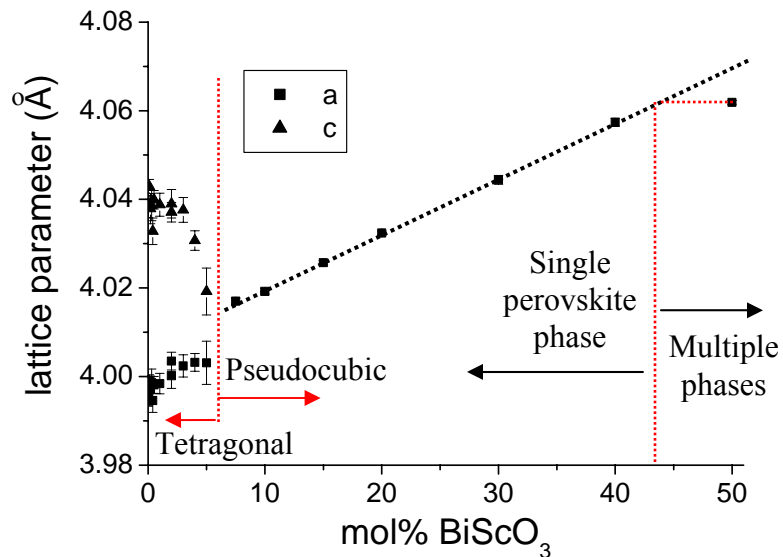
Figure 4.3.   Lattice parameters as a function of $BiScO_3$ concentration (measured on powdered samples after sintering)

Figure 4.4 shows a comparison of the XRD data of samples with x = 0.001 with and without excess Bi added as a sintering aid. XRD data on the sintered samples with extra Bi_2O_3 showed less well-defined tetragonality than the ones without extra Bi_2O_3. Apparently, the defects associated with the excess Bi_2O_3 may contribute to a decreased tetragonality of the perovskite. This suggests that some amount of the Bi_2O_3 added as a sintering aid diffused into the structure during sintering. The impact of this fact needs to be considered carefully in the dielectric property analysis.
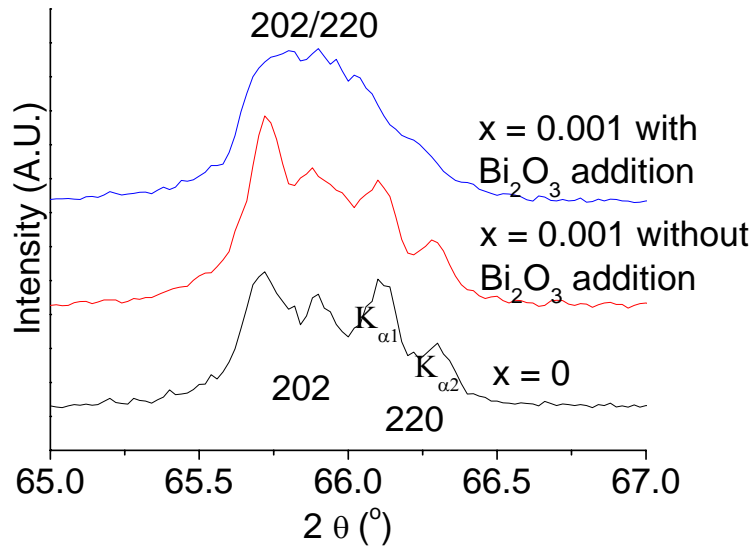
Figure 4.4. X-ray diffraction patterns of (1-x) $BaTiO_3$ - x $BiScO_3$ after sintering, showing the effect of excess Bi_2O_3 used in the sintering on the structure

4.1.3 Microstructure

The sintered pellets prepared as described in section 3.1 were confirmed to possess more than 95 % of theoretical density for all samples.   Theoretical density was calculated based on the lattice parameters obtained from the XRD study in the previous section.   Figure 4.5 is a SEM micrograph on the fractured surface of the sample sintered at 1300 ^{o}C for 1 hour with composition x = 0.1, showing an almost pore-free, fine microstructure as expected.
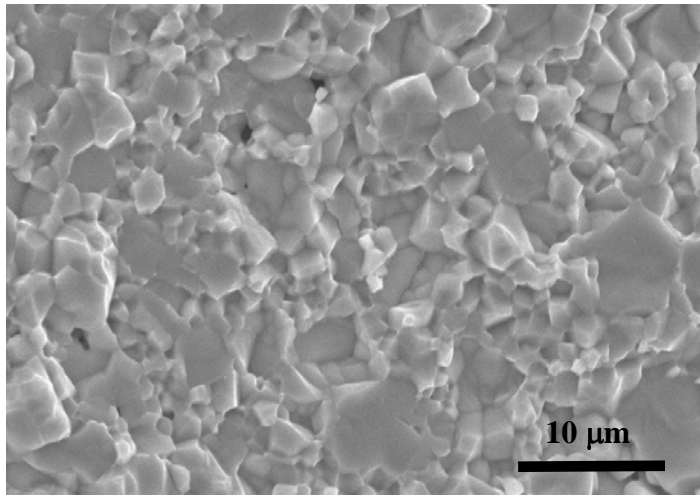
Figure 4.5.   SEM micrograph on the fractured surface of sintered 0.9 BaTiO$_3$ - 0.1

BiScO$_3$ ceramic sintered at 1300 ^{o}C for 1 hour

An interesting feature in microstructure was observed for x = 0.03 – 0.1.   The samples with the compositions were hard to homogenize during sintering, resulting in core-shell structures observed with TEM, as shown in Figure 4.6 for x = 0.05 with 1 hour and 20 hour sintering.   It was found the prolonged sintering reduced the number of core-shell grains and the size of cores.   However, the inhomogeneity could not be

completely eliminated even with 20 hour sintering, as shown in Figure 4.6(b). It was roughly estimated that more than a half of the grains exhibited core-shell features in 1 hour sintered samples, whereas less than 10% of the grains did in 20 hour sintered samples. The consequence of this core-shell structure on dielectric properties is discussed in the following section. EDS results indicated that shell was enriched in $BiScO_3$, while the cores were depleted, as shown in Figure 4.7.

(a)   (b)
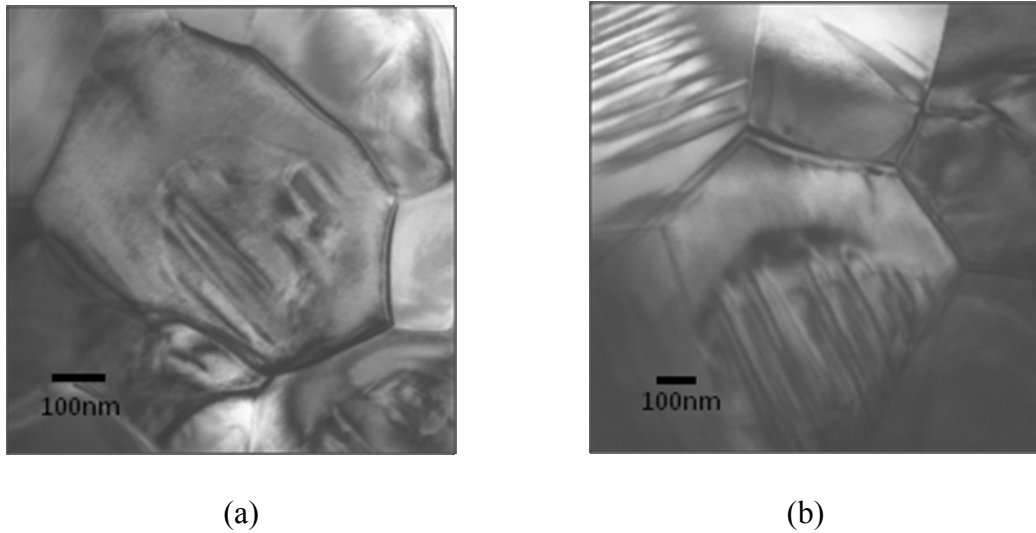
Figure 4.6. TEM micrograph of 0.95 $BaTiO_3$ – 0.05 $BiScO_3$ ceramics (a) 1 hour sintering and (b) 20 hour sintering
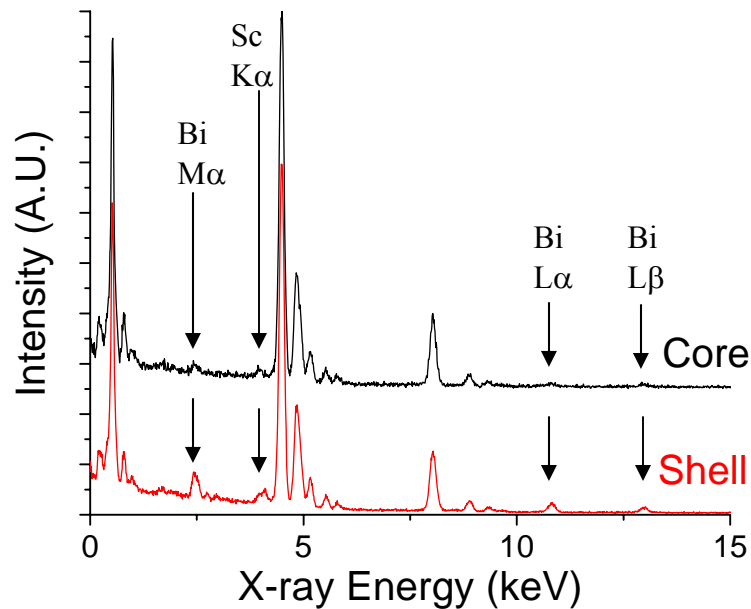
Figure 4.7.   EDS spectrum of 0.95 BaTiO$_3$ – 0.05 BiScO$_3$ ceramics with 1 hour sintering,

showing a significant difference in Bi and Sc intensity between the core and the shell

The process employed in this work also resulted in fine-grained material, especially near the BaTiO$_3$ end of the solid solution.   Figure 4.8 shows TEM micrographs of sintered samples for the compositions x = 0, 0.02, 0.05, 0.1, and 0.2, with 1 hour sintering.   Pure BaTiO$_3$ had grains larger than 5 μm, as shown in Figure 4.8(a), but the composition with a few % BiScO$_3$ showed about a 0.3 μm grain size (Figure 4.8(b)).   The grain size increased slowly with further increase in the BiScO$_3$ concentration; an average grain size of 2 μm was observed for 20% BiScO$_3$ (Figure 4.8(e)).   This result is counterintuitive since extra Bi$_2$O$_3$, which would presumably act as a sintering aid, was added to the samples with x = 0.001 – 0.15.   The mechanism which is responsible for this observation should be studied in future work.
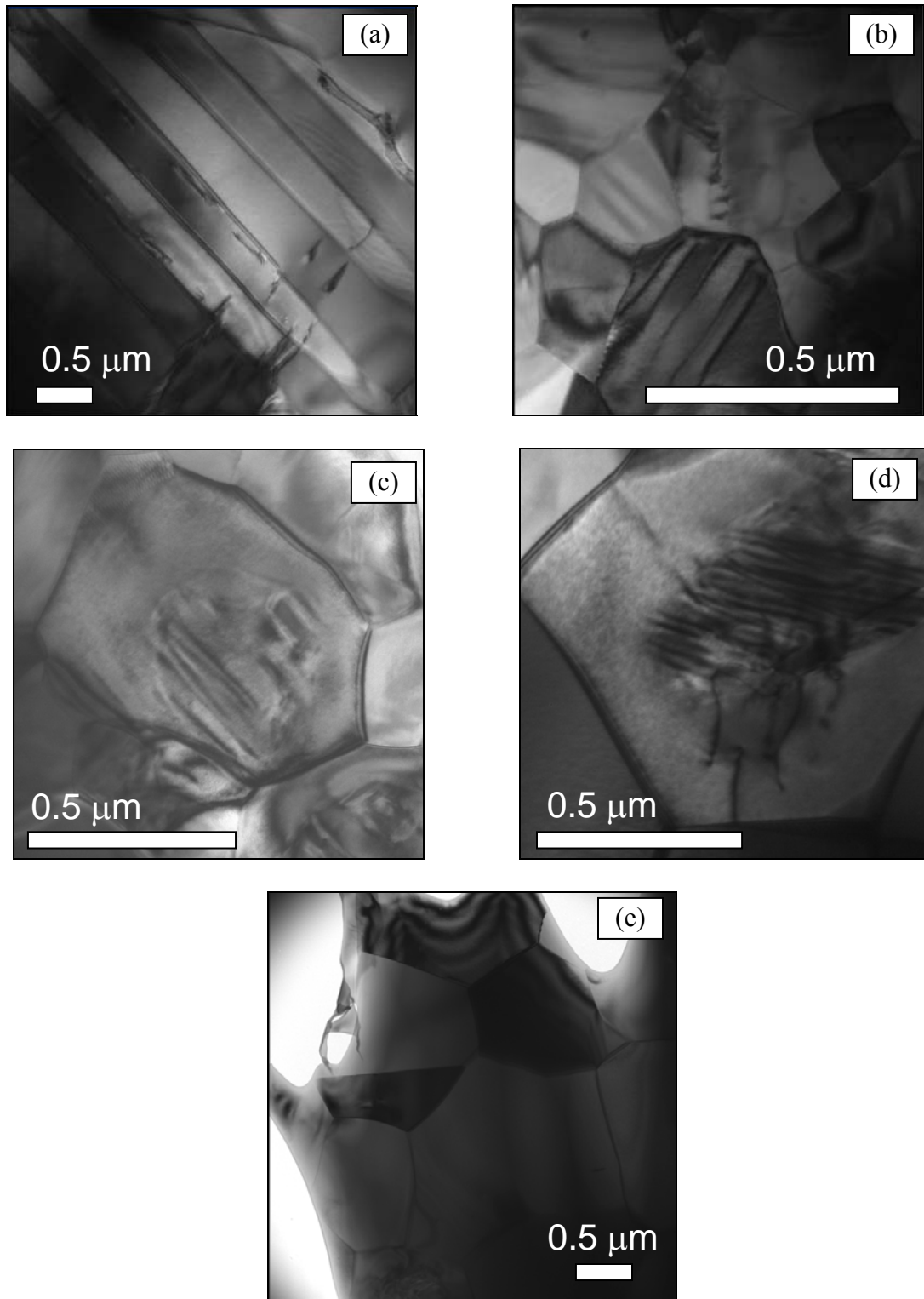
Figure 4.8.   TEM micrographs of (1-x) $BaTiO_3$ - x $BiScO_3$ ceramics for x = (a) 0, (b) 0.02, (c) 0.05, (d) 0.1, and (e) 0.2

4.1.4. Dielectric Properties

Figure 4.9 shows the dielectric constant and loss tangent data of ceramics with x

= 0, 0.005, 0.02, 0.05, 0.2, and 0.4 measured at frequencies from 100 Hz – 1 MHz over

the temperature range from -120 to 400 ^{o}C.

(a)

(b)

(c)
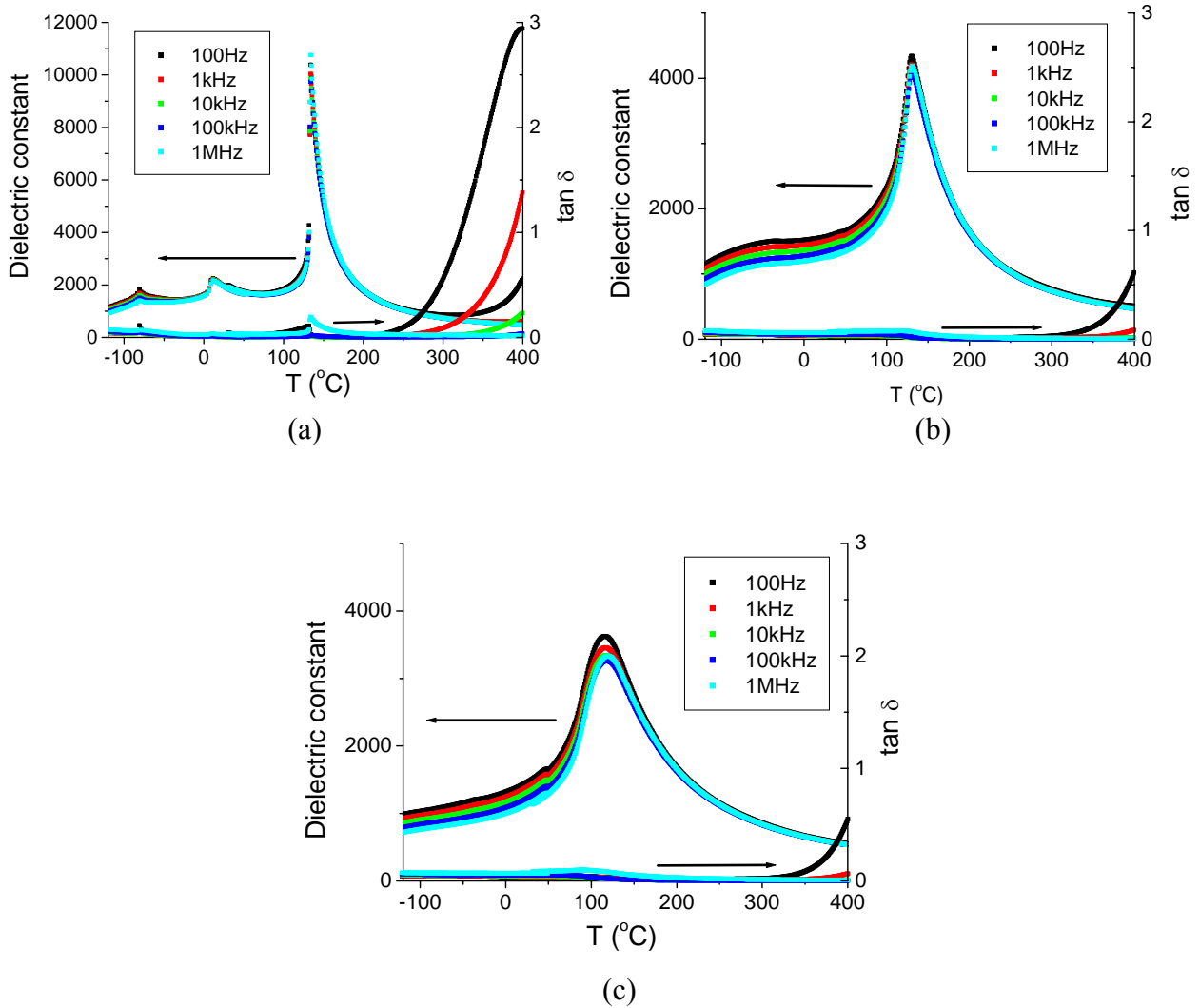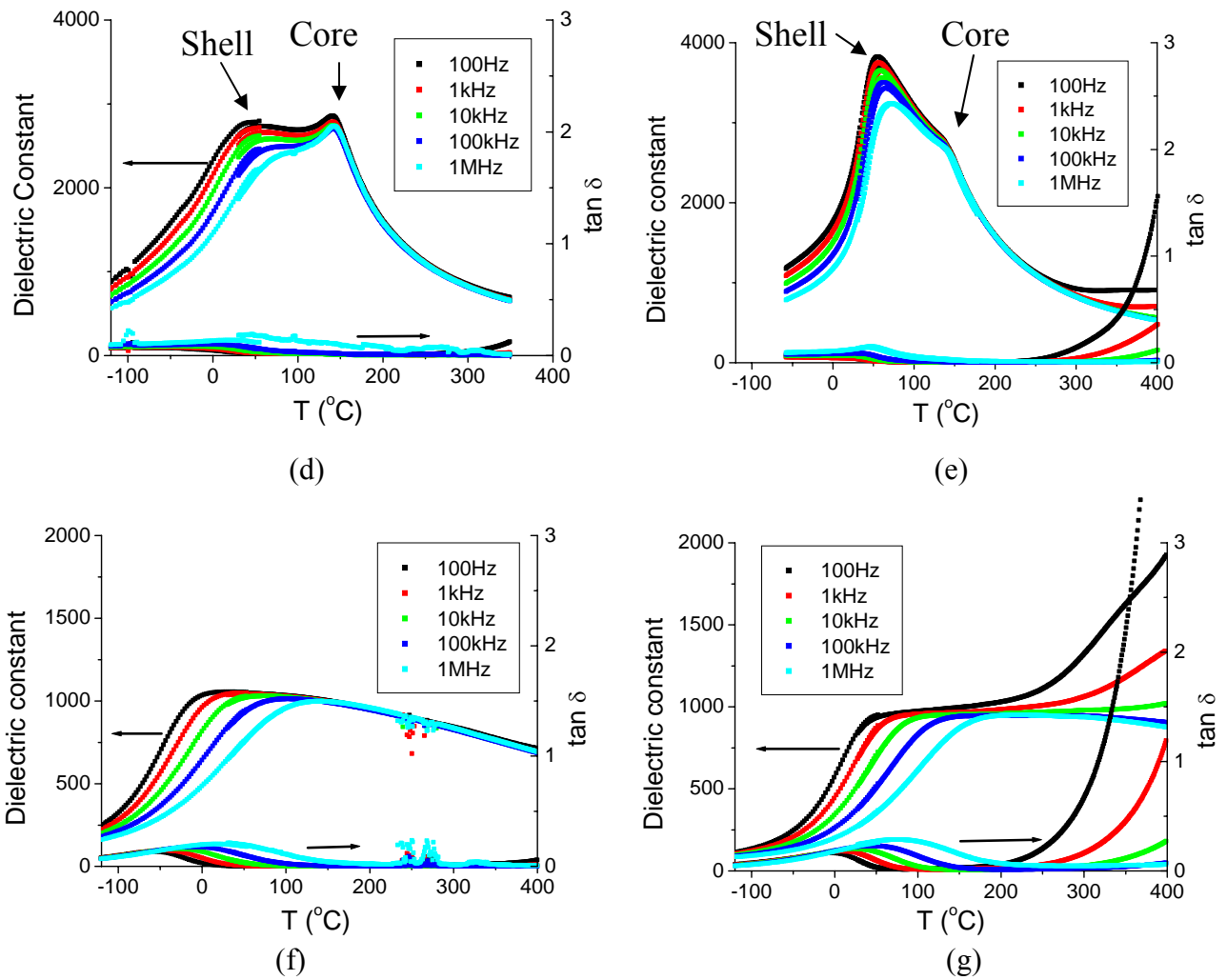
Figure 4.9.   Dielectric constant and dielectric loss tangent data as a function of

temperature measured at frequencies of 100Hz – 1MHz for (1-x) BaTiO$_3$ - x BiScO$_3$

ceramics (a) x = 0, (b) 0.005, (c) 0.02, (d) 0.05, (e) 0.05 with 20 hour sintering (f) 0.2,

and (g) 0.4.   Note that all samples except for (e) were sintered for 1 hour.

It is clear that as $BiScO_3$ is added to $BaTiO_3$, the materials quickly lose two of the characteristic sharp dielectric peaks and the maximum dielectric constant decreases significantly. That is, even for a small amount of $BiScO_3$, i.e. x = 0.005, the peaks associated with the rhombohedral to orthorhombic and orthorhombic to tetragonal phase transitions are difficult to distinguish.

Samples with core-shell microstructures, mentioned in section 4.1.3, had two permittivity peaks at about 50 and 140 $^{\circ}$C over the measured temperature range, as shown in Figure 4.9(d) for x = 0.05. With longer sintering, the lower temperature dielectric peak grows and the high temperature peak becomes a shoulder, as shown in Figure 4.9(e). This is consistent with the observation that samples sintered for 20 hours became more compositionally homogeneous. This also suggests that the cores of the grains observed in the TEM micrographs are rich in $BaTiO_3$. These would then be responsible for the higher temperature peak. In contrast, the shell (rich in $BiScO_3$ or the Bi_2O_3 added as a sintering aid) would then account for the lower temperature peak. The EDS results, which indicated $BiScO_3$ - rich shells, support this assumption.

For x = 0.15 or more, a single diffuse dielectric peak with a dielectric constant of about 800-1000 over a wide range of temperature was observed. These data are very similar to those shown in thin films by Tinberg and Trolier-McKinstry (2007). Thus, the highly dispersive and diffusive dielectric behavior observed in thin films was confirmed in bulk materials as well. However, there is no strong increase in the room temperature permittivity suggestive of a MPB near the transition from tetragonal to pseudocubic structures. This contrasts with the observed increase in permittivity in thin

films at x = 0.4, which was considered to be the MPB (Tinberg and Trolier-McKinstry, 2007).   The origin of this discrepancy is not known.

The temperature of the maximum dielectric constant (T_{max}) was determined to be a function of composition, as shown in Figure 4.10(a) for the $BaTiO_3 - BiScO_3$ system. Figure 4.10(b) illustrates comparable data for the Bi doped $BaTiO_3$ system (Bahri et al., 2001).   In $BaTiO_3 - BiScO_3$ ceramics, for x = 0.03 – 0.1, the dielectric data from the samples sintered for 20 hours are used for T_{max} as they are assumed to be closer to their equilibrium state than the ones with shorter sintering periods.   It was found that T_{max} decreases monotonically with $BiScO_3$ concentration for x = 0 - 0.1.   From x = 0.1, T_{max} increases roughly linearly.

It is important to note that there may be two effects convoluted for the low $BiScO_3$ concentrations.   As was described in sections 3.1 and 4.1.2, in order to densify these samples, excess Bi had to be added, and some of this excess Bi was incorporated into the $BaTiO_3$.   It has previously been demonstrated that Bi doping of $BaTiO_3$ induces a slight decrease in T_c, as shown in Figure 4.10(b) (Bahri et al., 2001).   However, it is believed that the $BiScO_3$ concentration (rather than the Bi concentration) dominates the drop in T_{max} from x = 0 to 0.02, since the drop in T_{max} observed here is larger than the changes reported for Bi-doped $BaTiO_3$ with a few % of Bi.

(a)

(b)
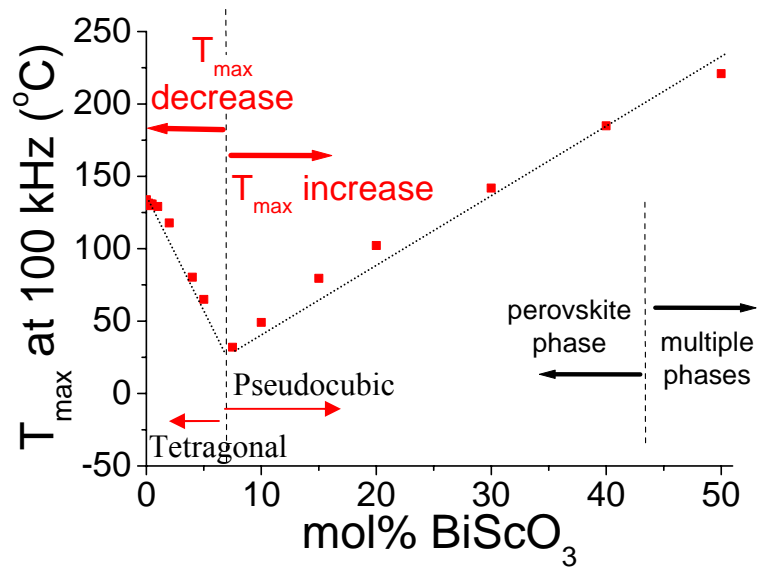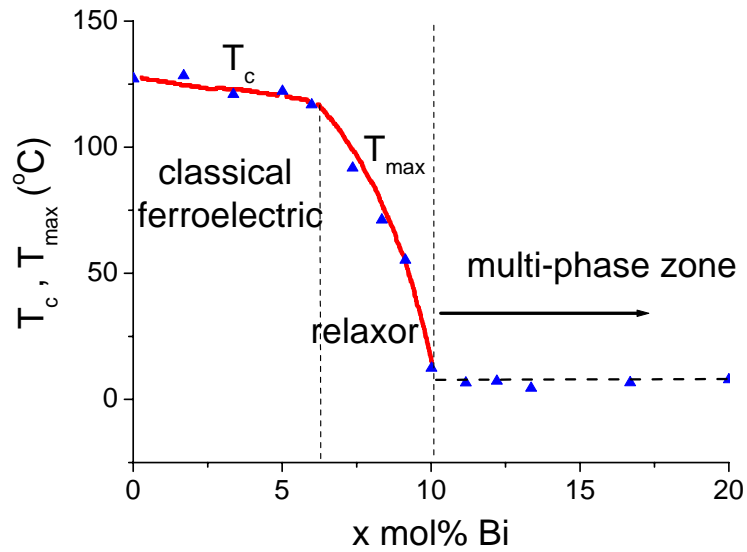
Figure 4.10. (a) T_{max} for 100 kHz as a function of composition for (1-x) $BaTiO_3$ - x $BiScO_3$ ceramics, and (b) T_{max} or T_c variation with x for $Ba_{1-3/2x}Bi_xTiO_3$ ceramics (rescaled after Bahri et al., 2001)

4.1.5 Dielectric Relaxation

Materials exhibiting dielectric relaxations possess intermediate to high permittivity values ranging from 50 to 40,000. The higher permittivity materials are typically relaxor ferroelectrics such as $Pb(Mg_{1/3}Nb_{2/3})O_3$, which involve complex interactions between interacting dipolar nano-domains. Low permittivity ($\varepsilon_r \sim 50\text{-}150$) materials with dielectric relaxations can involve dipoles that do not correlate over significant distances, such as is the case of $Bi_{1.5}(Zn_{0.92}Nb_{1.5})O_{6.92}$ (Nino et al., 2002).

It is interesting to consider for what compositions in $(1\text{-}x)$ $BaTiO_3$ - x $BiScO_3$ behave as a normal ferroelectric, a relaxor ferroelectric, or a dielectric relaxor. As shown in Figure 4.9, the dielectric behavior gradually becomes frequency dependent around $x = 0.02$ - 0.05, and strongly dispersive peaks are observed with increasing concentration of $BiScO_3$. Figure 4.11 plots the inverse of the dielectric constant at 1 MHz as a function of temperature for ceramics with $x =$ (a) 0, (b) 0.05, (c) 0.1, and (d) 0.2. The fit to the Curie-Weiss law (Jona and Shirane, 1993) and the calculated Curie constant are also shown in the figure. 1 MHz data was employed here to minimize the space charge contribution to the dielectric constant. Higher temperature measurements ($> 400\,^{o}C$) were attempted to acquire better fits to Curie-Weiss law, but could not be used because of increases in the loss tangent around $400\,^{o}C$ even at 1 MHz. It is clear that the Curie-Weiss law is obeyed reasonably well up to $x = 0.05$, but a deviation from the linear relation can be observed for $x = 0.1$ and 0.2. The Curie constant increases with the $BiScO_3$ concentration, but it is unclear if this is an intrinsic trend of the system due to the small temperature range for the fits caused by the space charge contribution at high temperature. It was difficult to determine a deviation temperature, T_D from these results.
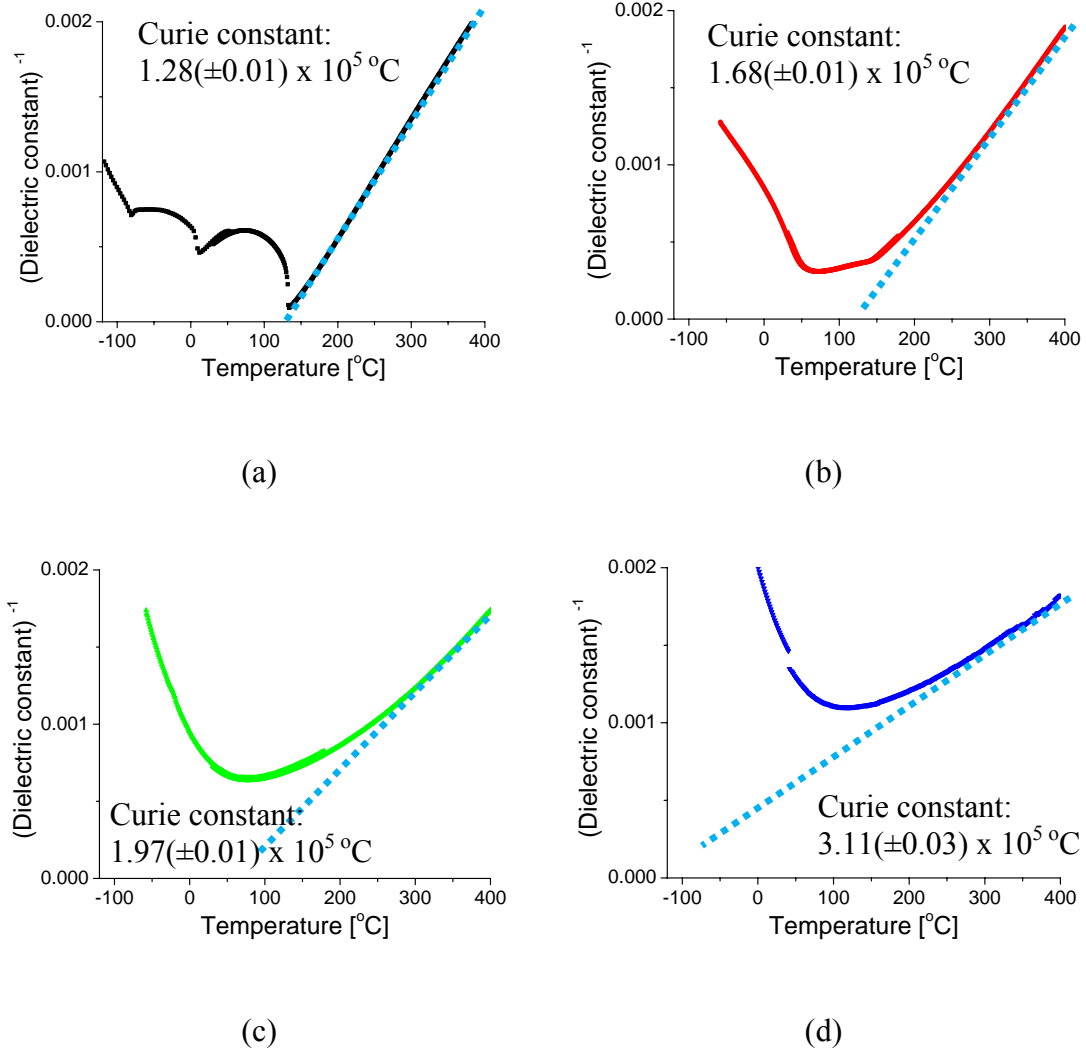
Figure 4.11. Curie-Weiss plot for (1-x) BaTiO$_3$ - x BiScO$_3$ samples with x = (a) 0, (b) 0.05, (c) 0.1, and (d) 0.2 at 1 MHz with the fit to Curie-Weiss law and Curie constant

Since both dielectric dispersion and deviation from the Curie-Weiss law are characteristic of relaxor ferroelectric materials, this result suggests that the solid solution behaves like a normal ferroelectric with the range from x = 0 to about x = 0.02 and shows more relaxor-like behavior with a further increase of BiScO$_3$. The trend agrees with the

increasing dispersion observed in thin films with increasing $BiScO_3$ concentration (Tinberg and Trolier-McKinstry, 2007).

Both Arrhenius and Vogel-Fulcher (Vogel, 1921; Fulcher, 1925) fits to the frequency dispersion were considered for compositions $x = 0.1 - 0.5$. The maxima in the measured loss tangent were fit to an asymmetric sigmoidal function to obtain T_{max}, as shown in Figure 4.12 for $x = 0.3$, since it was difficult to determine T_{max} values from the dielectric constant. The Arrhenius model assumes that a thermally activated process governs the dielectric relaxation. This yields a temperature dependent relaxation expressed by:

$$\omega = \omega_0 \exp [- E_a / k_B T_{max}] \qquad\qquad (4.3)$$

where ω is the measured frequency of the loss tangent maximum, ω_0 is related to the attempt jump frequency, E_a is the activation energy , and k_B is Boltzmann's constant.
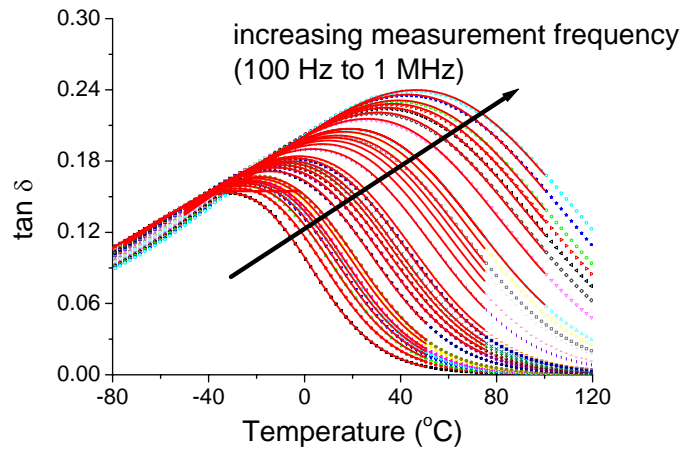
Figure 4.12. tan δ vs. temperature for frequencies from 100 Hz to 1MHz measured on a 0.7 $BaTiO_3$ - 0.3 $BiScO_3$ sample. The symbols are the experimental data; the solid lines are fits using an asymmetric sigmoidal function to obtain T_{max}.

Figure 4.13 shows Arrhenius plot for x = 0.3. The data fit the Arrhenius expression reasonably well over the measured frequency range, although some deviations are apparent ($R^2 \sim 0.995$). However, the attempt jump frequencies obtained for compositions from 0.1 – 0.5 are unrealistic (on the order of 10^{18} to 10^{20} Hz), well beyond the electronic resonant frequency. Unphysical values of this type are common in relaxor ferroelectrics (Colla et al., 1992).
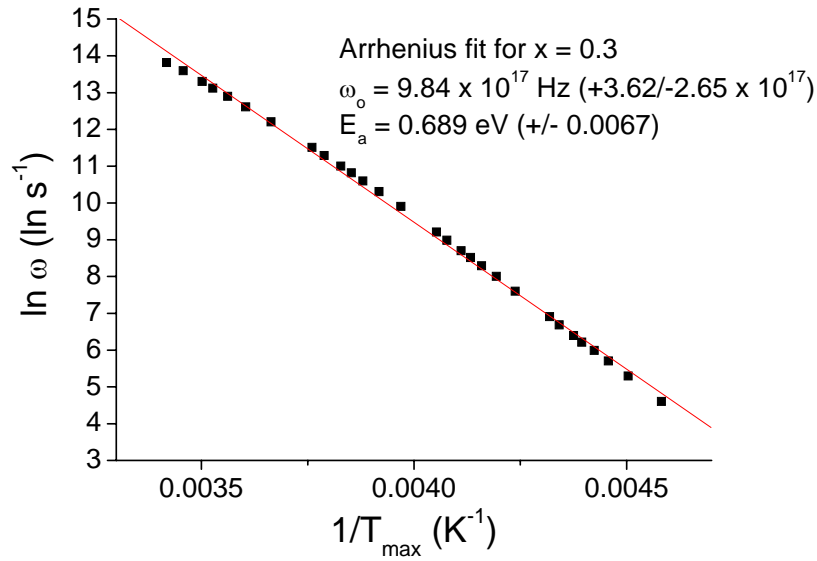
Figure 4.13. The frequency of the loss tangent maximum as a function of inverse T_{max} for a 0.7 $BaTiO_3$ - 0.3 $BiScO_3$ sample. The solid line is fitted to an Arrhenius model.

The unphysical results are a consequence of the assumption implicit in the Arrhenius plot that the dipoles become dynamic for all temperatures above absolute zero temperature (0 K). If instead, it is assumed that the dynamics are initiated above a freezing temperature, T_f, this gives a dielectric analog of a spin or a dipolar glass and the

dielectric relaxation should follow a Vogel-Fulcher model (Viehland et al., 1990; Chen et al., 2000). This is expressed by the equation,

$$\omega = \omega_0 \exp\left[-E_a / k_B (T_{max} - T_f)\right] \qquad (4.4)$$

where T_f is the freezing temperature. T_f can be thought of as the temperature below which thermal energy is no longer sufficient to permit dipolar cluster dynamics in relaxor ferroelectrics.

Figure 4.14 shows the Vogel-Fulcher plot for compositions x = 0.1 – 0.5. All of the data show excellent fittings ($R^2 > 0.999$ for all compositions). Figure 4.15 plots the key parameters, namely, the activation energy, the attempt frequency, and freezing temperature values obtained from the Vogel-Fulcher fit as a function of $BiScO_3$ concentration. The error bars are plotted using the 95% confidence intervals obtained in the fitting. It is difficult to find a composition trend in either the activation energy or the attempt frequency, but it is clear that the freezing temperature increases as the $BiScO_3$ concentration increases. Thus, as shown in Figure 4.16, both T_f and T_{max} increases as a function of the $BiScO_3$ concentration in the pseudocubic structure range.

Table 4.1 lists the Vogel – Fulcher fitting parameters obtained in this study along with values for other perovskites and $BaTiO_3$ - $BiScO_3$ thin films. The attempt frequencies obtained for the $BaTiO_3$ - $BiScO_3$ system, $\omega_o \sim 10^{13}$ Hz, compare well with other relaxors. However, the calculated activation energies, $E_a \sim 0.25$ eV are unusually high. Moreover, the values determined here do not correspond to the values obtained in thin films with the same compositions, which are 0.05 – 0.12 eV (Tinberg, 2006). The origin of this discrepancy is not known. It should be noted though, that ω_o in films ($\sim 10^8$ Hz) is also anomalously low.

It was previously observed by Stringer et al. that $Pb(Mg_{1/3}Nb_{2/3})O_3 - PbTiO_3$ with $BiScO_3$ addition (BS-PMN-PT ternary system) shows only a small change in T_f, with increasing $BiScO_3$ concentration (0.22 to 0.32 BS) (Stringer et al., 2007). In that case, however, the PMN concentration was changed at the same time (from 0.25 to 0.15 PMN). Viehland (Viehland, 1992) demonstrated that T_f decreases with PMN concentration in PMN-PT (See PMN – PT data in Table 4.1). Thus, to account for the small change in T_f reported in the Stringer data (Stringer et al., 2007), $BiScO_3$ would have to increase T_f, which is consistent with the trend observed in $BiScO_3 - BaTiO_3$ system.
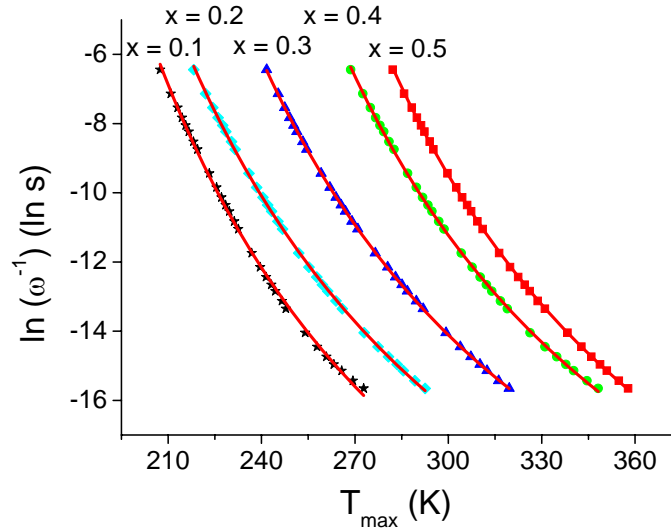
Figure 4.14. The inverse frequency of the loss tangent maximum as a function of T_{max} for (1-x) $BaTiO_3$ - x $BiScO_3$ samples with x = 0.1 – 0.5. Solid lines are fits to the Vogel-Fulcher model.
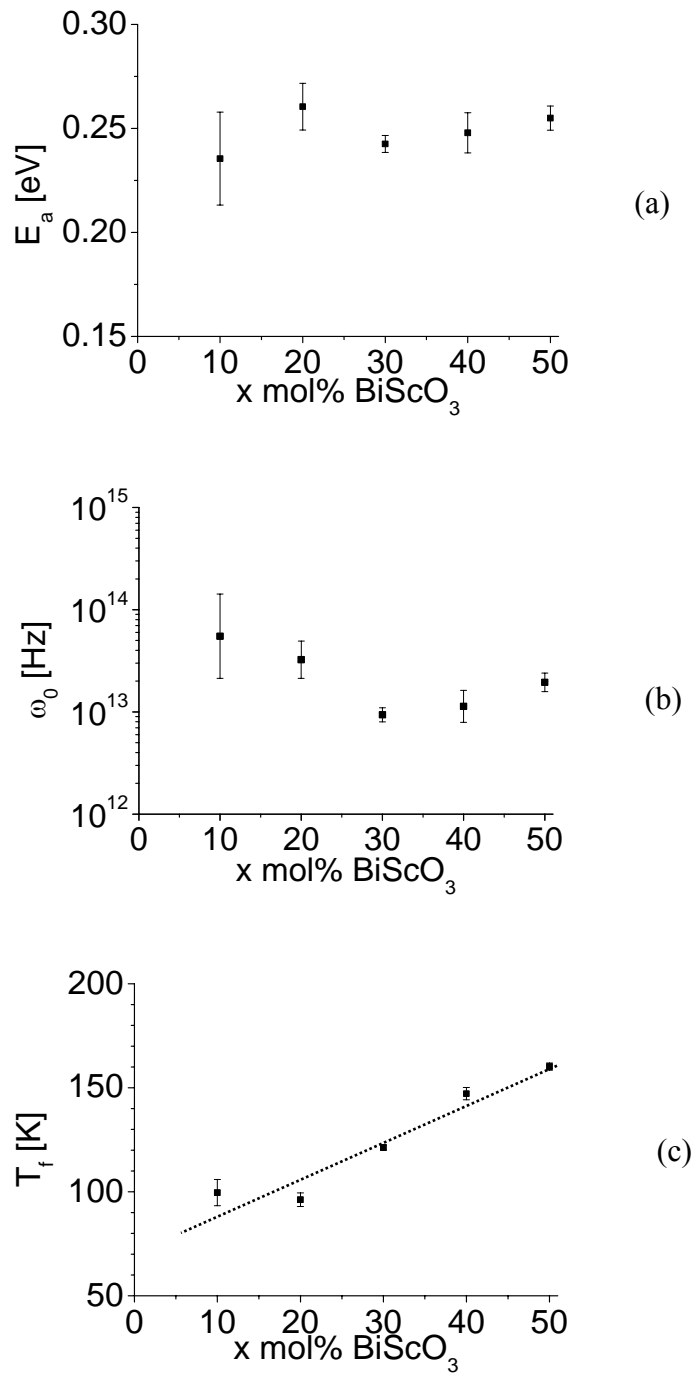
Figure 4.15.   (a) Activation energy, (b) attempt jump frequency, and (c) freezing

temperature obtained from the fit to the Vogel – Fulcher model for (1-x) BaTiO$_3$ - x

BiScO$_3$ ceramics
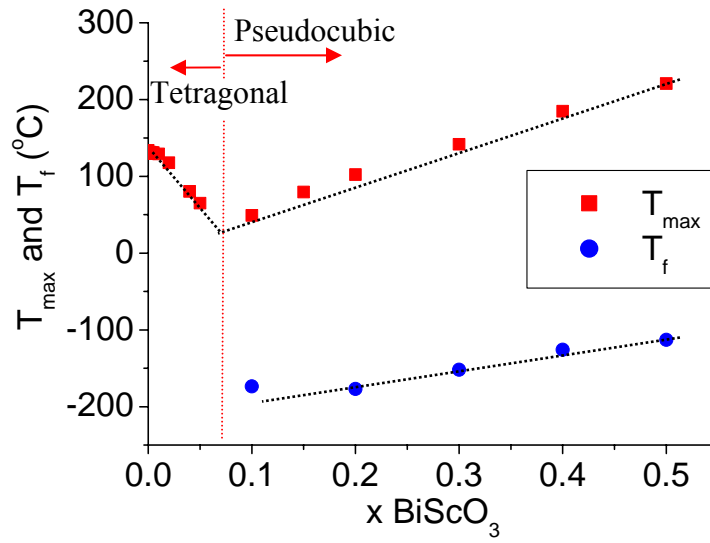
Figure 4.16. T_f and T_{max} as a function of $BiScO_3$ concentration for $(1-x)$ $BaTiO_3$ - x

$BiScO_3$ ceramics

Table 4.1. Activation energy, attempt jump frequency, and freezing temperature

obtained from the fit to the Vogel – Fulcher model for various perovskite materials

System	x	E_a (eV)	ω_o (Hz)	T_f (K)	Ref
(1-x) BaTiO$_3$ - x BiScO$_3$ (This study)	0.1	0.24 ± 0.02	5.5 x 10^{13}	100 ± 6	-
	0.2	0.26 ± 0.01	3.2 x 10^{13}	96 ± 3	
	0.3	0.24 ± 0.01	9.4 x 10^{12}	121 ± 1	
	0.4	0.25 ± 0.01	1.1 x 10^{13}	147 ± 3	
	0.5	0.26 ± 0.01	2.0 x 10^{13}	160 ± 2	
(1-x) PMN - x PT	0	0.076	1.0 x 10^{13}	220	Viehland, 1992
	0.07	0.061	3.7 x 10^{14}	284	
	0.1	0.046	2.4 x 10^{12}	296	
	0.2	0.019	4.1 x 10^{12}	350	
	0.25	0.017	3.4 x 10^{12}	384	
x BS - (1-x) (PMN - 0.53 PT) (1 mol % excess MgNb$_2$O$_6$)	0.22	0.104	1.3 x 10^{13}	430	Stringer et al., 2007
	0.32	0.111	1.3 x 10^{12}	432	
(Sr$_{1-1.5x}$Bi$_x$)TiO$_3$	0.0133	0.036	1.00 x 10^{10}	30.7	Chen and Yu, 2002
	0.0533	0.040	1.73 x 10^9	70.3	
	0.133	0.047	1.05 x 10^9	104.6	
	0.2	0.025	3.08 x 10^8	131.9	
Ba(Ti$_{0.7}$Zr$_{0.3}$)O$_3$	-	0.21	1.54 x 10^{10}	199.6	Yu et al., 2002
Ba(Ti$_{1-x}$Ce$_x$)O$_3$	0.06	0.0039	1.45 x 10^{11}	374.1	Chen et al., 2002
	0.1	0.0076	1.32 x 10^{11}	320.1	
	0.2	0.027	3.21 x 10^9	138.7	
(1-x) BaTiO$_3$ - x BiScO$_3$ (Thin film)	0.2	0.05	5.3 x 10^7	147	Tinberg, 2006
	0.4	0.06	2.6 x 10^8	175	
	0.6	0.12	3.4 x 10^9	147	

To access the high field dielectric response, the polarization was measured as a function of applied electric field, as shown in Figure 4.17. Compositions with $x \leq 0.05$ show a ferroelectric hysteresis loop, whereas compositions with $x \geq 0.1$ do not show sign of polarization saturation when measured with a maximum applied electric field of 50 kV/cm at room temperature (Figure 4.17(a)). Measurements at higher field were performed for a thinner sample with $x = 0.3$ at various temperatures with a maximum applied electric field of about 550 kV/cm. As shown in Figure 4.17(b), the polarizations start to saturate at high field. There is no clear indication for the existence of a ferroelectric hysteresis loop at 0 ^{o}C, but the loops open at lower temperatures, suggesting long range ferroelectricity and relaxor behavior. It should be noted, however, that there is also dielectric loss that contributes to the opening of the loops, which makes it difficult to accurately define the ferroelectricity in the system. It would be useful in the future to monitor the temperature dependence of a property that depends on the remanent polarization.

Figure 4.18 shows the temperature dependence of the remanent polarization and coercive field for the 0.7 $BaTiO_3$ - 0.3 $BiScO_3$ ceramics obtained from the hysteresis loop in Figure 4.17(b). The diffuse transition to $P_R = 0$ and $E_C = 0$ would be consistent with relaxor ferroelectricity. However, T_f obtained from Vogel-Fulcher analysis for this composition was -150 ^{o}C, which is about 100 ^{o}C lower than the T_f estimated from these remanent polarization or coercive field behaviors ($\sim$ -50 ^{o}C). The origin for the difference may be, in part, the very different field levels used to probe the sample in the two families of measurements. This should be investigated in a future study.

In thin films, a clearer ferroelectric hysteresis loop was obtained with x = 0.4 at lower temperatures, suggesting that these materials are really relaxor ferroelectrics (Tinberg and Trolier-McKinstry, 2007).   This difference may arise from the fact that much higher electric fields (on the order of MV/cm) can be applied to thin films due to their superior dielectric breakdown strength.   Thinner samples with higher densities need to be prepared so that higher electric fields can be applied to ceramics to confirm if this is the case.

(a)

(b)
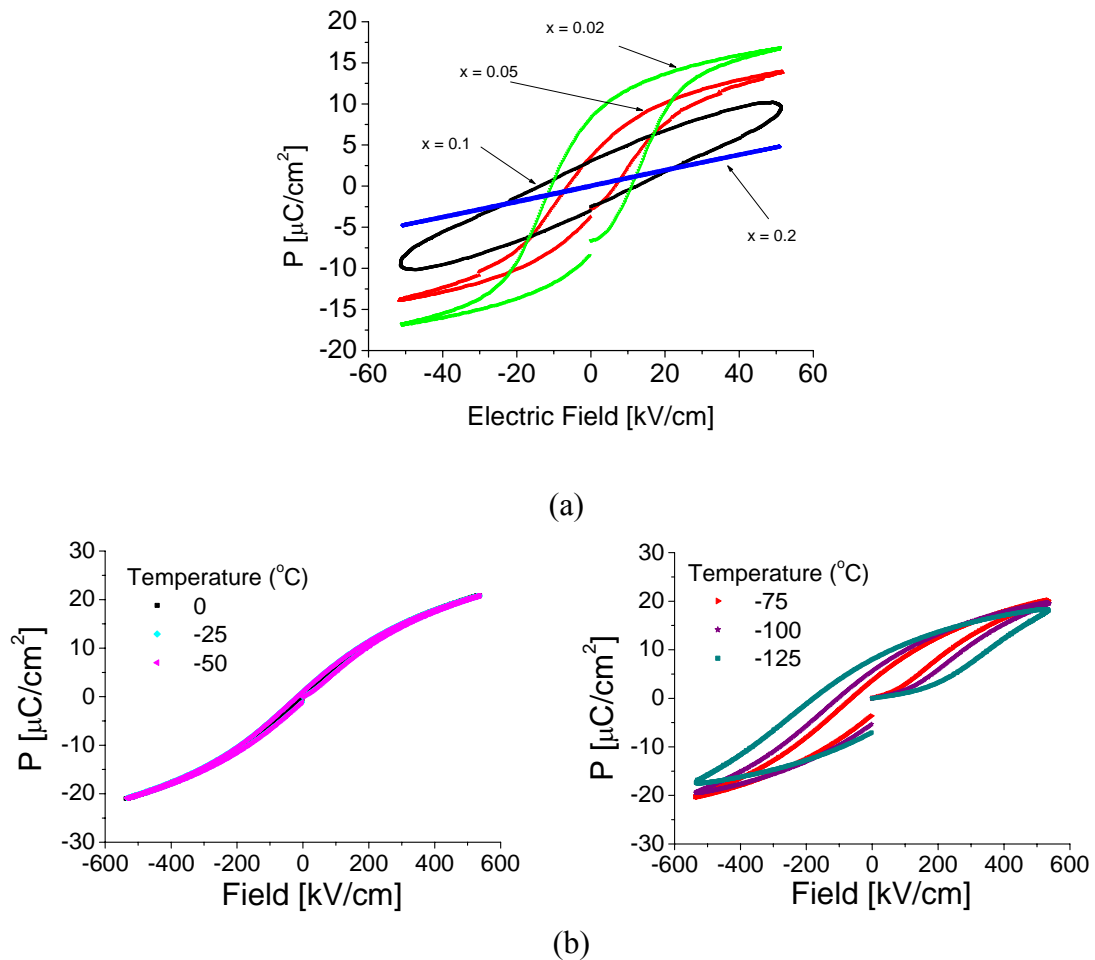
Figure 4.17.   Polarization vs. electric field data for (1-x) BaTiO$_3$ - x BiScO$_3$ ceramics for (a) x = 0.02, 0.05, 0.1 and 0.2 measured with a maximum field of 50 kV/cm and (b) x = 0.3 measured at various temperatures with a maximum field of ~ 550 kV/cm
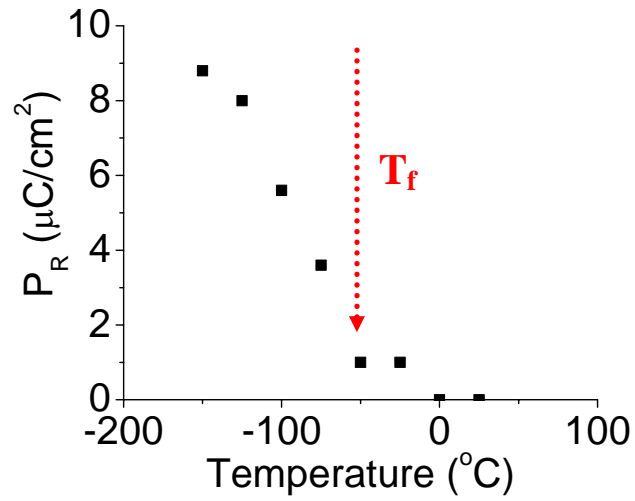
(a)
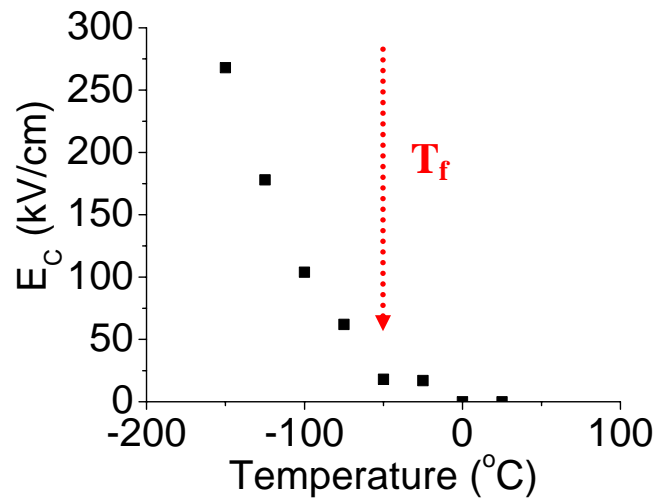
(b)

Figure 4.18.   (a) Remanent Polarization and (b) coercive field vs. temperature data for

0.7 BaTiO$_3$ - 0.3 BiScO$_3$ ceramics measured with an applied field of ~ 550 kV/cm

4.2 High Energy Density Capacitor Application

4.2.1 Compositions

As mentioned in section 1.1.2, 0.6 BaTiO$_3$ – 0.4 BiScO$_3$ thin films exhibited an energy density of 13 J/cm^3 for a bias field of about 1300 kV/cm (Tinberg and Trolier-McKinstry, 2007). To confirm if bulk ceramics with comparable composition show high energy density as well, 0.7 BaTiO$_3$ – 0.3 BiScO$_3$ ceramics, which have good high field resistance as shown in Figure 4.19, were employed for this investigation. 0.6 BaTiO$_3$ – 0.4 BiScO$_3$ ceramic samples showed significant dielectric losses above 200 °C, likely due to space charge conduction, as shown in Figure 4.9 (g).
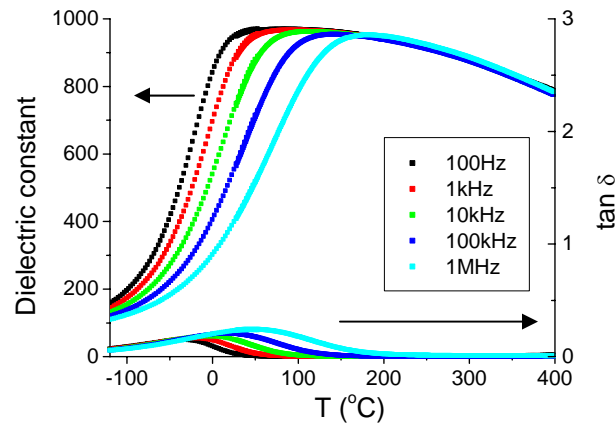
Figure 4.19. Dielectric constant and tan δ as a function of temperature of 0.7 BaTiO$_3$ - 0.3 BiScO$_3$ ceramics measured at frequencies between 100Hz and 1MHz

4.2.2 Pellet Samples

First, the dielectric breakdown strength of the ceramics was measured, since a reasonably high breakdown strength is essential in energy storage applications. Table 4.2 shows the breakdown strength as a function of sample thickness. Due to the small numbers of samples, Weibull analysis was not performed. Instead, an average strength was calculated for each thickness. It was found that the breakdown strength increases significantly with decreasing thickness (See Figure 4.20). The fit to the data was performed based on the assumption that the breakdown mechanism is dominated by thermal breakdown. Thus, the strength should be proportional to $d^{-1/2}$, where d is sample thickness (see section 2.11). The fit is not perfect, but it is clear that the sample has a reasonably high breakdown strength which should increase for thinner samples.

Table 4.2.   Dielectric breakdown strength of 0.7 $BaTiO_3$ - 0.3 $BiScO_3$ ceramics

Sample thickness [mm]	Dielectric breakdown strength [kV/cm]	Number of samples
0.91	117 ± 13.1	11
0.48	275 ± 39.1	7
0.31	205 ± 23.8	8
0.20	437 ± 81.2	9
0.08	879 ± 429	3
0.05	764 ± 52.3	6
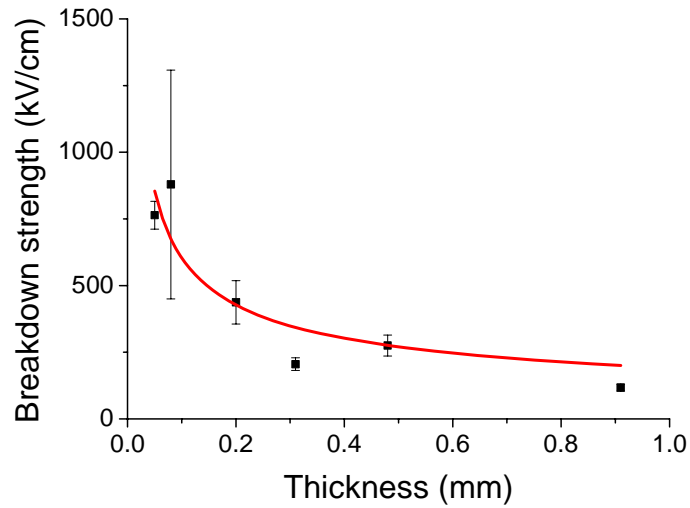
Figure 4.20.   Dielectric breakdown strength of 0.7 BaTiO$_3$ - 0.3 BiScO$_3$ ceramics as a

function of sample thickness.   The solid line is the fit proportional to d$^{-1/2}$, assuming

thermal breakdown mechanism.

Figure 4.21 shows room temperature polarization – electric field data on 0.2 mm

thick 0.7 BaTiO$_3$ - 0.3 BiScO$_3$ bulk ceramics.   An energy density of 2.3 J/cm^3 was

achieved at about 225kV/cm at room temperature.   This value is comparable to reported

data for X7R capacitors based on BaTiO$_3$ (about 2.0 J/cm^3 at 200kV/cm), as shown in

Figure 4.22 (Love, 1990).
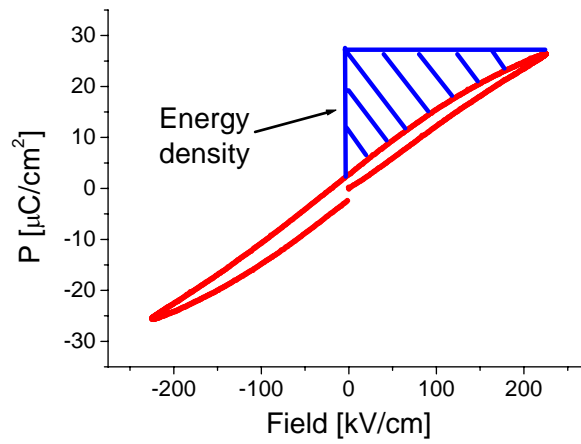
Figure 4.21.   Room temperature polarization vs. electric field data on 0.7 BaTiO$_3$ - 0.3

BiScO$_3$ pellet
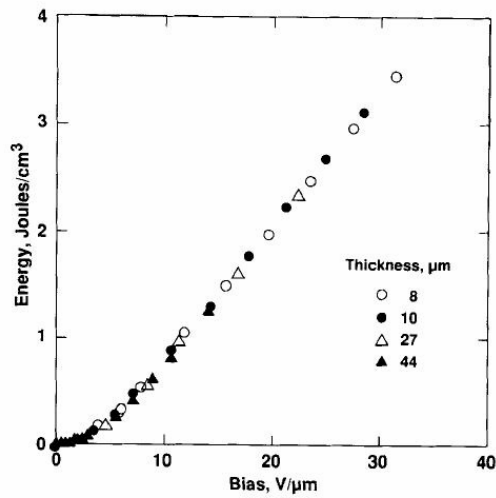
Figure 4.22.   Energy density vs. bias field for a C08 (X7R) capacitor (from Love, 1990)

4.2.3 Single Dielectric Layer Capacitors

To confirm the increase in energy density at small layer thicknesses, 0.7 BaTiO$_3$ - 0.3 BiScO$_3$ capacitors were prepared via tape casting with a dielectric thickness of about 25 to 50 μm. After sintering, dielectric layer thicknesses of $\geq$ 15 μm were achieved. Figure 4.23 shows a 33 μm thick dielectric layer with continuous electrode layers.
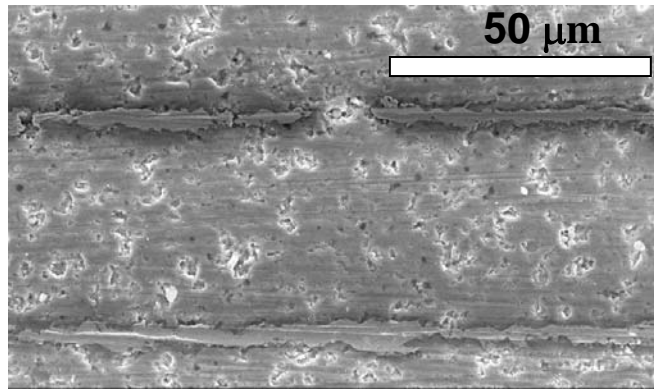
Figure 4.23.   SEM micrograph of the polished cross section of a 0.7 BaTiO$_3$ - 0.3 BiScO$_3$ thin dielectric layer capacitor

Figure 4.24 shows the dielectric constant as a function of temperature for the capacitor with a dielectric layer thickness of 27 μm. The apparent maximum dielectric constant value for the capacitor is smaller (750-800) than that of pellet samples (1000). This difference is due in part to the lower density of the tape cast samples. If it is assumed that the low density of the capacitor is responsible for all of the degradation in dielectric constant, it was estimated that the sample was about 82% of theoretical density (using a dielectric constant of 775 for the capacitor, and assuming the pellet is 98%

theoretical density with a dielectric constant of 1000). This was done using the Maxwell mixing rule dielectric constant (Kingery et al., 1976),

$$K = [V_M K_M (2/3+ K_D/3 K_M) + V_D K_D] / [V_M (2/3+ K_D/3 K_M) + V_D] \qquad (4.5)$$

where K, K_M, and K_D are dielectric constant for the mixture, a matrix, and a spherical particle, and V_M and V_D are volume fraction of the matrix and the particle, respectively. However, such a low density is inconsistent with the observed high dielectric breakdown strength and low dielectric loss. Thus, while a lower density accounts for some of the decreased dielectric constant, it cannot be the only factor. Inaccuracy in estimating the electrode area or dielectric thickness for the capacitor samples can be a source of error as well.
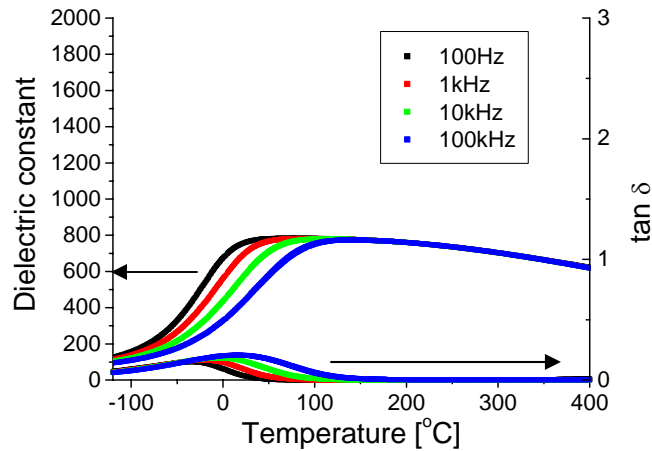
Figure 4.24. Dielectric constant and dielectric loss tangent data as a function of temperature from 100 Hz to 100 kHz for a 0.7 BaTiO$_3$ - 0.3 BiScO$_3$ capacitor with 27 μm thick dielectric layers

Figure 4.25 shows the high field polarization data for a thin layer 0.7 BaTiO$_3$ - 0.3 BiScO$_3$ capacitor from -180 to 340 ^{o}C. It was found that the hysteresis loop opened

up both at low (around -150 °C) and high (> 300 °C) temperatures. The high

temperature hysteresis is probably due to a conduction contribution. The slopes of the

curves around zero field become smaller for lower temperature measurements as

expected from the decrease in dielectric constant at low temperatures shown in Figure

4.24.

(a)

(b)

(c)
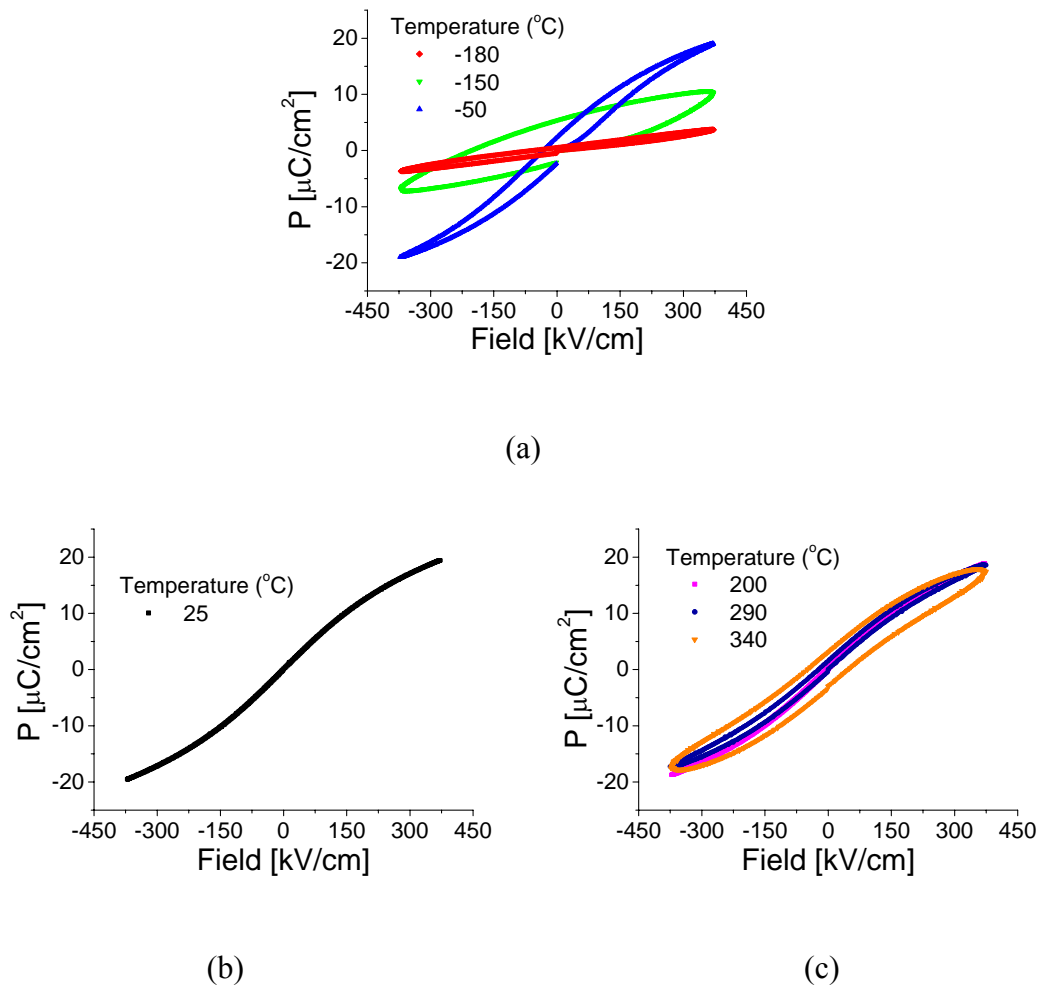
Figure 4.25.   Polarization vs. electric field data on a 0.7 BaTiO$_3$ - 0.3 BiScO$_3$ capacitor

at various temperatures, (a) from -180 to -50 °C, (b) room temperature, and (c) from 200

to 340 °C

Figure 4.26 and 4.27 show the energy density vs. applied field at different temperatures and the energy density vs. temperature, respectively. The energy density at room temperature for the thin dielectric layer capacitor was 1.4 J/cm^3 at 220 kV/cm, which is inferior to the value for the pellet sample, 2.3 J/cm^3 at 225 kV/cm. This difference can be explained by the difference in dielectric constant and the polarization behavior under high fields between the capacitor sample and the pellet sample as shown in Figure 4.28. At 730 kV/cm, right before the breakdown for the sample with dielectric layer thickness of 15 μm, a high energy density, ~ 6.1 J/cm^3 was achieved at room temperature, which may be appealing for some high energy applications.

Another aspect which may be attractive for some applications is that the capacitor exhibits excellent temperature stability from 0 ^{o}C up to about 300 ^{o}C with a relatively high energy density value, as shown in Figure 4.27.
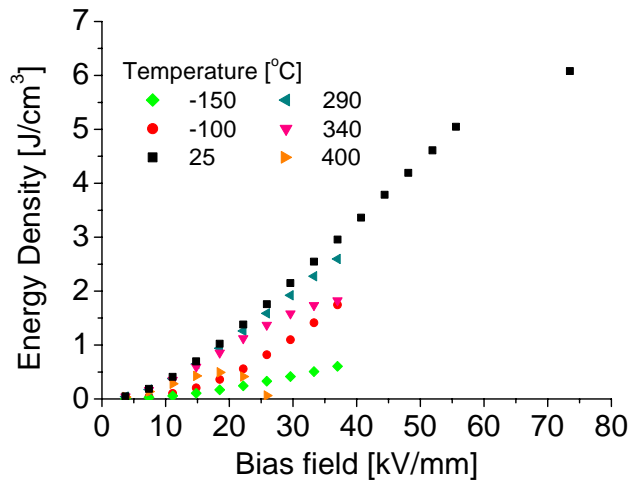
Figure 4.26. Energy density vs. bias field for a 0.7 BaTiO$_3$ - 0.3 BiScO$_3$ thin dielectric layer capacitor at room temperature
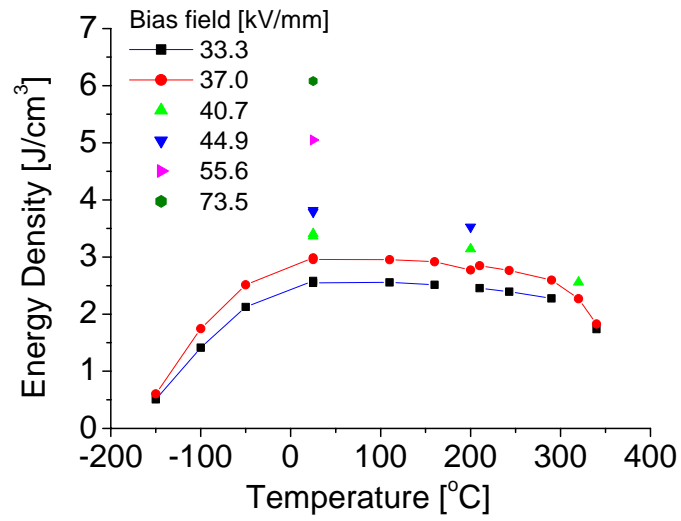
Figure 4.27.   Energy density vs. temperature for a 0.7 BaTiO$_3$ - 0.3 BiScO$_3$ thin

dielectric layer capacitor at various bias fields
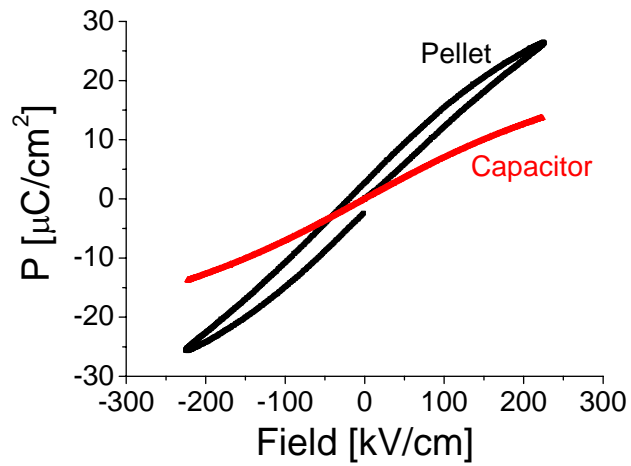
Figure 4.28.   Polarization vs. electric field data on a 0.7 BaTiO$_3$ - 0.3 BiScO$_3$ capacitor

and a pellet, showing the difference in energy density values

4.2.4 Comparison with Commercial Capacitors

The energy storage capability of 0.7 BaTiO$_3$ - 0.3 BiScO$_3$ capacitors was compared to that of commercial capacitors, a C0G, a base metal electrode X7R (X7R BME), and a precious metal electrode X7R (X7R PME). The Electronic Industries Alliance (EIA) standard defines C0G parts as possessing TCC of 0 +/- 30 ppm/^{o}C and X7R as showing a +/- 15% capacitance deviation from its room temperature value over the temperature range of -55 to 125 ^{o}C. An emphasis was placed on the temperature stability of the energy storage characteristics.

Table 4.3 lists the sample dimensions, room temperature capacitance, dielectric constant and loss tangent at 10 kHz, as well as the energy density at room temperature. Figures 4.29 and 4.30 show the energy density as a function of bias field and the polarization for the commercial capacitors compared to the 0.7 BaTiO$_3$ - 0.3 BiScO$_3$ capacitor data at room temperature, respectively. The energy density values for the X7R materials examined here were lower than that obtained by Love (Love, 1990): about 1 J/cm^3 for the X7R material in this study compared to the 2 J/cm^3 reported by Love at 20 kV/mm. More importantly, it is clear from Figure 4.29 that the 0.7 BaTiO$_3$ - 0.3 BiScO$_3$ capacitor possesses superior energy storage capability to the three commercial capacitors at the same applied electric field.

Table 4.3. Comparison of the energy storage capacitor of a 0.7 BaTiO$_3$ - 0.3 BiScO$_3$ dielectric compared with commercial capacitors at room temperature

sample	dielectric layer thickness [μm]	effective electrode area for one layer [cm^2]	Dielectric Layers	Total electrode area [cm^2]
0.7 BaTiO$_3$ - 0.3 BiScO$_3$ (this study)	27	0.133	1	0.133
X7R BME	7.5	0.0071	62	0.443
X7R PME	8.3	0.0057	61	0.348
C0G	2.8	-	330	9

sample	capacitance at 10 kHz [nF]	tan δ at 10 kHz	dielectric constant at 10 kHz	Energy density at 35 kV/mm [J/cm^3]
0.7 BaTiO$_3$ - 0.3 BiScO$_3$ (this study)	2.85	0.15	650	2.7
X7R BME	92.8	0.0013	1780	1.5
X7R PME	94.3	0.0013	2540	1.5
C0G	97.0	0.00006	34	0.2
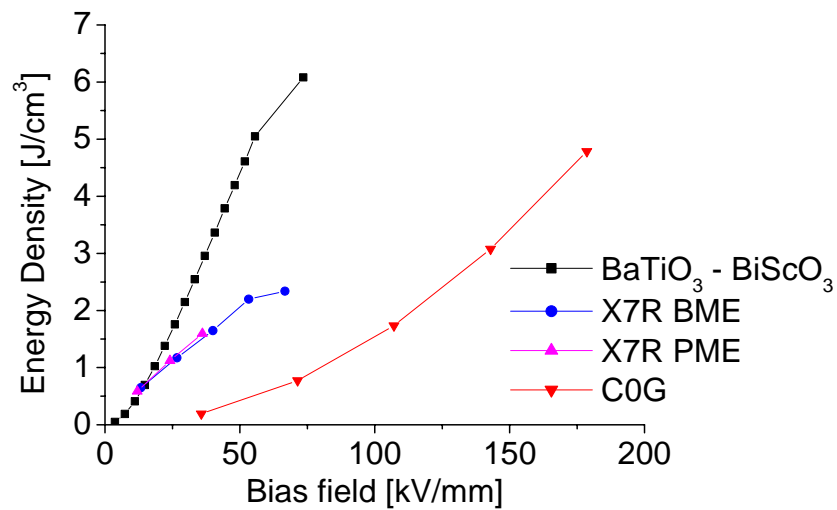
Figure 4.29. Stored energy density as a function of bias field at room temperature for commercial capacitors and a 0.7 BaTiO$_3$ - 0.3 BiScO$_3$ dielectric
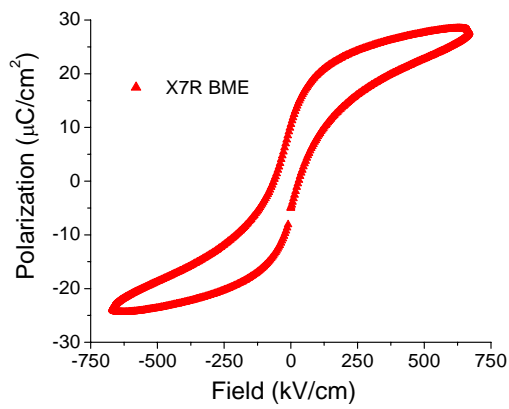
(a)
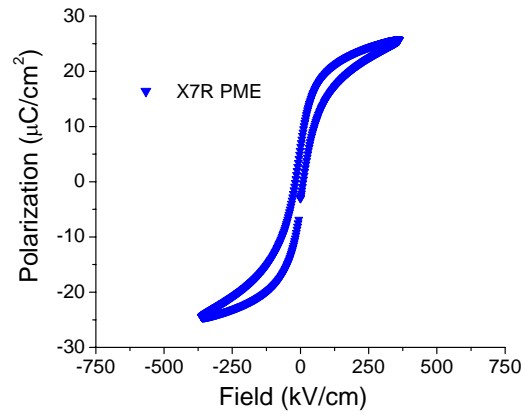
(b)
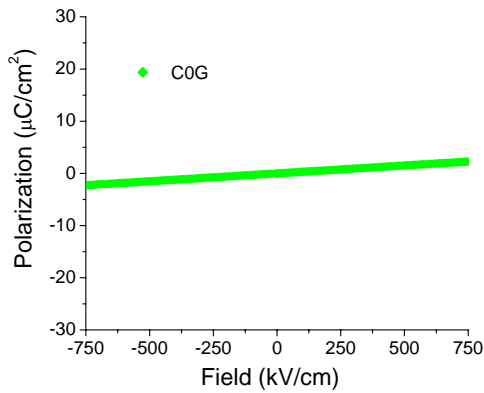
(c)
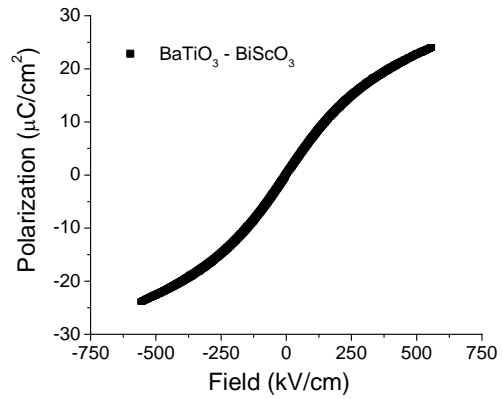
(d)

Figure 4.30.   Comparison of the room temperature polarization - field data for three

commercial capacitors (a) X7R BME, (b) X7R PME, (c) C0G and (d) a 0.7 BaTiO$_3$ - 0.3

BiScO$_3$ dielectric

To examine the temperature stability of the stored energy density, the
polarization was measured as a function of the applied electric field at 200 ^{o}C and 320 ^{o}C.
Figure 4.31 shows the polarization – field data and the calculated energy as a function of
electric field for the three commercial capacitors.

The X7R capacitors became significantly leaky at 320 ^{o}C, resulting in open loops, as shown in Figure 4.31 (a) and (b). Even at 200 ^{o}C, the energy density values at about 35 kV/mm for the X7R BME and PME capacitors are about 33% lower than the room temperature values. This result was expected from the fact that X7R capacitors are targeted for the temperature range of -55 to +125 ^{o}C. Moreover, the transition temperature of BaTiO$_3$ - based formulation is well below 200 ^{o}C.

In contrast, the C0G capacitor exhibits a stable energy density as a function of temperature; no significant change is apparent between 20 and 320 ^{o}C, as shown in Figure 4.31 (c). The stability of the C0G capacitor is superior to that of the 0.7 BaTiO$_3$ - 0.3 BiScO$_3$ capacitor. However, as shown in Figure 4.29, the energy density value at the same electric field is much larger for the 0.7 BaTiO$_3$ - 0.3 BiScO$_3$ capacitor than for the C0G capacitor. Depending on the application, the 0.7 BaTiO$_3$ - 0.3 BiScO$_3$ capacitor may be more attractive due to its high energy storage capability and almost temperature independent behavior from 0 to 300 ^{o}C.
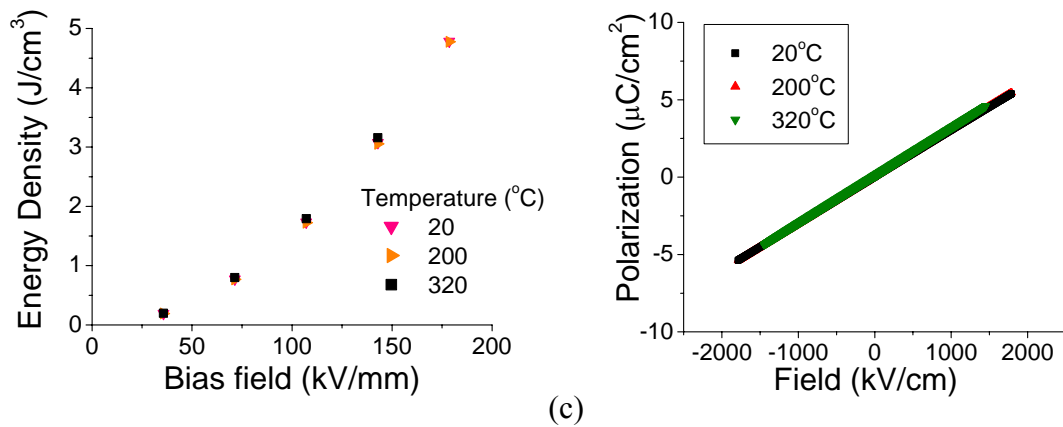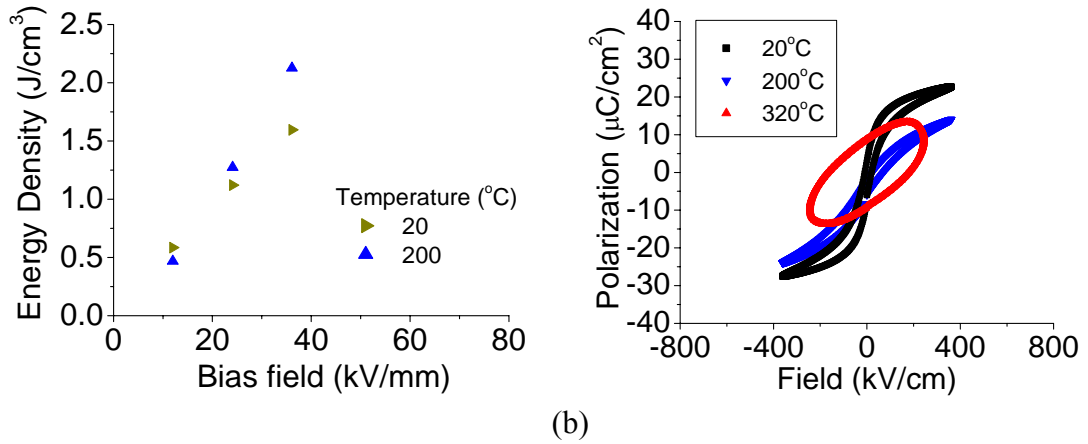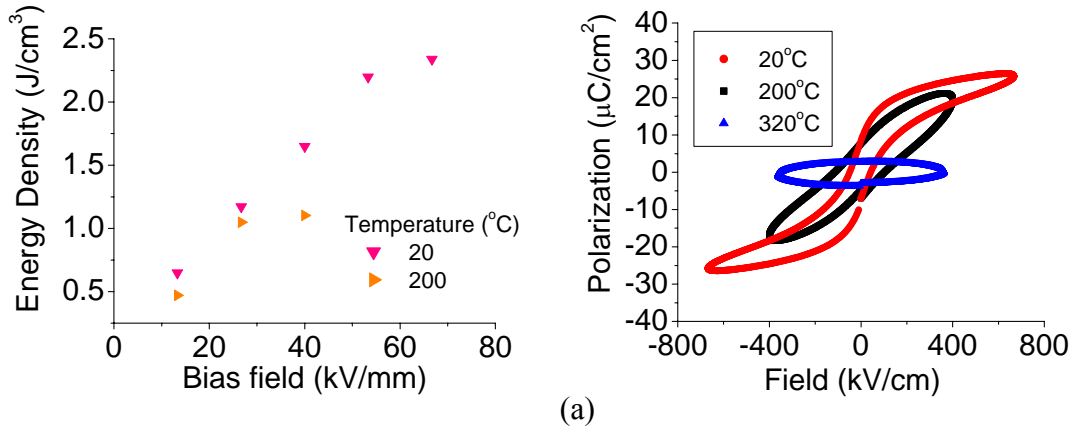
Figure 4.31. Energy density vs. bias field and polarization vs. electric field at various temperatures for commercial capacitors (a) X7R BME, (b) X7R PME, and (c) C0G

4.3 Off-center Ion Doping

As was reported previously for thin films (Tinberg and Trolier-McKinstry, 2007), a diffusive, broad dielectric maxima was observed here for most of the compositions studied in the $BaTiO_3$ - $BiScO_3$ system. The undoped ceramics showed slim room temperature hysteresis loops, which are not suitable for piezoelectric applications. Figure 4.32 illustrates room temperature unipolar strain vs. applied field and polarization data for 0.9 $BaTiO_3$ – 0.1 $BiScO_3$ ceramics. Table 4.4 lists the electrostrictive coefficients, M_{33} and Q_{33}, estimated from these unipolar strain behaviors for $BaTiO_3$ - $BiScO_3$ ceramics and lead magnesium niobate (PMN) ceramics (a commercially available electrostrictive material). No obvious compositional trend was found in the system, except the coefficients for x = 0.1 were slightly higher than the other compositions. Although the Q coefficient for the $BaTiO_3$ - $BiScO_3$ system is close to the value for PMN, the electrostrictive properties of this system are inferior to that of PMN. Commercially available electrostrictive materials such as PMN or lead magnesium niobiate - lead titanate solid solutions (PMN - PT) achieve high electrostrictive properties due to their high dielectric constant (> 5000); for example, the 0.85 PMN - 0.15 PT ceramic by TRS Technologies achieves 0.1% strain at a field of 2 x 10^6 V/m at room temperature, which is almost two orders of magnitude higher than that of the $BaTiO_3$ – $BiScO_3$ system.

In the present formulation, the intrinsic piezoelectric coefficient is limited by the relaxor nature and the very small P_R. Consequently, it is interesting to consider whether it is possible to stabilize the polarization to make the material more suitable as a piezoelectric, possibly by doping off-center ions to change the slim hysteresis loops into more square looking loops.

(a)   (b)
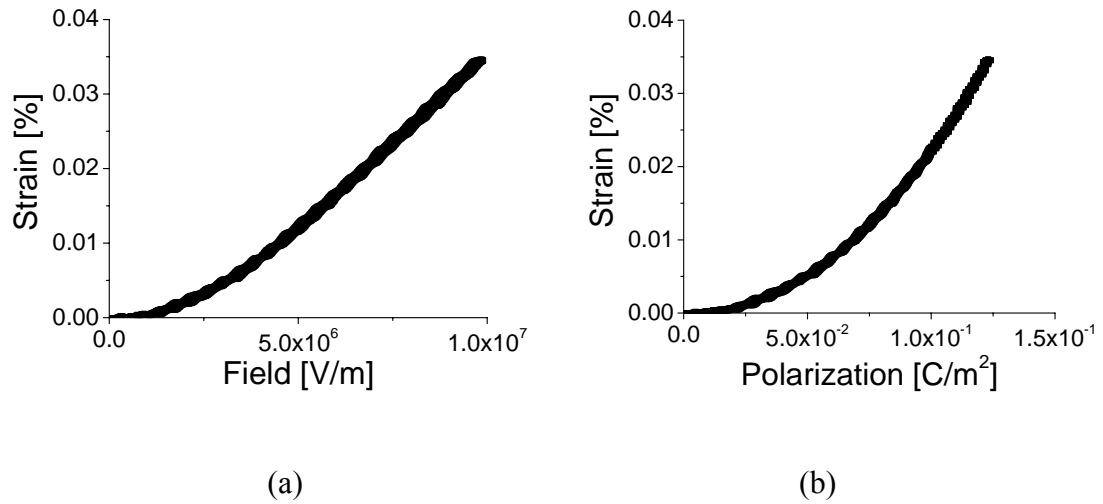
Figure 4.32.   Unipolar strain vs. (a) applied field and (b) polarization for 0.9 $BaTiO_3$ - 0.1 $BiScO_3$ ceramics at room temperature

Table 4.4.   Room temperature electrostrictive coefficient M_{33} and Q_{33} for several compositions in (1-x) $BaTiO_3$ – x $BiScO_3$ and PMN ceramics

Sytem	x	M_{33} [10^{-18} m^2/V^2]	Q_{33} [10^{-2} m^4/C^2]	Ref
(1-x) $BaTiO_3$ - x $BiScO_3$ (This study)	0.1	3.9 +/- 0.01	2.2 +/- 0.002	-
	0.2	1.1 +/- 0.002	1.3 +/- 0.002	
	0.3	0.84 +/- 0.002	1.3 +/- 0.005	
	0.4	0.84 +/- 0.003	1.1 +/- 0.004	
$Pb(Mg_{1/3}Nb_{2/3})O_3$ (PMN)	-	-	2.3 +/- 0.2	Kuwata et al., 1980

4.3.1 Li-doped Samples

Li doping of the system was employed in an attempt to stabilize a normal ferroelectric in this highly polarizable system, following the work of Sakabe on $Ag(Nb_{1/2}Ta_{1/2})O_3$ (Sakabe, 2001).

4.3.1.1 Compositions

(1-x) $BaTiO_3$ - x $BiScO_3$ compositions with x = 0.1 and 0.3 were employed as the base ceramics.   As Figure 4.33 shows, ceramics with x = 0.1 exhibit two peaks in the permittivity as a function of temperature, associated with the core-shell structure as described in the previous section, whereas x = 0.3 has a dielectric constant of about 1000 over a wide range of temperature.   0, 1, 5, 10, or 15 mol% $LiNbO_3$ was added to these base compositions.   Nb was added with Li in order to maintain electroneutrality.

Thus, the compositions studied were:

(1-y) (0.9 $BaTiO_3$ - 0.1 $BiScO_3$) – y $LiNbO_3$, with y = 0, 0.01, 0.05, 0.10, and 0.15

(1-y) (0.7 $BaTiO_3$ - 0.3 $BiScO_3$) – y $LiNbO_3$, with y = 0, 0.01, 0.05, 0.10, and 0.15

(a)   (b)
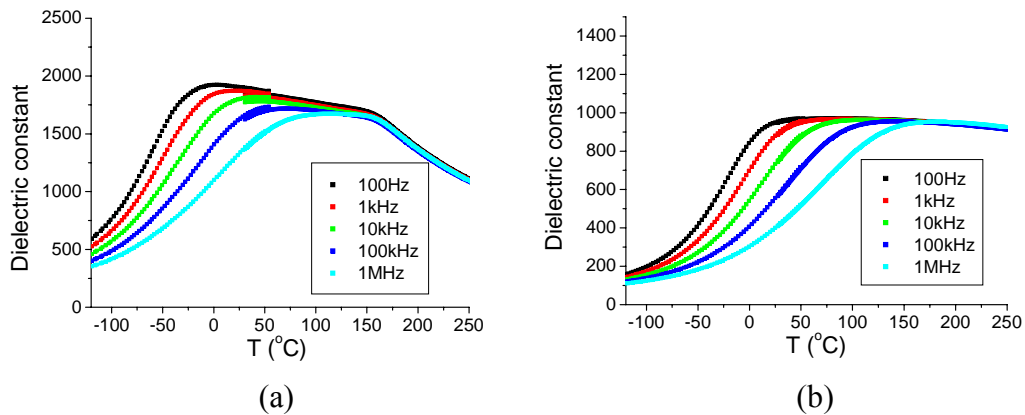
Figure 4.33.   Dielectric constant data on unpoled (1-x) $BaTiO_3$ - x $BiScO_3$ samples with (a) x = 0.1 and (b) x = 0.3

95

4.3.1.2 Structural and Dielectric Properties

The x-ray diffraction measurements showed that all of the compositions with y = 0 – 0.10 could be prepared with only minor amounts of non-perovskite phases, as shown in Figure 4.34 (a). Undesired second phases were clearly observed on the sample with y = 0.15, shown in Figure 4.34 (b). Figure 4.35 plots the lattice parameters calculated from the XRD data assuming a pseudocubic phase as a function of composition. Although the undesired second phases were not obvious from the XRD for compositions up to y = 0.1, the calculated lattice parameters do not show a linear trend with increasing $LiNbO_3$ concentration, indicating that solid solution was not achieved.

(a)   (b)
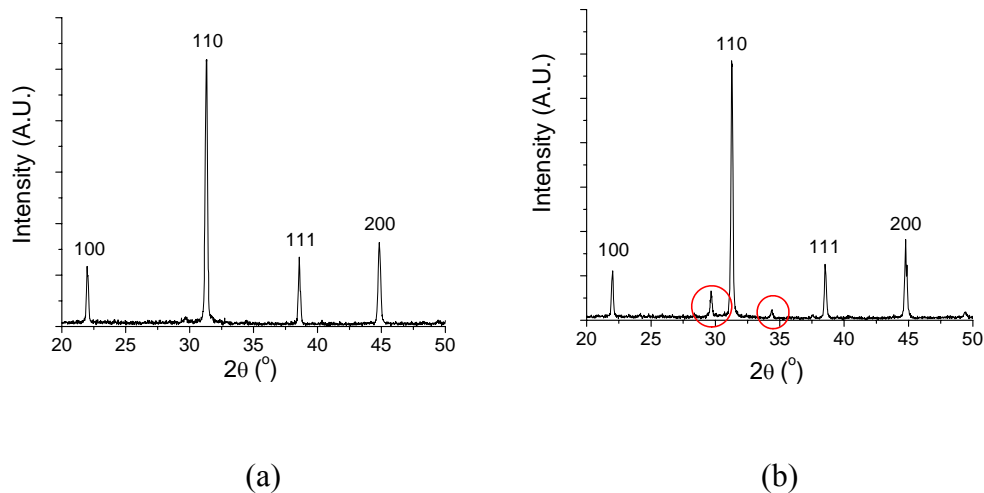
Figure 4.34.   X-ray diffraction patterns of (1-y) [(1-x) $BaTiO_3$ - x $BiScO_3$] - y $LiNbO_3$ ceramics after sintering.   The indexing is done based on a pseudocubic perovskite unit cell (a) x = 0.3, y = 0.10 and (b) x = 0.3, y = 0.15
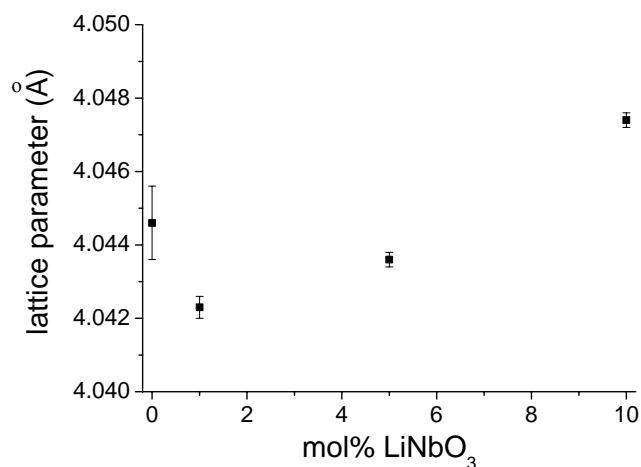
Figure 4.35. Lattice parameters of (1-y) (0.7 BaTiO$_3$ - 0.3 BiScO$_3$) - y LiNbO$_3$ ceramics

as a function of LiNbO$_3$ concentration (measured on powdered samples after sintering)

Figure 4.36 is a TEM micrograph on (1-y) (0.9 BaTiO$_3$ - 0.1 BiScO$_3$) − y

LiNbO$_3$ with y = 0.01.   There appear to be pockets of a second phase, as observed in the

figure; the circled regions are smaller in size and differ in color contrast from the

surrounding big grains, which may suggest a compositional difference between the two

phases.   This result supports the conclusion from the lattice parameter data that the

LiNbO$_3$ added was not incorporated in the BaTiO$_3$ - BiScO$_3$ matrix.   Compositional

mapping was tried to confirm this.   Unfortunately, Li concentration gradients are

difficult to detect by EDS as the electron configuration of Li ion does not allow

generation of x-ray radiation.   Instead, Nb concentration differences throughout the

sample were investigated based on the assumption that the Nb^{5+} ion would tend to be

coupled with the Li^{1+} ion.   However, no significant Nb concentration gradient was

observed by EDS.   Multiple calcinations (up to four times) and longer sintering times

(up to 20 hours) were attempted to achieve a solid solution, but no significant changes were observed.
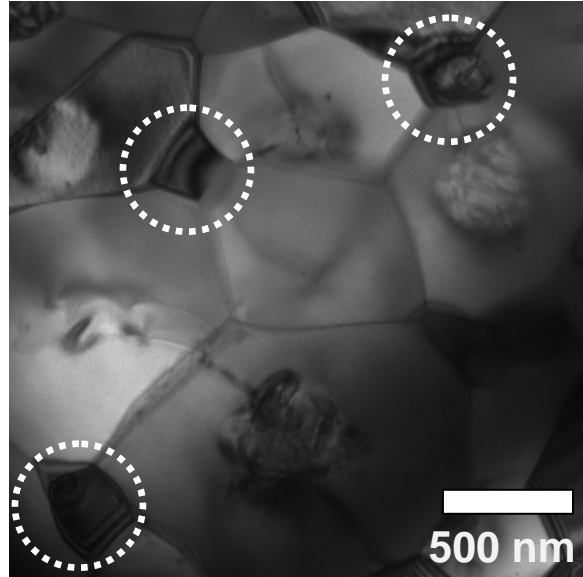
Figure 4.36.   TEM micrograph on (1-y) (0.9 BaTiO$_3$ - 0.1 BiScO$_3$) – y LiNbO$_3$ with y = 0.01.   The circled regions are believed to be from a second phases.

Figure 4.37 shows the resulting dielectric behavior for (1-y) (0.7 BaTiO$_3$ - 0.3 BiScO$_3$) – y LiNbO$_3$ ceramics with (a) y = 0, (b) y = 0.01, (c) y = 0.05, and (d) y = 0.10. It is clearly observed that the more LiNbO$_3$ is added to the system, the smaller the dielectric constant the material has.   The shape of the curve for each composition is similar, including comparable temperatures for the maxima of the dielectric constant. This suggests that a minor amount of second phase dominates the changes observed on doping, as predicted from the structural results.   Thus, it is highly likely that these materials do not possess the desired normal ferroelectric properties.   Figure 4.38 shows polarization vs. electric field measurement on (1-y) (0.7 BaTiO$_3$ - 0.3 BiScO$_3$) – y

LiNbO$_3$, with y = (a) 0, (b) 0.01, (c) 0.05, and (d) 0.10, which confirms that the Li added

did not stabilize a normal ferroelectric in the BaTiO$_3$ - BiScO$_3$ based system, presumably

because it was not properly incorporated into the matrix.   The same trend was observed

for the compositions with (1-y) (0.9 BaTiO$_3$ - 0.1 BiScO$_3$) – y LiNbO$_3$.

(a)

(b)

(c)

(d)
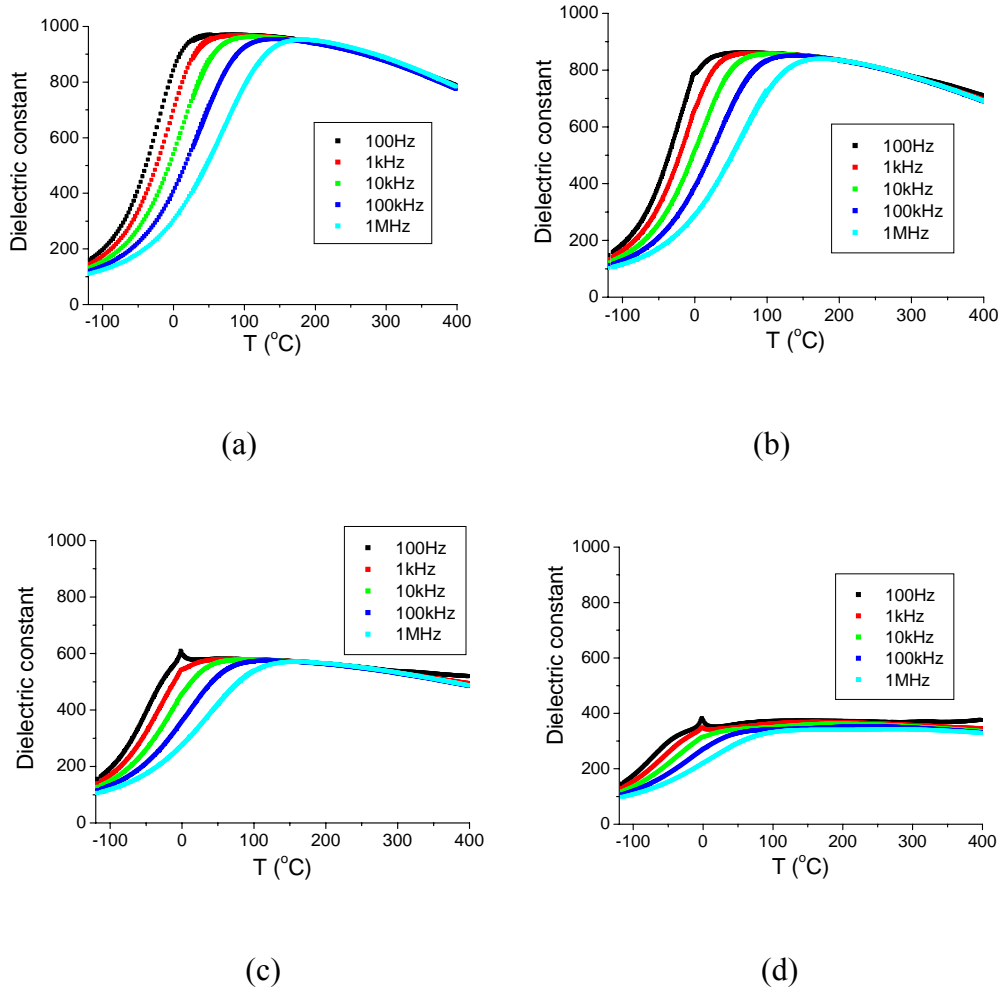
Figure 4.37.   Dielectric constant data on unpoled (1-y) (0.7 BaTiO$_3$ - 0.3 BiScO$_3$)

– y LiNbO$_3$ ceramics with (a) y = 0, (b) y = 0.01, (c) y = 0.05, and (d) y = 0.10
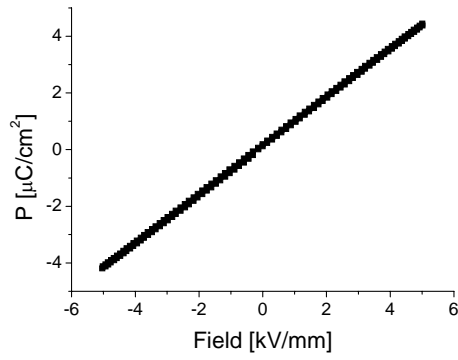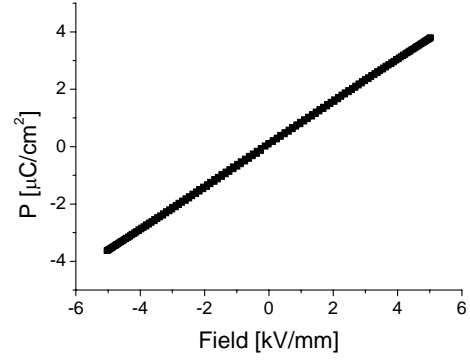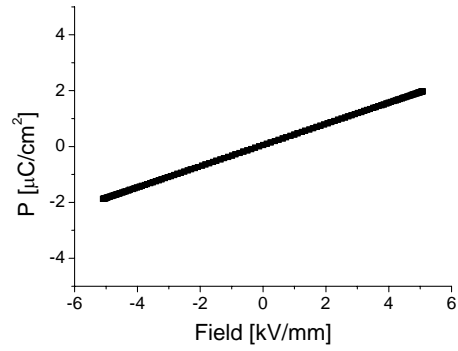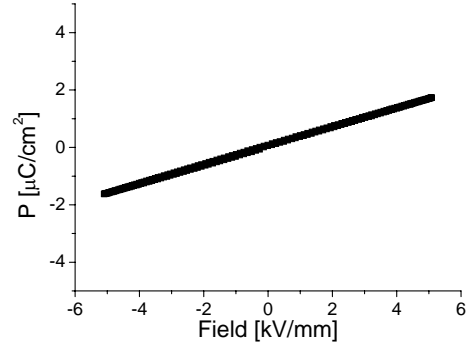
Figure 4.38.   Polarization vs. electric field data on (1-y) (0.7 BaTiO$_3$ - 0.3 BiScO$_3$) – y

LiNbO$_3$ samples with (a) y = 0, (b) y = 0.01, (c) y = 0.05, and (d) y = 0.10

Although no Nb concentration gradient was observed across the sample, Li-doping without Nb co-doping was attempted.   The result was similar to the ceramics with Nb, as shown in Figure 4.39 for a 1% Li-doped 0.6 BaTiO$_3$ - 0.4BiScO$_3$.
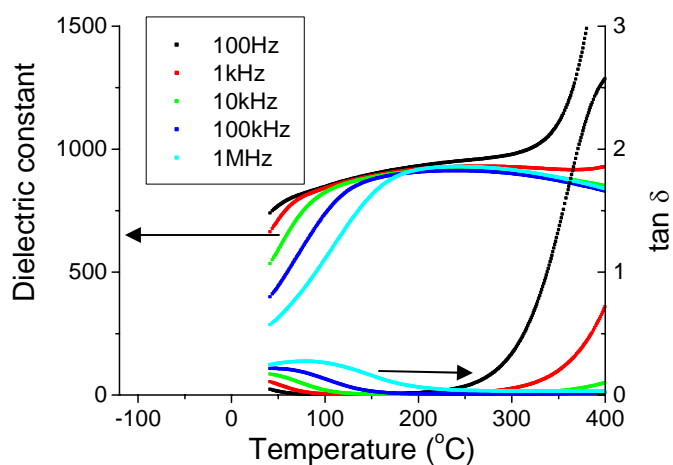
Figure 4.39.   Dielectric constant and tan δ vs. temperature for a 1% Li-doped 0.6

BaTiO$_3$ - 0.4 BiScO$_3$ ceramics

4.3.2   Na- doped samples

Due to the poor observed solubility of Li in the BaTiO$_3$ - BiScO$_3$ matrix, Na doping was also attempted.   As shown in Table 4.5, the Na^{1+} ion is larger than Li^{1+}, which may help to increase the solubility into the BaTiO$_3$ - BiScO$_3$ system.   Yet, Na^{1+} is still smaller than Ba^{2+}, therefore it may work as an off-center ion to stabilize a normal ferroelectric.

Table 4.5.   Shannon ionic radius for Ba, Bi, Li, and Na ions.   Note that the radius of Bi^{2+} ion for 12 coordination was extrapolated from the radii for other coordinations (after Shannon, 1976).

		Shannon ionic radius [Å]	
		12 coordination	8 coordination
A site ion in perovskite	Ba^{2+}	1.61	1.42
	Bi^{3+}	1.34	1.17
Possible off-center ion	Li^{1+}	-	0.92
	Na^{1+}	1.39	1.18

4.3.2.1   Compositions

As with the Li doping, the $0.7\ BaTiO_3 - 0.3\ BiScO_3$ was employed as the base ceramic.   0, 1, 5, 10, or 15 mol% of $NaNbO_3$ was added to the base composition.   Nb was added with the Na or K in order to maintain electroneutrality, as for the Li doping.

Thus, the compositions studied were:

$(1-y)\ (0.7\ BaTiO_3 - 0.3\ BiScO_3) - y\ NaNbO_3$, with $y = 0$, 0.01, 0.05, 0.10, and 0.15.

4.3.2.2   Structural and Dielectric Properties

The x-ray diffraction measurements show formation of the perovskite phase for all of the compositions with $y = 0 - 0.15$ (See Figure 4.40 for $y = 0.15$), unlike the Li doping case where undesired 2nd phases were clearly observed on the sample with $y = 0.15$.   The different behavior should be associated with the higher Na solubility in the system than that of Li, most likely due to the improved match between the sizes of the

dopant and the host site.   Figure 4.41 plots the lattice parameters calculated from the

XRD data assuming a pseudocubic phase.   The lattice parameter continuously and

linearly decreases with increasing $NaNbO_3$ concentration, which is consistent with

Vegard's law (Vegard, 1921) suggesting solid solution.
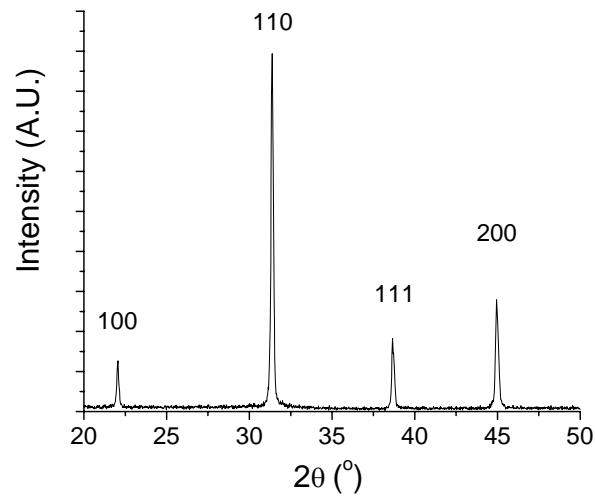
Figure 4.40.   X-ray diffraction pattern of a 0.85 (0.7 $BaTiO_3$ - 0.3 $BiScO_3$) – 0.15

$NaNbO_3$ ceramic after sintering.   The indexing is done based on a pseudocubic

perovskite unit cell.
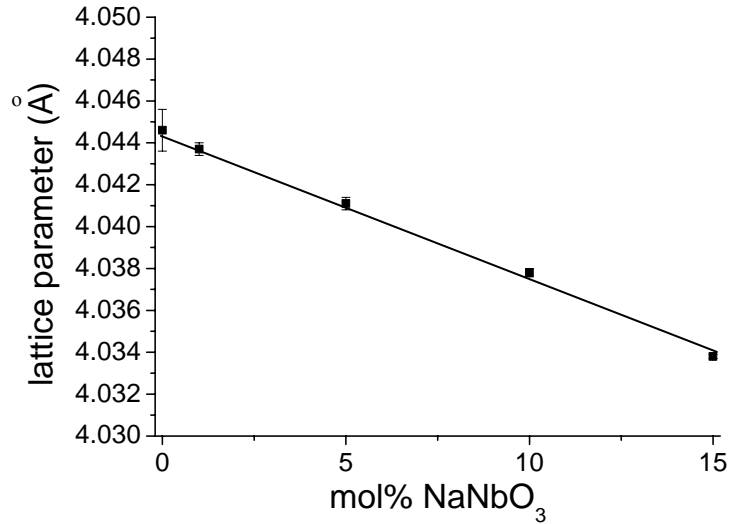
Figure 4.41. Lattice parameters of (1-y) (0.7 BaTiO$_3$ - 0.3 BiScO$_3$) – y NaNbO$_3$

ceramics as a function of NaNbO$_3$ concentration (measured on powdered samples after

sintering)

Figure 4.42 shows the dielectric measurements on (1-y) (0.7 BaTiO$_3$ - 0.3 BiScO$_3$) – y NaNbO$_3$, with y = (a) 0, (b) 0.01, (c) 0.05, (d) 0.10, and (e) 0.15. As in Li doping, there was no indication that Na doping stabilized a normal ferroelectric in the system. Also, as more NaNbO$_3$ is added to the system, the dielectric constant of the material decreases. This is correlated with a decrease in T$_{max}$ with increasing NaNbO$_3$ concentration.
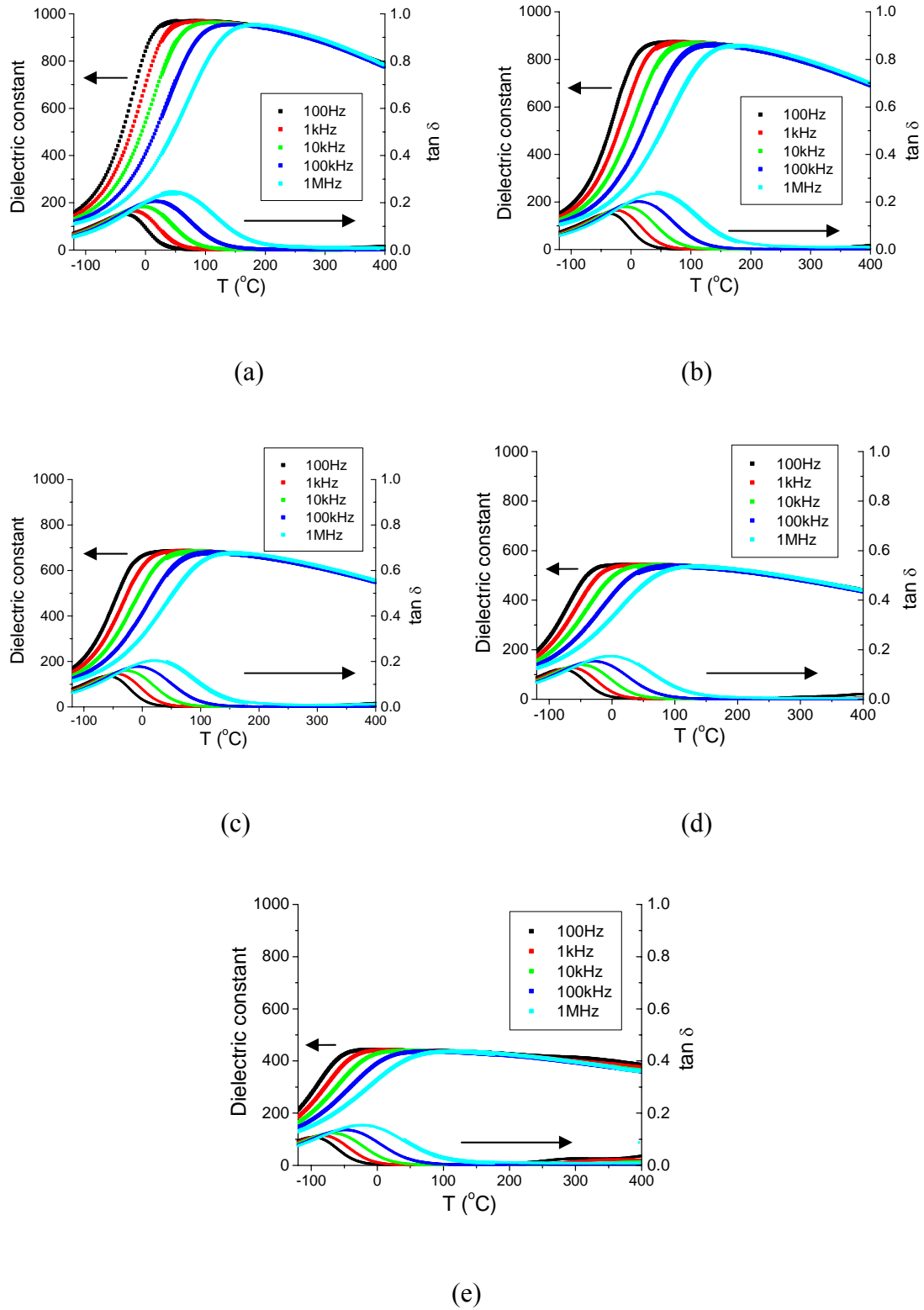
Figure 4.42.   Dielectric constant data on unpoled (1-y) (0.7 BaTiO$_3$ - 0.3 BiScO$_3$) – y

NaNbO$_3$ samples with (a) y = 0, (b) y = 0.01, (c) y = 0.05, (d) y = 0.10 and (e) y = 0.15

Table 4.6 lists the room temperature electrostrictive coefficients, M_{33} and Q_{33}, estimated from the unipolar strain behaviors for (1-y) (0.7 BaTiO$_3$ - 0.3 BiScO$_3$) – y NaNbO$_3$ ceramics. Q_{33} was invariant as a function of the NaNbO$_3$ concentration, but M_{33} decreases with increasing NaNbO$_3$ concentration. This is consistent with the decrease in dielectric constant with increasing NaNbO$_3$ concentration (M = Q ε_0^2 ε_r^2).

Table 4.6. Room temperature electrostrictive coefficient M_{33} and Q_{33} for several compositions in (1-y) (0.7 BaTiO$_3$ - 0.3 BiScO$_3$) - y NaNbO$_3$ ceramics

y	M_{33} [10^{-19} m^2/V^2]	Q_{33} [10^{-2} m^4/C^2]
0	8.4 +/- 0.02	1.3 +/- 0.005
0.01	7.2 +/- 0.03	1.3 +/- 0.004
0.05	4.6 +/- 0.02	1.2 +/- 0.006
0.10	3.1 +/- 0.01	1.3 +/- 0.005
0.15	2.3 +/- 0.01	1.5 +/- 0.005

To investigate the T_{max} in terms of the relaxor behavior, Vogel-Fulcher analysis was performed on the NaNbO$_3$ doped samples, as described in section 4.1.5. The maxima in dielectric loss (tan δ) were employed to define T_{max} instead of the dielectric constant due to the flat dielectric behavior. Figure 4.43 shows the Vogel-Fulcher plot for compositions y = 0 – 0.15. Excellent fittings (R^2 > 0.999 for all compositions) were achieved for all of the data. Figure 4.44 plots the key parameters, namely, the activation energy, the attempt frequency, and freezing temperature values obtained from the Vogel-Fulcher fit as a function of BiScO$_3$ concentration with the 95% confidence intervals obtained in the fitting. The attempt jump frequency (on the order of 10^{13} Hz) and the high activation energy (~ 0.25 eV) are consistent with the undoped samples.

The attempt jump frequency and the activation energy appear to increase with increasing $NaNbO_3$ concentration, but the relatively large confidence limits make it difficult to judge.   On the other hand, it is clear that the freezing temperature decreases with increasing $NaNbO_3$ concentration.   In addition, T_{max} decreases with increasing $NaNbO_3$ concentration, as shown in Figure 4.45.   Interestingly, the decrease in T_f is much larger than the decrease which would be expected just from the $BiScO_3$ dilution due to the $NaNbO_3$ addition; for example, 15 mol% $NaNbO_3$ doping in 0.7 $BaTiO_3$ - 0.3 $BiScO_3$ reduces the $BiScO_3$ content to ~ 25 mol% in the system.   If only the dilution of $BiScO_3$ was responsible for the decrease in T_f, the decrease would be only 10 - 15 ^{o}C with 15 mol% $NaNbO_3$ doping as shown in section 4.1.5.   This is much smaller than the experimental drop of ~ 75 ^{o}C.   This result implies that $NaNbO_3$ doping breaks up the polar ordering developed in the $BaTiO_3 - BiScO_3$ system and the system is driven towards $T_f \rightarrow 0$, which is the case for non-interacting dipoles.   This might suggest that Na simply decreases the size of the unit cell, and does not off-center to stabilize a normal ferroelectric (enhance the long-range order).   The fundamental origin of the differences in the roles of dopants is not well understood and needs to be investigated.
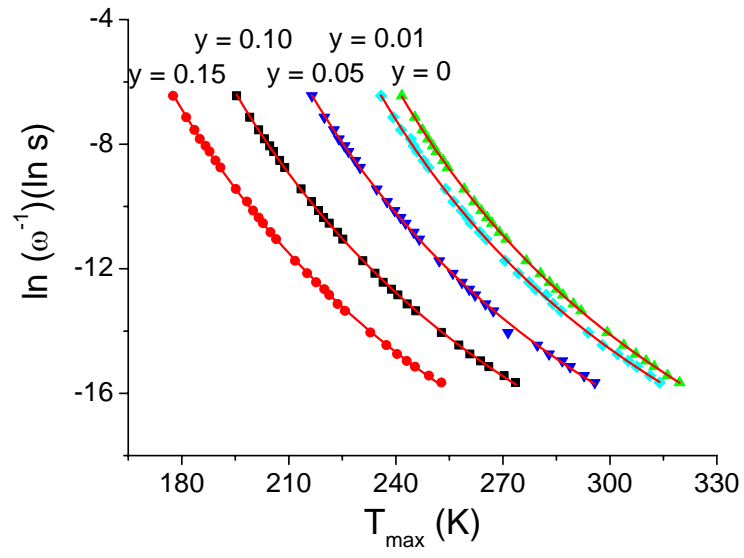
Figure 4.43.   The inverse frequency of the loss tangent maximum as a function of T_{max}

for (1-y) (0.7 BaTiO$_3$ - 0.3 BiScO$_3$) – y NaNbO$_3$ samples with y = 0 – 0.15.   Solid lines

are fits to the Vogel-Fulcher model.
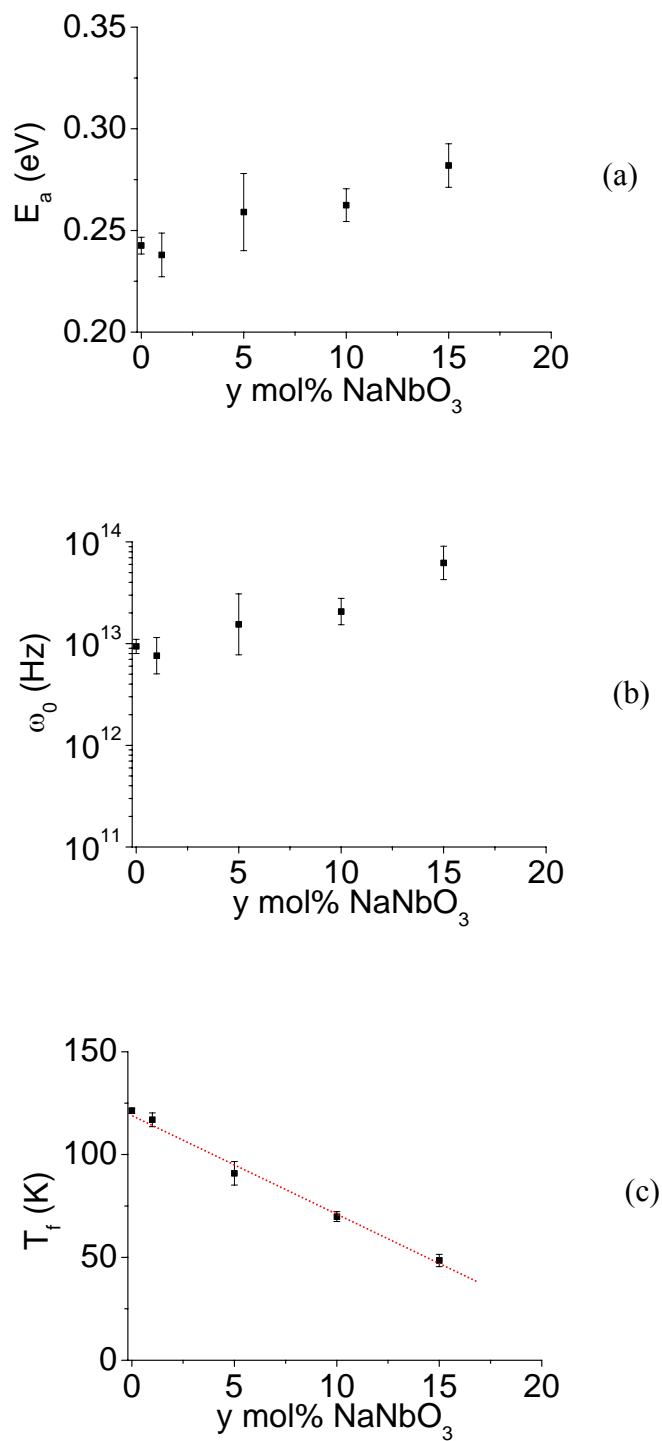
Figure 4.44. (a) Activation energy, (b) attempt jump frequency, and (c) freezing temperature obtained from the fit to the Vogel – Fulcher model for (1-y) (0.7 BaTiO₃ - 0.3 BiScO₃) – y NaNbO₃ samples with y = 0 – 0.15
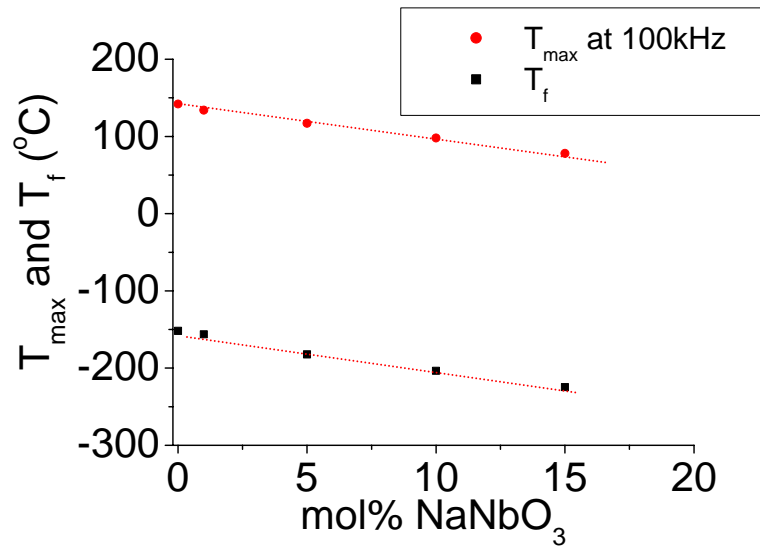
Figure 4.45. T_f and T_{max} as a function of $BiScO_3$ concentration for $(1-y)$ $(0.7\ BaTiO_3$ -

$0.3\ BiScO_3)$ – y $NaNbO_3$ samples with y $= 0 – 0.15$

The possibility of field inducing a normal ferroelectric was also investigated, since the field induced transition was confirmed in some relaxor materials such as La-modified PZT (Viehland et al., 1992) and lead magnesium niobate (PMN) (Levstik et al., 1998).   Figure 4.46 shows the dielectric result on the sample, $(1-y)$ $(0.7\ BaTiO_3$ - 0.3 $BiScO_3)$ – y $NaNbO_3$ with y $= 0.10$, via cooling with a dc bias field of about 50 kV/cm. No obvious changes in the dielectric properties were observed during and after dc bias cooling, indicating that normal ferroelectric phase could not be stabilized in the samples. This experiment should be repeated on a sample with higher T_f values.
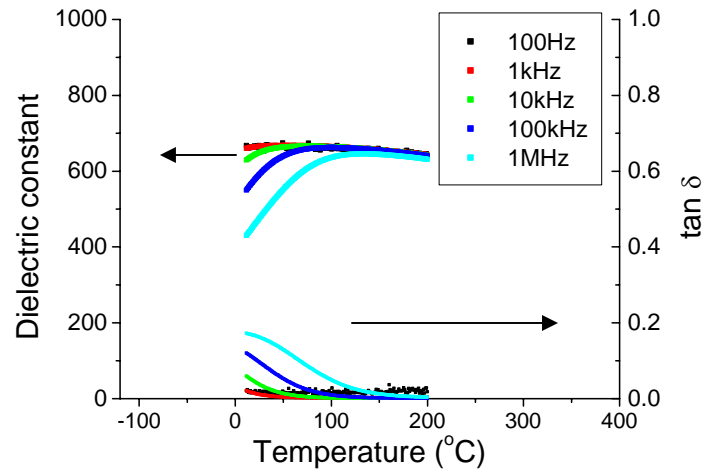
Figure 4.46.　Dielectric constant data on a (1-y) (0.7 BaTiO$_3$ - 0.3 BiScO$_3$)

– y NaNbO$_3$ ceramic with y = 0.10 via cooling with a dc bias field of about 50 kV/cm

Chapter 5: Conclusions and Future Work

5.1 Summary and Conclusions

The structural and dielectric properties of bulk $(1-x)$ BaTiO$_3$ - x BiScO$_3$ (x = 0 to 0.5) ceramics were investigated. The main purposes of the work were to confirm the result from thin films and to acquire a better understanding of the binary system, including determination of the phase diagram, displacive phase transitions, the associated dielectric properties, and the differences in the roles of Bi$_2$O$_3$ and BiScO$_3$ doping in BaTiO$_3$.

The solubility was investigated through the systematic trends in the dielectric data, lattice parameter, and microstructure. The solubility limit for BiScO$_3$ into the BaTiO$_3$ perovskite structure was determined to be x = 0.43, which is much higher than the solubility of Bi alone and in a good agreement with the thin film data (which suggested a limit of x = 0.45 without epitaxy). A structural change from tetragonal to pseudocubic was observed at about x = 0.05 - 0.075 at room temperature. The composition for the transition disagrees with the data on films, which showed clear tetragonality even with x = 0.20 and 0.30. The origin of this discrepancy is not known, but may be a function of strains associated with the film deposition.

An interesting core-shell feature in microstructure was observed for x = 0.03 – 0.1. It was found the prolonged sintering reduced the number of core-shell grains and the size of cores. However, the inhomogeneity could not be completely eliminated even with 20 hour sintering. The EDS results revealed that BiScO$_3$ is enriched in the shell. The process employed in this work also resulted in fine-grained material, especially near the BaTiO$_3$ end of the solid solution. Pure BaTiO$_3$ had grains larger than 5 μm, but the

112

composition with a few % $BiScO_3$ showed about a 0.3 μm grain size. The grain size increased slowly with further increase in the $BiScO_3$ concentration; an average grain size of 2 μm was observed for 20% $BiScO_3$.

Dielectric measurements revealed a gradual change from normal ferroelectric behavior in pure $BaTiO_3$ to a highly diffusive and dispersive relaxor behavior from 10 to 40 mol% $BiScO_3$. Several of the compositions showed high permittivities (approximately 1000) with low temperature coefficients of capacitance over a wide range of temperature. This result confirmed the result from the earlier work in thin films that the broad, frequency dependent permittivity maximum is an intrinsic material property, neither a consequence of defects or stresses associated with the thin film preparation, nor a space charge contribution. The Vogel-Fulcher model gave an activation energy of 0.2-0.3 eV for the relaxor behavior range, which was high compared with other relaxors. The attempt frequency was on the order of 10^{13} Hz and the freezing temperature ranged from -177 to -93 ^{o}C (96 to 160 K) with the $BiScO_3$ concentration. It was also found that T_{max} increases with increasing $BiScO_3$ concentration in the pseudocubic structure range.

The dielectric constant is high and stable from 0 – 300 ^{o}C, making this composition attractive for high energy density capacitor applications. A single dielectric layer capacitor was prepared to confirm the feasibility of $BaTiO_3$ - $BiScO_3$ as a capacitor material. The 0.7 $BaTiO_3$ - 0.3 $BiScO_3$ capacitors exhibited an energy density of about 6.1 J/cm^3 at a field of 73 kV/mm at room temperature, which is superior to some commercial X7R capacitors. Moreover, this system may be very useful at high temperatures, as the permittivity of commercial $BaTiO_3$ – based capacitors drops rapidly above the transition temperature (around 130 ^{o}C). In this study, the relatively high

energy density values were confirmed from room temperature to 300 $^{\circ}$C with good temperature stability.

Another application possibility is as a base composition for lead-free piezoelectrics. Undoped $BaTiO_3$ - $BiScO_3$ ceramics are electrostrictors at room temperature over a wide composition range, but the highly polarizable material may be useful as a piezoelectric matrix if a normal ferroelectric phase could be developed. Possible off-center ions, Li and Na were doped into the system in an attempt to stabilize a normal ferroelectric. Solid solution was not achieved for the case of Li. For the case of Na, solid solution was confirmed up to 15 mol% $NaNbO_3$, but there was no indication of stabilization of a normal ferroelectric. Instead, it was found that T_{max} and T_f decrease with increasing $NaNbO_3$ concentration. This result suggests that $NaNbO_3$ doping may break up the polar ordering developed in the $BaTiO_3$ – $BiScO_3$ system. This may be because the Na simply decreases the size of the unit cell, and does not off-center on the A-site (not enhance the long-range order). The reason why some dopants lead to relaxor ferroelectricity, while others stabilize a normal ferroelectric, needs to be investigated.

5.2   Future Work

5.2.1   Base BaTiO$_3$ - BiScO$_3$ Ceramics

The structural and dielectric properties on (1-x) BaTiO$_3$ – x BiScO$_3$ ceramics were studied in this work, but there are several areas which should be investigated further.

The transition from a tetragonal to a pseudocubic structure occurs at x = 0.1 in bulk ceramics, but at x = 0.4 in thin films.   It should be noted that the film data shows the symmetry change near a tolerance factor of 1, while the ceramics investigated here become pseudocubic at a tolerance factor of about 1.05, an unusually high value.   The origin of this discrepancy needs to be investigated.   The result may be related to strains associated with the film deposition.   Prolonged annealing experiments on films, or growth of films with a higher degree of structural perfection might resolve this question. Another possibility is that the result may reflect differences between powders and continuous samples.   It would be useful both to check the x-ray diffraction patterns on polished pellets and to conduct neutron diffraction experiments, where a deeper depth can be probed.

The process employed in this work resulted in fine-grained material, especially near the BaTiO$_3$ end of the solid solution, ranging from a 0.3 μm grain size for a composition with a few % BiScO$_3$ to an average grain size of 2 μm for 20% BiScO$_3$. This result is counterintuitive since extra Bi$_2$O$_3$, which would presumably act as a sintering aid, was added to the samples with x = 0.001 – 0.15.   The mechanism which is responsible for this observation should be studied.   The grain size of the samples without the extra Bi$_2$O$_3$ should be checked first to confirm if the extra Bi$_2$O$_3$ plays an important role to control this fine microstructure.   If the extra Bi$_2$O$_3$ affects the

microstructure, it may be interesting to change the amount extra Bi_2O_3 added to see how the microstructure changes as a function of the amount.

The reason for the unusually high activation energy ($\sim$ 0.25 eV) calculated from the Vogel-Fulcher fit needs to be investigated. $Ba(Ti_{0.7}Zr_{0.3})O_3$ (Yu et al., 2002) with a comparable activation energy, 0.21 eV may be a good material to compare with to sort out what factors may influence the activation energy.

Due to space charge polarizability at high temperatures ($>$ 400 ^{o}C), it was difficult to determine Burn's temperature, T_D (the temperature at which deviations from the Curie-Weiss law are observed due to the development of micropolar regions). In many lead and Bi-based relaxor materials, it is known that E_a scales with (T_D - T_f) (Stringer, 2006). It would be interesting to know T_D for the $BaTiO_3$ - $BiScO_3$ system and to categorically determine if the trend in T_D with E_a and T_f is different from the other dielectrics. To achieve this, samples with lower space charge contribution at high temperature are necessarily, which may involve a tuning of sintering conditions to further increase the density of the pellet samples. Alternatively, high precision refractive index measurements as a function of temperature may be used to determine the Burn's temperature.

5.2.2 High Energy Density Capacitor Application

The promising result obtained as high energy density capacitors with good temperature stability is attractive for further investigations on the energy storage capability of the capacitors in the $BaTiO_3$ - $BiScO_3$ system. The following should be further investigation.

The density of the capacitors prepared in this work was low, which is believed to be one of the sources of the difference observed in dielectric constant between pellets and capacitors. Improved processing is required for tape cast capacitors in this system. For example, the formulation of the slurry, including the selection of binders, the laminating conditions including pressure, time, and temperature, the binder burnout and the sintering profile should be optimized to increase the density. Sintering conditions may also affect grain size, which may influence the properties. Higher density material should have a higher energy storage capability, which will be attractive for high energy capacitor applications.

Capacitors with thinner layers should be prepared as the dielectric breakdown is likely to further increase, assuming the thermal breakdown mechanism is dominating the process. If thinner layers can be prepared, higher electric fields may be applied to achieve higher energy density.

In this study, capacitors were prepared only with one composition 0.7 $BaTiO_3$ – 0.3 $BiScO_3$. It may be interesting to prepare capacitors across the (1-x) $BaTiO_3$ – x $BiScO_3$ solid solution, to investigate the composition dependence of the energy storage. The temperature range over which the energy density is high and temperature-stable may

be a function of composition, since it was confirmed in bulk samples that T_{max} varies and the diffusive dielectric curves shift with composition in this system.

5.2.3   Non - Lead Piezoelectrics

To make the $BaTiO_3$ - $BiScO_3$ system suitable for piezoelectric applications, the diffuse dielectric characteristic needs to be reduced to develop a normal ferroelectric in the material.   Further investigation should include the following.

In this work, Li and Na ions were doped to the $BaTiO_3$ - $BiScO_3$ system as possible off-center ions which may stabilize a polarization.   However, the Li clearly was not incorporated.   Alternative processing approached which are more amenable to homogeneous cation distributions would be useful. In addition, processing at lower temperatures may help to decrease the volatility of Li.

If the dopants can achieve a solid solution, the next question is whether the dopants stabilize a normal ferroelectric or not.   If not, it would be useful to investigate to understand the difference in off-center ion behavior between the $BaTiO_3$ - $BiScO_3$ system and the silver-based perovskites.   More generally, it would be very interesting to develop an understanding of why doping leads to relaxor ferroelectricity in some matrices and stabilizes normal ferroelectric phases in others (Vugmeister and Glinchuk, 1990; Sakabe et al., 2001).

References

Arlt, G., "Domain Contributions to Piezoelectricity in Ceramics," Ultrasonics Symposium Proceedings 2 733-743 (1990).

Bahri, F., A. Simon, H. Khemakhem, and J. Ravez, "Classical or Relaxor Ferroelectric Behavior of Ceramics with Composition $Ba_{1-x}Bi_{1/3x} TiO_3$," Physica Status Solidi A **184** [2] 459-464 (2001).

Bogdanov, S. V., K. V. Kiseleva, and V. A. Rassushin, "Effect of Bismuth Impurity on Certain Physical Properties of Barium Titanate Single Crystals," Soviet Physics - Crystallography **10** [1] 58-62 (1965).

Burn, I., "Flux-sintered $BaTiO_3$ Dielectrics," Journal of Materials Science **17** [5] 1398-1408 (1982)

Burn, I. and D. M. Smyth, "Energy Storage in Ceramic Dielectrics," Journal of Materials Science **7** 339-343 (1972).

Callister, W. D., *Fundamentals of Material Science and Engineering* (John Wiley & Sons, New York, 2001).

Chen, A., Z. Jing, and Z Yu, "Ferroelectric Relaxor $Ba(Ti,Ce)O_3$," Journal of Physics: Condensed Matter **14** 8901-8912 (2002).

Chen, A., Z. Yu, and Z. Jing, "Impurity-induced Ferroelectric Relaxor Behavior in Quantum Paraelectric $SrTiO_3$ and Ferroelectric $BaTiO_3$," Physical Review B **61** [2] 957-961 (2000).

Chen, A. and Z. Yu, "Dielectric Relaxor and Ferroelectric Relaxor: Bi-doped paraelectric $SrTiO_3$," Journal of Applied Physics **91** [3] 1487-1494 (2002).

Colla, E. V., E. Y. Koroleva, N. M. Okuneva, and S. B. Vakhrushev, "Low-frequency Dielectric Response of $PbMg_{1/3}Nb_{2/3}O_3$," Journal of Physics: Condensed Matter **4** 3671-3677 (1992).

Cross, L. E. "Relaxor Ferroelectrics," Ferroelectrics **76** 241-267 (1987).

Davis, T.G., "Dielectric Properties and Soft Modes in the Ferroelectric Mixed Crystals $K_{1-x}Na_xTaO_3$" Physical Review B **5**, 2530-2537 (1972).

DiAntonio, P., B. Vugmeister, J. Toulouse, and L. Boatner, "Polar Fluctuations and First-order Raman Scattering in Highly Polarizable $KTaO_3$ Crystals with Off-center Li and Nb Ions," Physical Review B **47** [10] 5629-5637 (1993).

Eitel, R. E., C. A. Randall, T. R. Shrout, P. W. Rehrig, W. Hackenberger, and S. E. Park, "New High Temperature Morphotropic Phase Boundary Piezoelectrics Based on $Bi(Me)O_3 - PbTiO_3$ Ceramics," Japanese Journal of Applied Physics **40** [10] 5999-6002 (2001).

Fulcher, G., "Analysis of Recent Measurements of the Viscosity of Glasses," American Ceramic Society - Journal **8** [6] 339-355 (1925).

wa Gachigi, K., *Electrical Energy Storage in Antiferroelectric – Ferroelectric Phase Switching, Chemically Modified Lead Zirconate Ceramics*, Ph.D Thesis, The Pennsylvania State University (1992).

Glazer, A. M., "The Classification of Tilted Octahedra in Perovskites," Acta Crystallographica **B28** 3384 – 3392 (1972).

Glazer, A. M., "Simple Ways of Determining Perovskite Structures," Acta Crystallographica **A31** 756 – 762 (1975).

Goldschmidt, V. M., Shrifter Norske Videnskop-Adad. Oslo: Matemot. Naturuid Klasse (Nov. 1926).

Goodenough, J. B., "Jahn-Teller Phenomena in Solids," Annual Review of Materials Science **28** 1-28 (1998).

Goodenough, J. B., "Colossal Magnetoresistace in $Ln_{1-x}AMnO_3$ Perovskites," Australian Journal of Physics **52** [2] 155-186 (1999).

Haun, M. J., E. Furman, S. J. Jang, and L. E. Cross, "Thermodynamic Theory of the Lead Zirconate-Titanate Solid Solution System Parts I – V," Ferroelectrics **99** 13 - 86 (1989).

Haun, M. J., *Thermodynamic Theory of the Lead Zirconate-titanate Solid Solution System*, Ph.D. thesis, The Pennsylvania State University (1988).

Hennings, D., A. Schnell, and G. Simon, "Diffuse Ferroelectric Phase Transitions in $Ba(Ti_{1-y}Zr_y)O_3$ Ceramics," Journal of the American Ceramic Society **65** [11] 539-544 (1982).

Hochli, U. T., K, Knorr, and A. Loidl, "Orientational glasses," Advanced in Physics **39** [5] 405-615 (1990).

Isupov, V. A., "Physical Phenomena in Ferroelectric Complex Perovskites," Bulletin of the Academy of Sciences of the U.S.S.R. Physical Series **47** [3] 136-141 (1983).

IEEE, "An American National Standard IEEE Standard Definitions of Terms Associated with Ferroelectric and Related Materials" IEEE Transactions on Ultrasonics, Ferroelectrics, and Frequency Control **50** [12] 1-32 (2003).

Jaffe, B., "Antiferroelectric Ceramics with Field-Enforced Transitions: A New Nonlinear Circuit Element," Proceeding of the IRE **49 [**8] 1264 - 1267(1961).

Jaffe, B., W. R. Cook, and, H. Jaffe, *Piezoelectric Ceramics* (Academic Press, New York, 1971).

Jaffe, B., R. S. Roth, and S. Marzullo "Properties of Piezoelectric Ceramics in the Solid-Solution Series Lead Titanate - Lead Zirconate - Lead Oxide: Tin Oxide and Lead Titanate - Lead Hafnate, " Journal of Research of the National Bureau of Standards **55 [**5] 239- 254 (1955).

Jona, F. and G. Shirane, *Ferroelectric Crystals* (Dover Publications, New York, 1993).

Kingery, W. D., H. K. Bowen, and D. R. Uhlmann, *Introduction to Ceramics* (John Wiley & Sons, New York, 1976).

Kishi, H., N. Kohzu, J. Sugino, H. Ohsato, Y. Iguchi, and T. Okuda, "The Effect of Rare-earth (La, Sm, Dy, Ho and Er) and Mg on the Microstructure in BaTiO$_3$," Journal of the European Ceramic Society **19** [6-7] 1043-1046 (1999).

Kishi, H., Y. Mizuno, and H. Chazono, "Base-Metal Electrode-Multilayer Ceramic Capacitors: Past, Present and Future Perspectives," Japanese Journal of Applied Physics **42** [1] 1-15 (2003).

Kittel, C., *Introduction to Solid State Physics* (John Wiley & Sons, New York, 2005).

Kuwata, J., K. Uchino, and S. Nomura, "Electrostrictive Coefficients of Pb(Mg$_{1/3}$Ng$_{2/3}$)O$_3$ Ceramics," Japanese Journal of Applied Physics **19** [11] 2099-2103 (1980).

Lee, S., Z. Liu, M. Kim, and C. A. Randall, "Influence of Nonstoichiometry on Ferroelectric Phase Transition in BaTiO$_3$," Journal of Applied Physics **101** 054119 (2007).

Lee, S., W. H. Woodford, and C. A. Randall, "Crystal and Defect Chemistry Influences on Band Gap Trends in Alkaline Earth Perovskites," Applied Physics Letters **92** 201909 (2008).

Levstik, A., Z. Kutnjak, C. Filipic, and R. Pirc, "Glassy Freezing in Relaxor Ferroelectric Lead Magnesium Niobate," Physical Review B **57** [18] 205-211 (1998).

Lines, M. E. and A. M. Glass, *Principles and Applications of Ferroelectrics and Related Materials* (Claredon, Oxford, 1977).

Love, G. R., "Energy Storage in Ceramic Dielectrics," Journal of American Ceramic Society **73** [2] 323-328 (1990).

Matsubara, M., T. Yamaguchi, W. Sakamoto, K. Kikuta, T. Yogo, and S. Hirano, "Processing and Piezoelectric Properties of Lead-free (K, Na) (Nb, Ta) O$_3$ Ceramics," Journal of American Ceramic Society **88** [5] 1190-1196 (2005).

Megaw, H.D., *Ferroelectricity in Crystals* (Methuen & Co Ltd., London, 1957).

Megaw, H. D., *Crystal Structures: A Working Approach* (W.B. Saunders, Philadelphia, 1973).

Mitsui,T., I. Tatsuzaki, and E. Nakamura, "An Introduction to the Physics of Ferroelectrics," *Ferroelectricity and Related Phenomena*, edited by I. Lefkowitz and G. W. Taylor (Gordon and Breach Science Publishers, New York, 1976).

Moulson, A. J. and J. M. Herbert, *Electroceramics: Materials, Properties, Applications, 2nd ed.* (Wiley, England, 2003).

Navrotsky, A., *Structure and Bonding in Crystals*, edited by M. O'Keeffe (Academic Press, New York, 1981).

Newnham, R. E., *Properties of Materials; Anisotropy, Symmetry, Structure* (Oxford University Press, New York, 2005).

Nino, J. C, M. T. Lanagan, C. A. Randall, and S. Kamba, "Correlation Between Infrared Phonon Modes and Dielectric Relaxation in $Bi_2O_3 - ZnO - Nb_2O_5$ Pyrochlore," Applied Physics Letters **81** [23] 4404-4406 (2002).

Nye, J. F., *Physical Properties of Crystals Materials* (Oxford University Press, London, 1985).

Randall, C.A. and A.S. Bhalla, "Nanostructural-Property Relations in Complex Lead Perovskites," Japanese Journal of Applied Physics **29** [2] 327 - 333 (1990).

Randall, C. A., S. F. Wang, D. Laubscher, J. P. Dougherty, and W. Huebner, "Structure Property Relationships in Core-shell $BaTiO_3 - LiF$ Ceramics," Journal of Materials Research **8** [4] 871-879 (1993).

Reaney, I. M., E. L. Colla, and N. Setter, "Dielectric and Structural Characteristics of Ba – and Sr – based Complex Perovskites as a Function of Tolerance Factor," Japanese Journal of Applied Physics **33** 3984 – 3990 (1994).

Saburi, O., "Properties of Semiconductive Barium Titanates," Journal of the Physical Society of Japan **14** [9] 1159-1174 (1959).

Saito, Y., H. Takao, T. Tani, T. Nonoyama, K. Takatori, T. Homma, T. Nagaya, and M. Nakamura, "Lead-free Piezoelectrics," Nature **432** 84-86 (2004).

Sakabe, Y., T. Takeda, Y. Ogiso, and N. Wada, "Ferroelectric Properties of $(Ag,Li)(Nb,Ta)O_3$ Ceramics," Japanese Journal of Applied Physics **4** [9B] 5675-5678 (2001).

Samara, G. A., "The Relaxational Properties of Compositionally Disordered ABO_3 Perovskites," Journal of Physics: Condensed Matter **15** 367 - 411 (2003).

Sasaki, S., C. T. Prewitt, and R. C. Liebermann, "The Crystal Structure of $CaGeO_3$ Perovskite and the Crystal Chemistry of the $GdFeO_3$-type Perovskites," American Mineralogist **68** 1189 - 1198 (1983).

Sawyer, C. B. and C. H. Tower, "Rochelle Salt as a Dielectric," Physical Review **35** 269 - 273 (1930).

Shannon, R. D., "Revised Effective Ionic Radii and Systematic Studies of Interatomic Distances in Halides and Chalcogenides," Acta Crystallographica A **32** 751-767 (1976).

Shrout, T. R. and S. J. Zhang, "Lead-free Piezoelectric Ceramics: Alternatives for PZT?," Journal of Electroceramics **19** 111-124 (2007).

Shuvalov, L. A., "Symmetry Aspects of Ferroelectricity," Journal of the Physical Society of Japan **28** [supplement] 38 - 51 (1970).

Sinha, J. K., "Modified Sawyer and Tower Circuit for the Investigation of Ferroelectric Samples," Journal of Scientific Instruments **42** [9] 696-698 (1965).

Skanavi, G. I., I. M. Ksendzov, V. A. Trigubenko, and V. G. Prokhvatilov, "Relaxation Polarization and Losses in Nonferroelectric Dielectrics with High Dielectric Constants," Soviet Physics JETP **6** [33] 250-259 (1958).

Stringer, J. C., *Structure – Property – Performance Relationships of New High Temperature Relaxors for Capacitor applications,* Ph.D Thesis, The Pennsylvania State University (2006).

Stringer, J. C., T. R. Shrout, and C. A. Randall, "High-temperature Perovskite Relaxor Ferroelectrics: A Comparative Study," Journal of Applied Physics **101** 054107 (2007).

Smolensky, G. A., "Physical Phenomena in Ferroelectrics with Diffused Phase Transition," Journal of the Physical Society of Japan **28** Supplement 26-37 (1970).

Takenaka, T. and H. Nagata, "Present Status of Non-Lead-Based Piezoelectric Ceramics," Key Engineering Materials **157-158**, 57-64 (1999).

Takenaka, T. and H. Nagata, "Current Status and Prospects of Lead-free Piezoelectric Ceramics," Journal of the European Ceramic Society **25** 2693-2700 (2005).

Tinberg, D. S., *Pulsed Laser Deposition of x BiScO$_3$ – (1-x) BaTiO$_3$ Thin Films for Lead Free Dielectric Applications,* Master of Science Thesis, The Pennsylvania State University (2006).

Tinberg, D. S. and S. Trolier-McKinstry, "Structural and Electrical Characterization of xBiScO$_3$ – (1-x)BaTiO$_3$," Journal of Applied Physics **101**, 024112 (2007).

Vegard, L., "Die Konstitution der Mischkristalle und die Raumfullung der Atome," Zeitschrift fur Physik **5** [1] 17-26 (1921).

Viehland, D., *The Glasy Behavior of Relaxor Ferroelectrics,* Ph.D Thesis, The Pennsylvania State University (1992).

Viehland, D,. S. J. Jang, and L. E. Cross, "Freezing of the Polarization Fluctuations in Lead Magnesium Niobate Relaxors," Journal of Applied Physics **68** [8] 2916-2921 (1990).
Viehland, D., J. F. Li, S. J. Jang, L. E. Cross, and M. Wuttig, "Glassy Polarization Behavior of Relaxor Ferroelectrics," Physical Review B **46** [13] 8013-8017 (1992).

Vogel, H., "Das Temperature- abhangigkeitsgesetz der Viskositat von Flussigkeiten (The Law of Viscosity Change with Temperature)," Physikalische Zeitschrift **22** 645-646 (1921).

Vugmeister, B. E. and M. Glinchuk, "Dipole Glass and Ferroelectricity in Random-site Electric Dipole Systems," Reviews of Modern Physics **62** [4] 993-1026(1990).

Weast, R. C., *Handbook of Chemistry and Physics, A Ready – Reference Book of Chemical and Physical Data* (CRC Press, PLACE, 1976).

Woodward, D. I., I. M. Reaney, R. E. Eitel, and C. A. Randall, "Crystal and Domain Structure of the $BiFeO_3 – PbTiO_3$ Solid Solution," Journal of Applied Physics **94** [5] 3313-3318 (2003).

Woodward, D. I., J. Knudsen, and I. M. Reaney, "Review of Crystal and Domain Structures in the $PbZr_xTi_{1-x}O_3$ Solid Solution," Physical Review **B72** 104110 (2005).

Woodward, P. M., "Octahedral Tilting in Perovskites. I. Geometrical Considerations," Acta Crystallographica B **53** 32- 43 (1997).

Yu, Z., A. Chen, R. Guo, and A. S. Bhalla, "Ferroelectric-relaxor Behavior of $Ba(Ti_{0.7}Zr_{0.3})O_3$," Journal of Applied Physics **92** [5] 2655-2657 (2002).

Zhang, C. L. , Z. X. Chen, L. E. Cross, and W. A. Schulze, "Dielectric and Piezoelectric Properties of Modified Lead Titanate Zirconate Ceramics from 4.2 to 300K," Journal of Materials Science **18** [4] 968-972 (1983).

Zhang, Q. M. H., Wang, N. Kim, and L. E. Cross, "Direct Evaluation of Domain-Wall and Intrinsic Contributions to the Dielectric and Piezoelectric Response and their Temperature Dependence on Lead Zirconate-Titanate Ceramics," Journal of Applied Physics 75 454 – 459 (1994).

Zhou, L., P. M. Vilarinho, and J. L. Baptista, "Solubility of Bismuth Oxide in Barium Titanate," Journal of American Ceramic Society **82** [4] 1064-1066 (1999).